iTRVZ: liquid nano-platform for signal integration on the plasma membrane

Authors

Taka A. Tsunoyama[1], Christian Hoffmann[2], Bo Tang[1], Koichiro M. Hirosawa[3], Yuri L. Nemoto[1], Rinshi S. Kasai[3], Takahiro K. Fujiwara[4], Kenichi G.N. Suzuki[3,4], Dragomir Milovanovic[2], Akihiro Kusumi[1,4]*

Affiliations

[1]Membrane Cooperativity Unit; Okinawa Institute of Science and Technology Graduate University (OIST); Onna-son, Okinawa, 904-0495; Japan.

[2]Laboratory of Molecular Neuroscience; German Centre for Neurodegenerative Diseases (DZNE); Berlin, 10117; Germany.

[3]Institute for Glyco-Core Research (iGCORE); Gifu University; Gifu, 501-1193; Japan.

[4]Institute for Integrated Cell-Material Sciences (WPI-iCeMS); Kyoto University; Kyoto, 606-8501; Japan.

Contact info

*Corresponding author. Email: akihiro.kusumi@oist.jp

Highlights (four highlights, 85 characters including spaces)

- Integrin, talin, RIAM, VASP, and zyxin are clustered which called iTRVZ
- iTRVZ forms liquid-like nanoscale cluster throughout the plasma membrane
- Downstream molecules are recruited to iTRVZ upon different receptor stimulations
- Phase separation is critical for iTRVZ formation and its signal transduction
- Two weak inputs are integrated in iTRVZ and non-linearly amplified to strong output

SUMMARY (150 words, now 120)

Crosstalk of cellular signaling pathways is essential for coordinating cell responses. Therefore, we suspect the existence of special scaffolding platforms that specifically undertake signal crosstalk and integration. Using advanced single-molecule imaging, we found a nanometer-scale liquid-like platform for integrating the signals downstream from GPI-anchored receptors and receptor-type tyrosine kinases. The platform employs some of the focal adhesion proteins, including integrin, talin, RIAM, VASP, and zyxin, but is distinct from focal adhesions, and is thus termed iTRVZ. The iTRVZ formation is driven by the protein liquid-liquid phase separation and the interactions with the raft domains in the plasma membrane and cortical actin. iTRVZ non-linearly integrates the two distinctly different receptor signals, and thus works as an AND gate and noise filter.

INTRODUCTION

Signaling pathways downstream from receptors are the targets of extensive investigations. In particular, understanding how each signaling pathway is integrated into coordinated cellular signal responses is one of the most critical issues in today's signaling research [1]. We hypothesized that PM-associated structures that function as platforms for signal integration might exist. Since integrins are involved in the signaling of receptor-type tyrosine kinases (RTKs) [2], immunoglobulin E Fc receptor [3], and glycosylphosphatidylinositol (GPI)-anchored receptors (GPI-ARs), including CD59, Thy1, and CD55 [4–9], we examined the possibility that an integrin-centered signal integration platform might exist on the PM cytoplasmic surface.

RESULTS

The iTRVZ's main constituent molecules, RIAM, VASP, and zyxin ()

Talin, a focal-adhesion (FA) protein, binds to integrins and various signaling molecules [10,11]. We examined the possibility that talin might play a central role in the formation and function of the hypothetical signal integration platform. We expressed tagged-talin1 molecules (four different tags) in talin1/2 double-knockout mouse embryonic fibroblasts (dKO MEFs) [11], at levels comparable to that of endogenous talin1 (**fig. S1, A to K**). Our advanced single-molecule imaging revealed that fluorescently-labeled talin1 (talin; in the following, talin1 is described as talin) formed numerous clusters on the cytoplasmic surface of the *apical* PM, where virtually no FAs exist [12], even without stimulation (**fig. S1I, and movie S1**).

Clustered CD59, containing an average of five CD59 molecules mimicking the ligated signaling-active CD59 [4,5], and ligated PDGFR were transiently and repeatedly recruited to the talin clusters on the apical PM, with a dwell lifetime of each recruitment lasting for ~0.3 s (exponential decay time constant, t_2; **Fig. 1, A and B, movies S2 and S3, and Materials and Methods**). The recruitments of these receptors suggested that the talin clusters might function as the signaling platform for both receptors.

The iTRVZ's main constituent molecules, RIAM, VASP, and zyxin

We examined another FA protein, zyxin. Tagged zyxin proteins expressed at the level similar to that of endogenous zyxin in zyxin-KO MEF cells [13] also forms clusters on the *apical* PM (**fig. S1, E to I, and movie S1**). Each talin and zyxin cluster contains a median of 4.0 and 4.8 copies of talin and zyxin, respectively (with broad distributions between 2 and 15 copies/cluster) (**Fig. 1C**). These clusters exist on the apical PM densely, with a mean number density of ~0.25 clusters/mm^2 for both talin and zyxin (**Fig. 1D**). This number density is comparable to that of clathrin-coated structures [14].

Approximately 70% of the talin and zyxin clusters were colocalized with each other (**Fig. 1E, and fig. S1, J and K**, respectively), suggesting that these clusters are co-clusters of talin and zyxin. Meanwhile, this 70% colocalization of talin and zyxin clusters indicated that some

of them might contain 0-2 copies of the talin and zyxin/cluster (the presence of 1~2 copies in the cluster could be missed under the employed imaging conditions). Zyxin and talin copy numbers in each cluster vary greatly (**Fig. S1L**), indicating very high freedom of stoichiometry in the co-clusters. Allowing high flexibilities in stoichiometry for incorporating various molecules would be an important feature as the signaling platform.

We refer to these altogether as "talin-zyxin clusters". Partial actin depolymerization with latrunculin A and cytochalasin D, and myosin deactivation with the ROCK inhibitor Y27632 reduced both the number density of talin clusters in the apical PM and the number of talin molecules within a talin cluster, suggesting that the formation of the talin-zyxin clusters requires the intact actin-myosin system. Meanwhile, stimulation by CD59 clustering or PDGF addition did not induce any changes in either the talin cluster number density or the talin number within a cluster (**Fig. 1, C and D**).

The lifetime of the talin-zyxin clusters exhibited the presence of two components (**Fig. 1F**): ~15% lasted for ~1 s and ~85% lasted for ~10 s (arithmetic means of talin and zyxin lifetimes). These lifetimes would represent both the decomposition of the clusters and the dissociation of the clusters from the apical PM. Meanwhile, the lifetime of talin clusters without zyxin observed in the zyxin-KO MEFs and the lifetime of zyxin clusters without talin in talin-dKO MEFs were both 1.1 s, and after rescue, the lifetimes became 9.5 s and 7.7 s, respectively (**Fig. S1M**; all SEM values given in figures). These results indicate that the ~1-s component (~15%) of the talin-zyxin clusters represents those that do not contain either talin or zyxin. The value of 85% for the 7.7~9.5-s component is indeed close to the 70% estimated for the clusters containing both (more than two) talin and zyxin proteins.

Single molecules of talin and zyxin repeatedly entered and exited from the clusters, with dwell lifetimes in the talin-zyxin cluster of 2.1 and 1.4 s, respectively (**Fig. 1G, and fig. S1N**), indicating that these molecules exchange with those in the bulk cytoplasm several times during the lifetime of the talin-zyxin cluster. This result indicates the liquid-like characteristics of the clusters.

Photoactivation localization microscopy (PALM) of talin and zyxin in fixed cells, followed by a Voronoï tessellation analysis [15,16], detected their nanoscale clusters (median diameter = 60 nm) on the *apical* PM at a number density of 0.35 clusters/μm^2 (mean; the average for

talin and zyxin) (**Fig. 1, H to K, and fig. S2, A to G**), consisting of a mean of 6.1 and 8.2 copies of talin and zyxin, respectively (slightly overestimated because clusters containing fewer than 3 copies were undetectable; **Fig. 1J**).

In summary, talin-zyxin clusters are liquid-like, nanoscale clusters with a lifetime on the PM of ~10 s, where constituent molecules and engaged receptors (PDGFR and CD59) are exchanging on the time scale of 0.3 - 2.1 s (see the intensity fluctuations of the cluster in **movie S4**). Talin-zyxin clusters were found in all five cell lines examined here (**fig. S3A**), suggesting that these clusters broadly exist in mammalian cells.

The iTRVZ's main constituent molecules, RIAM, VASP, and zyxin

To facilitate the observations of single-molecule recruitment to the talin-zyxin clusters in the *apical PM*, we employed a human T24 epithelial cell line, because the apical PM of the T24 cell is quite flat, facilitating single-molecule imaging (**fig. S3, B to E**). We generated the T24 cells stably expressing SNAPf-talin (called T24-T; together with endogenous talin1, expressing 1.7x more talin than that in wild-type cells). As in MEFs, the engaged CD59 and PDGFR were transiently recruited to the talin-zyxin clusters in T24-T cells (**fig. S3, F to I**).

We next investigated the presence of other FA proteins in the talin-zyxin clusters (**fig. S3J**). To systematically evaluate the propensity of the FA proteins to colocalize with the talin-zyxin clusters at the level of single molecules, we employed the "colocalization index", which is a measure of finding a molecule within a 50 nm radius circle around the center of the talin cluster relative to far distances [17] (as a control, all fluorescent spots were shifted by 1 μm with random angles in 2D) (**fig. S3K, and Materials and Methods**). b3 integrin (i), RIAM (R), VASP (V), and zyxin (Z) were remarkably colocalized with the talin (T) clusters even before PDGF stimulation, and therefore, we coined the name iTRVZ for the talin-zyxin cluster. Meanwhile, paxillin, vinculin, and N-WASP were not colocalized, showing that although iTRVZ contains FA proteins, its protein composition is distinct from that of the mature FA [18] (**Fig. 2A**). The actin-binding proteins a-actinin and filamin were also colocalized with iTRVZ. Upon PDGF stimulation, interestingly, the colocalizations of the T, R, V, and Z proteins were not increased, whereas those of integrin and FAK were increased (**Fig. 2A**). Consistently, the dwell lifetime of FAK at the iTRVZ was elongated (**fig. S3, L and M, and movie S5**).

Furthermore, paxillin and N-WASP were recruited to iTRVZ after stimulation.

The iTRVZ's main constituent molecules, RIAM, VASP, and zyxin

The PDGF stimulation induced the iTRVZ recruitment of FAK, PLCg1, Lyn, PI3K, and Akt (**Fig. 2, A and B**). Furthermore, PLCg1 was transiently recruited to iTRVZ upon the engagements of GPI-ARs (CD59 and Thy1) and RTKs (PDGFR and EGFR), and PLCb was recruited upon the stimulation of a GPCR (UTP receptor, P2Y) (**Fig. 2, C and D**). The recruitment of these molecules was reduced by the inhibitors for FAK and SFK (**Fig. 2C**, however, EGF stimulation after FAK inhibitor treatment and UTP stimulation after both inhibitor treatments showed moderate reduction without significant differences). The PDGF-induced PLCg1 recruitment additionally occurred on the PM outside the iTRVZ (**fig. S3, N and O**), indicating that the PDGFR's downstream signal occurs both inside and outside the iTRVZ. However, the PLCg1's recruitment per unit area is ~30 times greater in the iTRVZ than in the region outside the PM (**Fig. 2E**, see also **fig. S3, N and O**), indicating that the signaling reactions would occur much more efficiently in iTRVZ (**Fig. 2F**). As such, iTRVZ works as a platform for various signaling pathways.

The iTRVZ's main constituent molecules, RIAM, VASP, and zyxin

The involvement of phosphoinositides in iTRVZ was examined because PLCg1 is recruited to iTRVZ, and talin and RIAM bind PI(4,5)P_2 [19,20] (**Fig. 3, A to C, and movie S6**). Using probes for various phosphoinositides [21], PI(4)P and PI(4,5)P_2, but not PI(3)P and PI(3,4)P_2, were localized at the iTRVZ both before and after PDGF stimulation equally, but PI(3,4,5)P_3 was found only after stimulation (**Fig. 3C**). PI3K, which generates PI(3,4,5)P_3 from PI(4,5)P_2, was recruited to the iTRVZ only after PDGF stimulation (**Fig. 2B**), whereas PIP5K, which generates PI(4,5)P_2 and binds to talin [19] and MARCKS, a PI(4,5)P_2-sequestering protein, were recruited even before stimulation without any changes after stimulation. These results suggest that PI(3,4,5)P_3 is generated from PI(4,5)P_2 by the PI3K recruited to iTRVZ upon stimulation.

Meanwhile, typical raftophilic lipids, cholesterol and sphingomyelin (SM), were colocalized with the iTRVZ [22,23] (**Fig. 3, B and C**). The number density and size (talin number)

of the iTRVZ were reduced after partial depletions of cholesterol and PI(4,5)P_2 [4,5,24,25] (**fig. S4, A to K**). Phosphatidylserine (PS), with its long, saturated acyl chain subfraction putatively involved in the aster formation of GPI-ARs and actin filaments [9,26,27], was also colocalized with the iTRVZ (**Fig. 3C**). These results suggest that iTRVZ is supported by raft-lipid interactions [28] by way of PI(4,5)P_2 (and possibly long, saturated-chain PS). Meanwhile, the RTK's downstream signaling molecules JAK1, K-Ras, and Raf were not recruited to the iTRVZ (**Fig. 3D**).

In conclusion, iTRVZ, formed with the aid of raft domains by way of PI(4,5)P_2 and PS, recruits various signaling molecules downstream from the activated receptors, and works as the signal transduction platform for GPI-ARs, RTKs, and GPCRs (**Fig. 3E**). Namely, iTRVZ is shared by these receptor signaling pathways, suggesting the possibility that signal crosstalk and integration are induced there.

The iTRVZ's main constituent molecules, RIAM, VASP, and zyxin

Indeed, iTRVZ cooperatively and non-linearly integrates the PDGFR (RTK) and CD59 (GPI-AR) signals. First, we weakly stimulated the cells by adding either 20 pM PDGF (physiological concentration in the serum [29]) or 20 nM anti-CD59 mAb coated beads for CD59 clustering, which are 1/1,000 and 1/100 concentrations of our standard conditions, respectively. They induced much lower PLCg1 recruitment to the iTRVZ and Ca^{2+} responses than those in our standard conditions (**Fig. 4, A and B, and fig. S5A**). When we added both stimulants at the same time, the PLCg1 recruitment to iTRVZ and the Ca^{2+} responses became greater than the sum of those induced by separate stimulations, by factors of 4.7 and 6.8, respectively (**Fig. 4, A and B, and fig. S5A**), clearly demonstrating the cooperative, non-linear integration of the two signals.

This non-linear integrated amplification depended on iTRVZ, because it did not happen with zyxin-KO cells. However, it was recovered by the addition of the intrinsically disordered region [IDR] of zyxin, which is responsible for the formation of zyxin-talin co-clusters (**Fig. 4, A and B, and fig. S5, B and C;** for the zyxin's IDR, see the next subsection).

The non-linear integration depended on the activation of both FAK and SFK at iTRVZ (**Fig. 4, A and B, and fig. 5C**), and did not occur outside the iTRVZ (**Fig. 4B**). Since the weak

CD59 stimulation induced the FAK recruitment to iTRVZ more effectively than the SFK recruitment, and the weak PDGF stimulation triggered SFK recruitment but not the FAK recruitment (**fig. 5D**), the cooperative integration is considered to be induced by the simultaneous recruitment of SFK and FAK to iTRVZ, causing their upward spiral activations (**Fig. 4C, and fig. S5E**). In conclusion, iTRVZ works as a cooperative signal integrator for multiple, coincidental signals due to the co-activation of SFK and FAK in the fluid nano-region.

The iTRVZ's main constituent molecules, RIAM, VASP, and zyxin

The iTRVZ's main constituent molecules, RIAM, VASP, and zyxin, contain long intrinsically disordered regions (IDRs) [30] (**Fig. 4D, and fig. S6, A and B**), which are often involved in liquid-liquid phase separation (LLPS) [31–34]. Therefore, we examined the involvement of LLPS in iTRVZ formation.

First, iTRVZ was reduced in size (the talin number) in MEF cells after a 1,6-hexanediol treatment, which is known to disperse liquid condensates (**Fig. 1C**). Second, purified zyxin and VASP formed micron-scale liquid-like co-condensates *in vitro* at endogenous concentrations of 0.7~3.0 and 0.25 ~0.7 mM, respectively (**Fig. 4, E and F, and fig. S7, A to J**), indicating that zyxin and VASP are capable of undergoing LLPS. In T24 cells, micron-scale condensates of zyxin and VASP were never observed at endogenous expression levels, but were formed (always co-clustered) in cells overexpressing the proteins at ~14 μM average concentrations in the cytoplasm (**Fig. 4, G and H, fig. S7, K to M, and movie S7**), probably due to the presence of higher concentrations of proteins and other electrolytes like ATP [35]. The results obtained using WT and mutant zyxin (**Fig. 4D**), as well as those of VASP and RIAM, showed that the non-phosphorylated IDR domains are essential for their recruitment to iTRVZ (**Fig. 4I, and fig. S8, A and B**).

To further examine the IDR involvement in iTRVZ formation and signal transduction, we produced seven zyxin-KO MEF cell lines expressing different zyxin mutants (**fig. S9, A to F**). By comparing the sizes (talin numbers) and lifetimes of the iTRVZ in these cell lines (**fig. S9, D and E**), we found that the dephosphorylated IDR (including the Pro-rich domain) of zyxin enhance iTRVZ formation. Upon PDGF stimulation, the four cell lines expressing zyxin lacking IDRs or expressing phosphomimetic zyxin exhibited lower Ca^{2+} responses and Akt

phosphorylation, as compared with the zyxin-KO MEF cells rescued with the full-length zyxin (**Fig. 4, J to L, and fig. S9, G and H**). As described in the previous subsection, the non-linear integration of the weak CD59 and PDGF signals did not occur in cells without zyxin expression, but was recovered by expressing zyxin's IDR (**Fig. 4B, and fig. S5A**). In conclusion, these data demonstrate that the IDR-based LLPS is critical for generating the functional iTRVZ platform.

DISCUSSION

The iTRVZ's main constituent molecules, RIAM, VASP, and zyxin

We identified a nanoscale liquid-like signal integration platform on the PM, iTRVZ (**fig. S10**), which exists in both the apical and basal PMs. The iTRVZ platform is commonly used for the signaling pathways of three representative receptor classes: GPI-AR (CD59, Thy1), RTK (PDGFR, EGFR), and GPCR (UTP receptor, P2Y) (**Fig. 2C**). The recruited receptors and downstream signaling molecules would interact at iTRVZ extremely rapidly and efficiently, due to the very small sizes of the iTRVZ platform (50 ~ 80 nm in diameter) and its liquid nature.

The iTRVZ's main constituent molecules, RIAM, VASP, and zyxin

iTRVZ works as a cooperative and non-linear integrator and coincidence detector/amplifier of the signals from these different signaling pathways. Non-linear integration and coincidence detection/amplification would be critically important for inducing strong downstream signals when two separate external signals are received by the cell at about the same time, as well as for filtering out the accidentally evoked noise that would be prevalent in the cytoplasm [36,37].

The lifetime of iTRVZ is ~10 s, and its constituent molecules and recruited receptors and signaling molecules exchange with those in the bulk cytoplasm in the time scale of 0.2 - 3 s (**Fig. 1F and fig. S1L**), although the overall receptor signal in a whole cell tends to last for several minutes or longer. This indicates that each iTRVZ platform would create unit pulse-like signals on the order of seconds, and that the signal observed for a whole single cell, like the phosphorylation levels and Ca^{2+} mobilization, would be the result of the

summation of the unit pulse-like signals from many iTRVZ [4,5,38,39]. In addition, the limited iTRVZ lifetime and dwell lifetimes of signaling molecules would be useful for turning off the signals quickly and reliably: the output signal from each iTRVZ would be stopped within ~10 s without fail because iTRVZ will self-destruct and/or self-dissociate from the PM in 10 s. Similar transient liquid-like nanoscale signaling platforms might exist for other signaling systems [34,40] including those in immune cells [3,40].

The iTRVZ is probably formed by LLPS due to the IDR-IDR interactions of zyxin and VASP, and perhaps those of RIAM and other constituent molecules (**Fig. 4, D to I, and figs. S7 to 9**). The protein LLPS condensates on the nanometer scale have been suggested recently [41]. The iTRVZ is interfaced with the raft domains by way of PI(4,5)P_2, and possibly PS with long, saturated acyl chains [26]. The enhanced 3D protein LLPS on the raft domain surface has been suggested recently [42].

For the iTRVZ functions, the liquid-like properties of iTRVZ with loose stoichiometries, supported by the IDR-based LLPS, would be critically important. They would make iTRVZ quite versatile, to allow for the recruitment of a variety of receptors (some RTKs might participate in LLPS [43]) and signaling molecules without strict stoichiometric limitations, the enhancement of their interactions, their rapid departures from iTRVZ, and its self-destruction in 10 s. In the basal PM, some of the iTRVZs might convert into nano-scale nascent FAs upon the applied stress via integrin and vinculin recruitment [9,10,18,44]. iTRVZ was found in all of the cell lines examined in this study, and thus we conclude that it is a fundamentally important signal integration platform ubiquitously functioning in mammalian cells.

ACKNOWLEDGMENTS

We thank the PIs for the kind gifts of cell lines and cDNAs (details are given in the **STAR Methods**). We also thank Drs. P. Kanchanawong, S. Liu, and M. Kham (National University of Singapore) for the technical support for the mouse embryonic stem cell culture, Drs. P. Barzaghi and B. Humbel (OIST Imaging Section) for supporting FRAP experiments, and Drs. K. Simons (Lipotype GmbH), S. Mayor (National Centre for Biological Sciences), and all members of the Kusumi laboratory for valuable discussions. This work was supported in part by Japan Society for the Promotion of Science (JSPS) Grants-in-Aid for Scientific Research (Kiban A to A.K. [21H04772], Kiban S to A.K. [16H06386], Kiban B to T.K.F. [16H04775], Kiban C to R.S.K. [17K07333], Wakate B to R.S.K. [26870292], Wakate to T.A.T. [21K15058], and Challenging Exploratory Research to T.K.F. [18K19001]), a Grant-in-Aid for Innovative Areas from the Ministry of Education, Culture, Sports, Science and Technology of the Japanese government (MEXT) to K.G.N.S. (18H04671), a Japan Science and Technology Agency (JST) grant in the program of the Core Research for Evolutional Science and Technology (CREST) in the field of “Biodynamics” to A.K. and that in the field of “Extracellular Fine Particles” to K.G.N.S. (JPMJCR18H2), and a JST grant ACT-X to T.A.T. (JPMJAX211B). WPI-iCeMS of Kyoto University is supported by the World Premiere Research Center Initiative (WPI) of MEXT.

AUTHOR CONTRIBUTIONS

T.A.T. performed large majorities of the single-fluorescent-molecule imaging, biochemical, and molecular biology experiments and analyses. T.A.T., T.K.F., and A.K. developed the single-molecule imaging camera system, set up single-molecule imaging stations, and developed the analysis software. C.H. and D.M purified zyxin and VASP and, together with T.A.T., performed LLPS and FRAP experiments. B.T. generated protein probes for cholesterol and sphingomyelin. T.A.T., Y.L.N., K.M.H., R.S.K., T.K.F., K.G.N.S., C.H., D.M., and A.K. participated in discussions throughout the course of this research. T.A.T., T.K.F., K.G.N.S., and A.K. conceived and formulated this project, and evaluated and discussed data. T.A.T. and A.K. wrote the manuscript and all authors participated in its revision.

DECLARATION OF INTERESTS

The authors declare no competing interests.

MAIN FIGURE TITLES AND LEGENDS

Figure 1. Co-clusters of talin and zyxin with ~10-s lifetimes on the apical PM recruit receptors

(**A**) Visualization of talin and zyxin clusters in single fluorescent-molecule movies recorded at normal video rate (30 frames/s; top) by rolling averaging over 30 frames, followed by background subtraction using a rolling ball with a 30 pixel (1.5 μm) radius (middle). Talin and zyxin clusters were detected by using an in-house computer program to detect single fluorescent molecules in the image [45], and are indicated by circles (bottom). After rolling averaging, rapidly diffusing single molecules in the bulk cytoplasm are blurred-out and only immobile/slowly diffusing molecules on the PM can be visualized (**Video S1**). Halo7-far: Halo7 fused to the CAAX motif of K-Ras at Halo7's C-terminus, a control for rapidly diffusing molecules due to its anchoring to the fluid PM via the attached farnesyl group.

(**B** and **C**) Engaged CD59 (clustered by a fluorescent bead coated with anti-CD59 mAb) and Halo7-PDGFR (trajectories) were recruited to SNAPf-talin clusters (white spots in (B)) with dwell lifetimes of 0.33 and 0.22 s, respectively (C) (**Videos S2 and S3**). Throughout this work, we found that the dwell time distributions could be fitted by double exponential functions, and the longer decay time constants, τ_2, provided biologically meaningful lifetimes (**the main text; STAR Methods**), while the fitting error provided the SEM (n_{cells} = 20, n_{events} = 955, 1,046, 758, and 1,094 for CD59 mononer, CD59 cluster, –PDGF, and +PDGF, respectively).

(**D**) Distributions of the numbers of Halo7-tagged molecules residing in each cluster (monomer control: farnesylated Halo7 [Halo7-far], n_{cells} = 15, n_{spots} = 2,415 ~ 10,780).

(**E**) Number densities of Halo7-tagged talin and zyxin clusters on the apical PM (dots for individual cells; bars for mean ± SEM, n_{cells} = 15).

(**F**) Lifetime distributions of individual Halo7-tagged clusters (n_{cells} = 10, n_{spots} = 7,407 and 6,888 for talin and zyxin, respectively).

(**G** and **H)** Typical dual color images of talin and zyxin clusters (indicated by circles, G) and quantitative result in (H); ~70% clusters are colocalized with each other.

(**I**) Correlations between the copy numbers of talin and zyxi in each cluster (n_{cells} = 15, n_{spots} = 4,806 and 7,729 for talin1/2-dKO MEFs and zyxin-KO MEFs, respectively), indicating loose

stoichiometries for zyxin and talin in each cluster.

(**J**) Distributions of the dwell times of single talin and zyxin molecules inside the talin cluster and typical trajectories of single talin and zyxin molecules on the PM, exhibiting their temporary recruitment (magenta trajectories) to talin clusters (cyan circles). Note that about half of the talin and zyxin molecules were recruited directly from the cytoplasm. The distributions could be fitted with the sum of two exponential functions. Since the shorter decay component is likely to represent incidental colocalizations of the spots [46], we employed the longer time constants (τ_2) as the dwell lifetimes throughout this report. As the dwell time for each colocalization event, since the recruited molecules are temporarily immobilized in the cluster, we measured the immobilized period in the cluster (see **STAR Methods**) (n_{cells} = 10, n_{events} = 1,364 and 581 for talin and zyxin, respectively). The talin clusters were detected with Halo7-talin labeled with SaraFluor650, and the single molecules of talin and zyxin were detected with SNAPf-talin and SNAPf-zyxin labeled with TMR.

NS, not significant, *, $P < 0.05$, **, $P < 0.01$, using Brunner-Munzel test for (C), Steel-Dwass' test for (D, vs Talin cluster), and Games-Howell's test for (E).

Figure 2. PALM analysis of talin and zyxin clusters

(**A** and **B**) Conventional and PALM super-resolution images (Voronoï diagram) of mEos3.2-talin (A) and mEos3.2-zyxin (B) on the apical and basal PM. The areas surrounded by the green curve (image in the middle) were the regions with good focus (the apical PM is tilted variously) and used for further analysis. The cyan lines in the image on the right indicate the smallest polygon that included the clustered spots.

(**C**) Number densities of the talin and zyxin clusters on the PM, indicating that they are very similar on both the apical PM and the basal PM outside the FA (mean ± SEM, n_{cells} = 15 and 10 for Live SFMT and Fixed PALM, respectively).

(**D**) Distributions of the cluster diameters on the apical PM and basal PM outside the FA, showing that the clusters on the basal PM are slightly smaller than those on the apical PM (n_{cells} = 10, $n_{clusters}$ = 877, 1,065, 3,997, and 3,210 for talin-apical, zyxin-apical, talin-basal, and zyxin-basal, respectively).

(**E**) Distributions of the number of molecules in a cluster located on the apical PM and basal PM outside the FA. The cluster on the basal PM contains slightly more talin and zyxin molecules than those on the apical PM (n_{cells} = 10, $n_{clusters}$ = 877, 1,065, 3,997, and 3,210 for talin-apical, zyxin-apical, talin-basal, and zyxin-basal, respectively).

Figure 3. iTRVZ works as the signaling platform for various signaling pathways

(**A**) Schematic figure showing the FA- and actin-associated proteins examined in this work and their interactions. The numbers in the figure indicate the references (1: [47], 2: [48], 3: [49], 4: [50], 5: [51], 6: [52], 7: [53], 8: [54], 9: [55], 10: [56], 11: [57]).

(**B**) Method for calculating the colocalization index, based on the pair cross-correlation function (PCCF; normalized to the unit area) [17]. Namely, the distances of all pairs of red and green spots in each video frame were calculated for all frames in the movie, and this is done for all the movies (cells). From this data set, the number of pairs at a given distance range (for a bin) is obtained and expressed in the form of the histogram (after the area normalization). The colocalization index is defined as the ratio of the PCCF (0-50 nm) vs. PCCF (450-500 nm), representing the propensities of the molecules to be colocalized (bound). The control PCCF is obtained by shifting the coordinate of each molecule by 1 μm in random angles, and results are shown as the open-box in the boxplot. For details, see **STAR Methods**.

(**C**) Colocalization indices of various Halo7-tagged FA proteins with talin clusters. In the box plots throughout this report, bars, boxes, and whiskers indicate mean values, interquartile range (25–75%), and 10–90% range, respectively (n_{cells} = 20).

(**D**) Colocalization indices of the Halo7-tagged signaling molecules downstream of PDGFR with iTRVZ (n_{cells} = 20).

(**E**) Colocalization indices of PLCγ1-Halo7 and PLCγ1-Halo7 with iTRVZ after various stimulations, and the effects of FAK and SFK inhibitors (n_{cells} = 20).

(**F**) Dwell time of PLCγ1-Halo7 on iTRVZ; prolonged after stimulations (for τ_2, see the caption to **Figure 1J**, n_{cells} = 20, n_{events} = 1,568, 3,894, and 5,232 for no stimulation, +CD59 clustering, and +PDGF, respectively).

(**G**) PDGF-induced increases of the PLCγ1-Halo7 number density (after/before PDGF) outside (bulk) and inside iTRVZ (dots for individual cells and mean ± SEM, n_{cells} = 10).

(**H**) Schematic drawing summarizing the characteristic properties of iTRVZ.

NS, not significant, *, $P < 0.05$, **, $P < 0.01$, using two-tailed Welch's t-test for (C and D), Games-Howell's test for (E), and Steel's test for (F).

Figure 4. PI kinases, some phosphoinositides, PS, and raft domains are colocalized with iTRVZ

(**A**) PIP5K-Halo7 and MARCKS-Halo7 (trajectories) became transiently colocalized with talin clusters (white spots) (**Video S6**).

(**B**) Colocalization indices of Halo7-tagged PI kinases and lipid-binding probes with iTRVZ (data for PI3K are the same as those in **Figure 2D**, n_{cells} = 20).

(**C**) Schematic drawing showing the method for the optogenetic reduction of PI(4,5)P_2 in the PM [24]. CRY2 linked to mScarletI and 5-phosphatase-OCRL (mScar-CRY2-5PT) and CIBN fused to farnesyl-mGFP (localized on the PM cytoplasmic surface) were expressed in talin-rescued dKO MEFs (these cells were used to evaluate the number of talin molecules in an iTRVZ cluster after the treatments). In the dark, CRY2 does not bind to CIBN. Upon blue light irradiation (488-nm laser epi-illumination of the entire cell with a train of 200-ms pulses of 0.64 nW/μm^2 at 0.5 Hz for 30 s), light-activated CRY2 binds to CIBN located on the PM cytoplasmic surface, bringing mScarletI-CRY2-5ptase to induce PI(4,5)P_2 hydrolysis. The PI(4,5)P_2 level in the PM is monitored by the fluorescent probe, two tandemly-linked PH domains of PLCδ fused to SNAPf (SNAPf-2xPH). After the blue light is turned off, CRY2 is slowly deactivated, inducing the release of mScar-CRY2-5PT from the PM. The mScar-CRY2-5PT conjugate of the phosphatase-dead D523G mutant of 5PT was employed as the phosphatase activity-deficient control.

(**D**) Time course of the PI(4,5)P_2 level in the PM determined by imaging SNAPf-2xPH, using confocal microscopy ((D); images in (**Figure S4A**)) (mean ± SEM, n_{cells} = 10). To quantify the PI(4,5)P_2 level in the PM, first, the contour of the cell was determined in the image of SNAPf-2xPH using the ilastik software [58], and then the outer and inner contours of the cell, located

± 1 μm from the cell contour, were defined. The average pixel intensity in the area surrounded by the outer and inner contours (F_{PM}) and that in the cytoplasm (the regions surrounded by the inner contour: F_{cyto}) were measured. Here, F_{PM}/F_{cyto}, normalized by the mean value before light activation, is plotted. The PI(4,5)P_2 level quickly decreased after the blue light irradiation, and by ~10 min after turning off the 30-s irradiation, the original steady-state level was recovered. In contrast, in the cells expressing the phosphatase-dead mScar-CRY2-5PT(D523G), the PI(4,5)P_2 level was not affected by light. Single molecule observations of talin clusters (iTRVZ) were performed before, immediately after, and 15 min after the blue light irradiation (Before, After, and Recovery in (E)).

(**E**) PI(4,5)P_2 plays important roles in recruiting/anchoring talin molecules in iTRVZ as well as in anchoring iTRVZ on the PM cytoplasmic surface, because the mean number of talin molecules in an iTRVZ cluster (cluster size) and the mean iTRVZ number density on the PM (means for all iTRVZ clusters in a cell) were reduced immediately after light irradiation in cells expressing the WT-5PT conjugate (not in those expressing the D523G-5PT conjugate). These values had partially recovered by 15 min after the light irradiation (top row) (n_{cells} = 10). See also **Figure S4B**.

(**F**) Summary of the mean number of Halo7-talin molecules in an iTRVZ cluster after partial depletion of PI(4,5)P_2 and cholesterol. See **Figure S4D and S4E** for the distribution.

(**G**) The number density of iTRVZ (talin clusters) distributed on the apical PM after lipid depletion (mean ± SEM, n_{cells} = 15).

(**H**) Schematic diagram summarizing various signaling processes occurring at iTRVZ.

NS, not significant, *, $P < 0.05$, **, $P < 0.01$, using two-tailed Welch's t-test for (B), Games-Howell's test for (E and G), and Steel-Dwass' test for (F).

Figure 5. iTRVZ cooperatively integrates signaling pathways

(**A**) % Increases of the total number of recruited PLCγ1-Halo7 on iTRVZ (right) and the bulk PM (left) after separate and simultaneous CD59 and PDGFR stimulations in mGFP-zyxin (WT and mutants; **Figure 7A**) -rescued zyxin KO MEFs (n_{cells} = 10).

(**B**) Typical Ca^{2+} mobilization time courses in individual cells (mGFP-zyxin [WT]-rescued

zyxin KO MEFs) after separate and simultaneous CD59 and PDGFR stimulations. The results after normal stimulations by PDGF and anti-CD59 antibody-coated beads (top three curves) and those after much weaker stimulations (1/1,000 PDGF and 1/100 anti-CD59-beads stimulations: bottom three curves. In the figure, anti-CD59 is expressed as aCD59). Note that the y-axis scale for the results of the weak stimulations is two-fold expanded compared with those of the normal stimulations.

(**C**) Total Ca^{2+} signal (the areas below the Ca^{2+} response curves; see (B)), showing that the expression of zyxin IDR rescued the Ca^{2+} response of zyxin-KO MEFs (mean ± SEM, n_{cells} = 143 ~ 283). To examine Ca^{2+} responses, we measured the Ca^{2+} level at the peak as in **figure 4K**. However, for the assay shown in this figure, we measured the integrated Ca^{2+} response, since multiple smaller peaks often appeared under some stimulation conditions employed here.

(**D**) Schematic figure showing that iTRVZ non-linearly integrates the CD59 and PDGFR signals by inducing cooperative interactions of FAK and SFK.

(**E**) Colocalization indices of Halo7-tagged β3 integrin, FAK, Lyn, and PLCγ1 with iTRVZ (SNAPf-talin clusters) after separate/simultaneous weak stimulations by 20 pM PDGF and 20 nM anti-CD59 beads. Horizontal bars, boxes, and whiskers indicate mean values, interquartile ranges (25–75%), and 10–90% ranges, respectively (n_{cells} = 20).

(**F**) Proposed model for cooperative integration of the PDGFR and CD59 signals.

NS, not significant, *, $P < 0.05$, **, $P < 0.01$, using Games-Howell's test for (A, C and D) and two-tailed Welch's *t*-test for (E).

Figure 6. *In-vitro* and *in-cell* phase separation assays for zyxin and VASP

(**A**) Typical confocal fluorescence microscopy images of the mixtures of purified mCherry-zyxin and mGFP-VASP undergoing LLPS. (left) mCherry-zyxin (7.5 μM) and mGFP-VASP (2.5 μM; final concentrations, which are higher than the physiological expression levels; **Figure S6C**) were mixed, and then PEG 8000 (PEG8K) was added at a final concentration of 1%. The co-condensates of zyxin and VASP started forming immediately. After 20 min, 1,6-hexanediol (1,6-HD) was added at a 10% final concentration, which dispersed the co-

condensates, suggesting that the co-condensates were induced by LLPS via the IDR interactions. (right) LLPS found in the zyxin and VASP mixtures at concentrations in the cytoplasms of control MEF line 4 (left), zyxin-KO-MEFs expressing mGFP-zyxin or Halo7-zyxin, and T24 (**Figure S6C**), exhibiting the tendency to form smaller co-condensates at lower concentrations. In contrast, these cells rarely form micron-scale condensates in their cytoplasms, whereas iTRVZs, which are likely to be nanoscale condensates, form abundantly. This might be due to the presence of other proteins and electrolytes in the cytoplasm or perhaps to the high potency of PEG8K to induce LLPS.

(**B**) Distributions of the co-condensate diameters measured from zyxin images ($n_{condensates}$ = 100~152). See also **Figure S6E**.

(**C and D**) Time courses for the growth of the condensates. Typical images of the condensates of zyxin and its mutants (C; **Figure 7A**) and the total signal intensities of the condensates (D) at various time points after the PEG8K addition. The condensate detection and intensity measurements were performed using the in-house single-molecule tracking software. The ΔPr and ΔIDR mutants hardly formed condensates even at 60 min after the PEG8K addition, whereas the wildtype and ΔNC mutant formed condensates within 10 min after the PEG8K addition ($n_{replicates}$ = 20).

(**E** to **H**) *In-vitro* ((E and F); 10 min after 1% PEG8K addition) and in-cell (G and H) FRAP of zyxin and VASP co-clusters (**Video S7**, $n_{droplets}$ = 15). See also **Figure S6F-S6J**.

(**I**) Typical images of iTRVZ (zyxin cluster) showing assembly and disassembly. See also **Figure S6K**.

Figure 7. IDR mediated LLPS is critical for iTRVZ formation and its signaling functions

(**A**) Domain structures of Zyxin, VASP, RIAM, and their mutants used here, with disorder probabilities (shown on the right in magenta). %IDR represents the remaining IDR relative to its wildtype proteins.

(**B**) Colocalization indices of Halo7-tagged zyxin, VASP, RIAM and their mutants with iTRVZ (n_{cells} = 20).

(**C**) Distributions of the copy numbers of mGFP-zyxin (WT and mutants) in an iTRVZ (n_{cells} =

15, n_{spotss} = 2,745 ~ 5,090). Arrowheads indicate median values and mean values are shown in the panel on the right.

(**D** and **E**) Ca^{2+} mobilization after PDGF stimulation. Typical time courses (D) and Fold increase at the peak (E) (n_{cells} = 30).

5 (**F**) Western blot analysis of PDGF-induced Akt phosphorylation ($n_{replicates}$ = 4).

NS, not significant, *, $P < 0.05$, **, $P < 0.01$, using two-tailed Welch's t-test for (B), Games-Howell's test for (B, E, and F), and Steel-Dwass' test for (C).

SUPPLEMENTAL FIGURE TITLES AND LEGENDS

Figure S1. Establishing the talin1/2-double-KO MEF (dKO MEF) lines rescued with tagged talins and zyxin-KO MEF lines with tagged zyxins, related to Figure 1

(**A**) Establishing the talin1/2-dKO MEFs rescued with various tagged talin1s expressed at levels comparable to that of endogenous talin1 in talin2-KO MEFs (parental cell line for generating talin1/2-dKO MEFs). Western blot analysis of the expression levels of talin1 and tagged talin1 in the talin1/2-dKO MEFs rescued with these proteins (talin-rescued dKO MEFs) (mean ± SEM, $n_{\text{replicates}}$ = 4). Since talin1 is the main isoform in most tissues [59], we employed it rather than isoform 2 in this research. Unless otherwise specified, we simply call talin1 "talin" throughout this report. Since the talin-dKO MEF line was generated from the talin2-KO MEFs (as the parental cell line) [11], we used this line as a control. Control MEF lines 1-4 are immortalized MEF lines used as independent controls.

(**B**) Testing the functions of various tagged talins, based on their functions in cell adhesion. Cell attachment at 5 min after plating on fibronectin-coated plastic dishes (mean ± SEM, n_{dishes} = 6). Expression of talin fused to various tag proteins rescued the cell attachment deficiency at levels comparable to that of non-tagged talin, suggesting that the tagged talins are functional, in agreement with the previous report [11].

(**C**) Testing the functions of various tagged talins, based on their involvement in the formation of focal adhesions (FAs) and partitioning into them. Confocal micrographs of talin and tagged talin stained with an anti-talin1 monoclonal antibody in the confocal section near the basal PM, showing that, in rescued cells, the staining patterns of tagged talins, mostly representing those in the focal adhesions (FAs) at the resolution of confocal microscopy, are similar to that of wild-type talin. The contour of the non-rescued cell is shown by a yellow line (these cells do not spread well).

(**D**) Establishing the zyxin-KO MEFs rescued with various tagged zyxins expressed at levels comparable to the average of those of endogenous zyxin in four control MEF lines. Western blot analysis of the expression levels of zyxin and tagged zyxin in the zyxin-KO MEF line rescued with these proteins (mean ± SEM, $n_{\text{replicates}}$ = 4). Since the zyxin-KO MEF line was derived from the zyxin-KO mouse [13], no parental cell line is available. Therefore, the same

MEF lines 1-4 used in (A) were used as independent control MEF lines. The expression levels of tagged zyxin in the zyxin-KO MEF line were adjusted to be about the average of the zyxin expression levels found in these four control MEF lines.

(**E**) Testing the functions of various tagged zyxins, based on their functions in cell adhesion. Cell attachment at 5 min after plating on fibronectin-coated plastic dishes (mean ± SEM, n_{dishes} = 6). Expression of zyxin and tagged-zyxin both *lowered* the cell attachment at 5 min to similar levels, in agreement with the previous report [13], suggesting that the tagged zyxins are functional.

(**F**), Testing the functions of various tagged zyxins, based on their involvement in the formation of FAs and partitioning into them. Confocal micrographs of zyxin stained with anti-zyxin polyclonal antibodies in the confocal section near the basal PM, showing that, in rescued cells, the staining patterns of tagged zyxins, mostly representing those in the focal adhesions (FAs) at the resolution of confocal microscopy, are similar to that of wild-type zyxin.

(**G**) Lifetime distributions of Halo7-talin clusters in zyxin-KO MEFs with and without zyxin re-expression (left), and Halo7-zyxin clusters in talin-dKO MEFs with and without talin re-expression (right). The data were fitted with the sum of two exponential functions (providing the decay times; SEM = fitting error, n_{cells} = 10, n_{spots} = 2,148 ~ 7,273). The long-term (τ_2) decay component virtually disappeared in the cells without talin or zyxin, demonstrating that the talin-zyxin co-cluster lifetime is in the range of 7.7 - 9.5 s in MEFs, whereas the lifetimes of the clusters without talin or zyxin are ~1 s.

NS, not significant, *, $P < 0.05$, **, $P < 0.01$, using Games-Howell's test for (A, B, D, and E) and Steel-Dwass' test for (G).

Figure S2. PALM detection and analysis of talin and zyxin clusters, related to Figure 2

(**A**) Distributions of the durations of the bright and dark states (T_{on} and T_{off}, respectively) and the number of blinks of mEos3.2. The spots in the images were detected by an ImageJ plug-in ThunderSTORM [60] and analyzed by the SR-Tesseler software [16] (n_{cells} = 5).

(**B**) Conventional fluorescence images (basal and apical PM images using total internal reflection and oblique-angle laser illuminations, respectively) and PALM super-resolution

images (Voronoï diagram) of monomer control (mEos3.2-far; mEos3.2 fused to the CAAX motif of K-Ras at Eos3.2's C-terminus). The areas surrounded by green dashed curves are the regions of interest. The cyan lines represent the cluster boundaries. The clusters of mEos3.2-far are hardly detected. To avoid false detection of the clusters, blinking spots were excluded from the dataset, using the "Detection cleaner" function in SR-Tesseler with a 200-frame (3.3 s) maximum search duration, which is sufficiently long to detect >99% of the blinking events [61]. The general control cell line, Talin1/2 dKO, was not used because, either before or after transfection with mEos3.2-far, the cells failed to attach to the cover glass.

(**C and D**) Distributions of the cluster diameters (C) and the number of molecules in a cluster (D) for mEos3.2-far on the apical PM and basal PM outside the FA (n_{cells} = 10, $n_{clusters}$ = 113 and 261 for apical and basal, respectively).

Figure S3. Talin-zyxin clusters existed in all the cells examined here, and we generated the T24-T cell line, T24 cells stably expressing SNAPf-talin, employed extensively for examining the recruitment of FA proteins and signaling molecules to the talin-zyxin clusters (iTRVZ), using the colocalization index method, related to Figure 3

The T24-T cell line expressing SNAPf-talin (T at the end of T24-T represents talin) was created and used for the majority of the experiments for testing the recruitment of FA proteins and signaling molecules to the talin-zyxin clusters (iTRVZ) in the following part of this report. The T24-T line produced here expressed ~1.7x total talin (SNAPf-talin + endogenous talin) as compared with the endogenous talin expressed in the parental T24 cells (see (B)). The parental cell line T24 was selected because single molecules in the apical PM of this cell line could be observed easily due to its flatter apical PM, as compared with other cells examined in this study. The SNAPf-protein tag was used to label talin because we wished to employ the Halo7-protein tag for the molecules we tested for recruitment to the talin clusters. This was because the labeling efficiency of the Halo7 tag was ~88%, whereas that of the SNAPf tag was 66% (**STAR Methods**). Virtually all of the talin clusters would be visible with the lower labeling efficiency of the SNAPf tag (see the caption to B), but since FA proteins and signaling molecules are likely to be monomers/dimers, to observe these molecules using

single-molecule imaging with higher efficiencies, using the tag with higher labeling efficiencies was desirable.

(**A**) Typical images of talin clusters (overexpressed Halo7-talin) in various cell lines. Talin nanoclusters were detected in all of the examined cell lines (apical PM).

(**B** to **D**) Generation of the T24-T cell line, which stably expresses SNAPf-talin. (B) Western blot analysis of the expression levels of talin1 and SNAPf-talin1 (these two bands were not separable and thus we measured the sum of the band intensities) in the T24-T cells. These cells expressed ~1.7 times more talin1 (including SNAPf-talin1) than the wild-type T24 cells (mean ± SEM, $n_{\text{replicates}}$ = 4). Since the labeling efficiency of SNAPf was 66% (**STAR Methods**), altogether 27% of the total talin expressed in the T24-T cell line is fluorescently labeled. (C) Image of SNAPf-talin located on the apical PM of a T24-T cell (which appears similar to the image of Halo7-talin on the apical PM in the parental T24 cell line shown in (A)). (D) Comparison of the number density of talin clusters on the apical PM of the T24-T cells (containing SNAPf-talin) with that of the talin-dKO MEFs rescued with Halo7-talin (mean ± SEM, n_{cells} = 15). The number density in the T24-T cells appears slightly lower than that of the talin-rescued dKO MEFs, probably due to the lower fluorescent labeling efficiency of SNAPf compared with Halo7. Monomer control: Halo7-far expressed in the same cell lines.

(**E and F**) Transient recruitment of the engaged CD59 (clustered by a fluorescent bead coated with anti-CD59 mAb) and Halo7-PDGFR to the SNAPf-labelled talin clusters in T24-T cells, confirming the consistency with their recruitment to Halo7-labelled talin clusters in the Halo7-talin-rescued talin-dKO MEFs (**Figure 1B and 1C**). (E) Typical images showing that the engaged CD59 and PDGFR (trajectories) became transiently colocalized with the SNAPf-labelled talin nanoclusters (white spots) in T24-T cells. (F) The dwell time distributions of the engaged CD59 and PDGFR in the SNAPf-labelled talin clusters (n_{cells} = 20, n_{events} = 3,209, 2,471, 1,485, and 3,261 for CD59 monomer, CD59 cluster, –PDGF, and +PDGF).

(**G** and **H**) Typical image showing that Halo7-FAK (trajectories) became transiently colocalized with iTRVZ (white spots) in T24-T cells after PDGF stimulation (G), with its dwell time distributions both before and after PDGF stimulation (H). FAK molecules were transiently recruited to the talin cluster both directly from the cytoplasm and via the PM by lateral diffusion (**Video S5**) (n_{cells} = 20, n_{events} = 4,690).

(**I**) Colocalization indices of Halo7-tagged JAK1, K-Ras, and Raf1 with iTRVZ (no correlation, n_{cells} = 20).

(**J** and **K**) Number fractions (%, J) and % number increases (K) of PLCγ1-Halo7 recruited to iTRVZ and outside iTRVZ (bulk) in the apical PM after PDGF stimulation (mean ± SEM, n_{cells} = 10). See also the area-normalized data shown in **Figure 3G**.

NS, not significant, *, $P < 0.05$, **, $P < 0.01$, using Brunner-Munzel test for (F, and H) and two-tailed Welch's t-test for (I).

Figure S4. Effects of partial depletions of PI(4,5)P_2 and cholesterol on the iTRVZ (using talin-rescued dKO MEFs), related to Figure 4

(**A**) Representative confocal micrographs of mScar-CRY2-5PT and SNAPf-2xPH, recorded before, immediately after, and 15 min after the blue light irradiation (Before, After, and Recovery, respectively). Both the mScar-CRY2 conjugates of the wild-type 5PT (WT-5PT; left) and D523G-5PT (right) were recruited to the PM after the blue light irradiation, whereas changes in the SNAPf-2xPH signal representing the PI(4,5)P_2 level were observed only in the cells expressing the WT-5PT conjugate of mScar-CRY2-5PT. SNAPf-2xPH were labeled with the SiR-SNAP ligand. See **Figure 4D** for quantification.

(**B**) Typical images of iTRVZ (observed as talin clusters) immediately after the blue light irradiation, showing that the iTRVZ number density in the apical PM and the signal intensity of each iTRVZ cluster (SNAPf-talin) in the cell expressing the WT-5PT conjugate of mScar-CRY2-5PT (left), but not in the cells expressing the phosphatase-dead D523G-5PT conjugate (right), were reduced after the blue light irradiation. See **Figure 4E** for quantification.

(**C**) Representative confocal micrographs of SNAPf-2xPH, showing the reduction of PI(4,5)P_2 levels in the PM after the drug treatments [25]. The Ca^{2+} ionophore ionomycin induces PI(4,5)P_2 hydrolysis by activating the Ca^{2+}-dependent PLC. Phenylarsine oxide and quercetin inhibit phosphatidylinositol 4-kinase, blocking the production of PI(4)P, the main substrate for PI(4,5)P_2 generation.

(**D and E**) Distributions of the number of Halo7-talin molecules in an iTRVZ cluster (n_{cells} =

15, n_{spotss} = 3,159 ~ 8,281), before and after the drug-induced partial depletion of PI(4,5)P_2 (D) and partial cholesterol depletion (E).

NS, not significant, *, $P < 0.05$, **, $P < 0.01$, using Steel-Dwass' test for (D and E).

Figure S5. IDRs of the examined proteins, related to Figure 6 and 7

(**A**) Summary of the IDR contents of the proteins (human) employed in this research, predicted by MobiDB 3.0 [30], showing that many FA- and actin-related proteins contain long IDRs [62]. Magenta shading indicates proteins with total IDR lengths longer than 150 amino acids (a.a.). The LLPS Ref column indicates publications reporting LLPS of the listed proteins (reference numbers in the figure; 1: [63], 2: [64], 3: [65], 4: [66], 5: [67], 6: [68], 7: [43], 8: [69], 9: [70]). Also see [71] and [34].

(**B**) Schematic drawings of the domain structures of the proteins investigated in this study, with their binding-partner molecule names (top) (reference numbers in the figure; 10: [49], 11: [53], 12: [56], 13: [57], 14: [52], 15: [51], 16: [50], 17: [72]) and plots of disorder probabilities (bottom; magenta lines for predicted IDR regions and their total fractions in percentages at the bottom right).

Figure S6. Determination of endogenous expression levels of zyxin and VASP, and *in-vitro* and *in-cell* phase separation assays, related to Figure 6 and 7

(**A to D**) Determination of the cytoplasmic concentrations of endogenous as well as tagged zyxin and VASP. (A) Typical western blot results ($n_{replicates}$ = 4) used to determine the amounts of the endogenous and tagged zyxin and VASP expressed in the cells employed in this study. Using purified mCherry-zyxin and mGFP-VASP proteins, the absolute protein amounts expressed in a cell were determined from the western blot band intensities. (B) The volume of the cytoplasm in a cell, determined by confocal microscopy (see **STAR Methods**). Bars, squares, boxes, and whiskers indicate the median values, mean values, interquartile ranges (25–75%), and 10–90% ranges, respectively. (C and D) The cytoplasmic concentrations (C) and total copy numbers per cell (D) of the endogenous and tagged zyxin and VASP (mean ± SEM, $n_{replicates}$ = 4). The MEFs expressed more zyxin than VASP in all cases.

(**E**) Distributions of the co-condensate diameters measured from VASP images ($n_{condensates}$ =

100~152). See also **Figure 6B**.

(**F and G**) *In-vitro* FRAP observations of micron-scale condensates. Typical time-series of FRAP images of condensates of mCherry-zyxin alone (top) and mGFP-VASP alone (bottom) (10 min after the PEG8K addition), showing that each protein by itself can form condensates (F). FRAP recovery curves (mean ± SEM, $n_{droplets}$ = 10), including the results for the two mixtures of zyxin and VASP at different concentrations (the same curves shown in **Figure 6F**) (G). The fluorescence recovery of the zyxin-only condensates was faster and greater than that of the VASP-only condensates. The condensates made from the 1:3 and 3:1 mixtures of VASP and zyxin exhibited recoveries between those of the VASP-only and zyxin-only condensates.

(**H to J**) In-cell LLPS assay for micron-scale condensates formed by overexpressed zyxin and VASP. Without immense overexpression, micron-scale condensates are rarely found in cells. Dual expression; cells expressing both proteins, Single expression; cells expressing either one of the proteins. (H) In-cell FRAP assays of micron-scale condensates. (I) Typical time-series of the FRAP images of the condensates of mCherry-zyxin alone (top) and mGFP-VASP alone (bottom), showing that each protein by itself can form condensates (**Video S8**). FRAP recovery curves (mean ± SEM, $n_{droplets}$ = 15), including the results for the cells expressing both molecules (the same curves shown in **Figure 6H**). The fluorescence recovery of the zyxin-only condensates was faster and more complete than that of the VASP-only condensates, and the co-expression of ~15 μM VASP and zyxin (J) moderated the differences between the condensates of individual proteins. These results are consistent with the observations made *in vitro* (G). (J) Cytoplasmic concentrations of mCherry-zyxin and mGFP-VASP highly overexpressed in the T24 cells used for the FRAP assays in (H) and (I), as well as in **Figure 4G and 4H** (n_{cells} = 15). The concentrations were determined by confocal microscopy, using various concentrations of purified mCherry-zyxin and mGFP-VASP proteins in PBS as standards. Compared with the T24-cell data shown in (C), mCherry-zyxin and mGFP-VASP were overexpressed by factors of ~18x and ~24x, respectively.

(**K**) Typical images of iTRVZ (talin cluster) showing assembly and disassembly. See also **Figure 6G**.

Figure S7. Generation of zyxin-KO MEF lines rescued with WT and mutant zyxins, and summary of this report, related to Figure 7

(**A**) Domain structures of zyxin and its mutants used here. %IDR represents the remaining IDR relative to the full length zyxin.

(**B**) Typical western blot pattern (top) and band quantification (bottom, mean ± SEM, $n_{replicates}$ = 4) of mGFP-zyxin molecules (WT and mutants) in the cell lines generated from zyxin-KO MEFs by the transfection with their cDNAs. Their expression levels were normalized by the GAPDH band intensities.

(**C**) Distributions (histograms) of the lifetimes of iTRVZ, detected as Halo7-talin clusters in zyxin-KO MEFs expressing mGFP-zyxin (WT and mutants) (n_{cells} = 10, n_{spotss} = 2,584 ~ 5,748). To avoid extreme congestion of the data points, the results are shown in two graphs. All histograms could be fitted by the sum of two exponential functions, providing the exponential decay times (SEM = fitting error). The lifetimes (τ_1 and τ_2) and their fractions are listed in the table on the right. As indicated in **Figure S1G** and its caption, iTRVZ includes the talin-zyxin co-clusters, and the clusters lacking the detectable numbers of either talin or zyxin (containing 0 - 2 copies of talin or zyxin in a cluster): the lifetime of the co-clusters is in the range of 7.7 - 9.5 s, whereas those of the clusters without the detectable numbers of talin or zyxin are ~1 s. Therefore, we conclude that the τ_2 component represents the lifetimes of iTRVZ containing various zyxin mutants. At the same time, these results suggest that iTRVZ is formed by cooperative interactions of proteins, particularly of zyxin and VASP, and that when the cooperative assembly is unsuccessful, the incomplete iTRVZ would be quickly disintegrated.

The τ_2 fractions for all of the mutants exhibited only small variations in the range of 54~68%, whereas that for WT-zyxin was 74%. Therefore, we pay more attention to the τ_2 values. The ΔNC mutant, which is almost solely made of the IDR, prolonged τ_2 to 5.6 s. The deletion of the C-terminal domain (ΔC) has a smaller effect on τ_2, whereas ΔNC, ΔN, ΔPr, ΔIDR, and Phos+ reduced τ_2 more, indicating that the three LIM domains near the N-terminus, the IDR (including the Pro-rich domain), and dephosphorylation enhance iTRVZ formation.

The comparison of the mGFP-zyxin (WT) data here with the results of the non-tagged

zyxin shown in **Figure S1G** supports the proposal that mGFP-zyxin behaves like endogenous zyxin, in terms of the formation of talin-zyxin clusters (iTRVZ).

(**D**) Schematic summary of this report.

(**Top**) iTRVZ platforms constitutively form and bind to the PM cytoplasmic surface via the actin-based membrane-skeleton meshwork [14,45,73] and the PI(4,5)P_2-containing raft domains (**Figure 1D**). They continually form and disperse, and bind to and disengage from the PM inner surface with a lifetime of ~10 s in both the apical and basal PMs (outside the FAs), probably ubiquitously among mammalian cells (**Figure 1F and S3A**). iTRVZ platforms consist of variable numbers of talin and zyxin as well as integrins, RIAM, and VASP (the numbers in an iTRVZ were not examined here), with diameters in the range of 50 - 80 nm (**Figure 2D**). Constituent molecules exchange rapidly with those in the bulk cytoplasm (dwell lifetimes of talin and zyxin ~ 1-2 s) (**Figure 1J**). Therefore, iTRVZ is considered to be a nano-scale liquid.

The iTRVZ formation is promoted by the iTRVZ's proteins' interactions with the raft domains via PI(4,5)P_2, the specific, but weak, multiple interactions of iTRVZ constituent proteins, and the LLPS-inducing interactions of the IDRs of zyxin (**Figure 3C, 4B, and 7B**), VASP, and RIAM (**Figure 7B**; talin does not contain any IDR), as well as the interactions with actin filaments (**Figure 1D**). The number density of iTRVZ on the PM is ~0.25 clusters/μm^2 (**Figure 1E**), which is about the same as that of clathrin-coated structures on the PM [14]. Since the sizes of the PM compartments produced by the actin-based membrane skeleton meshes range between 30 and 250 nm among various cultured cells (~100 nm for T24 cells) [74], an iTRVZ would exist in one out of ~400 compartments in T24 cells. We raise the possibility that cortical actin nodes [75] and GPI-anchored protein-actin filament asters [9,26,76] might also be linked to iTRVZ. The involvement of IDR interactions and LLPS would make the protein compositions of iTRVZ quite flexible.

(**Bottom**) The stimulation-induced engaged receptors, GPI-ARs, RTKs, and GPCRs, and their downstream molecules are recruited to iTRVZ (**Figure 3D and 3E**), where the signal transduction is efficiently performed due to the enhanced molecular collisions by the nano-liquid properties of iTRVZ (see also **Figure 4H**). The crosstalk between different signaling pathways would occur in iTRVZ, inducing the integration of signals from different pathways;

e.g., CD59 and PDGFR (**Figure 5**). Importantly, the integration, detected by the recruitment of PLCg to iTRVZ and the Ca^{2+} responses, occurs nonlinearly: the output signal is far greater than the simple sum of the two signals induced via DC59 and PDGFR individually (**Figure 5A and 5C**). This cooperative non-linear amplification is achieved by the coincidental recruitments of FAK and SFK induced by the activated CD59 and PDGFR, respectively (**Figure 5E**). FAK and SFK activate each other, and with the arrival of the newly recruited molecules, they would undergo spiral activations (also see **Figure 5F**). Since the output signal from the iTRVZ is generated by cooperative amplification of the coincidental inputs, iTRVZ works as an AND gate (coincidence detector) and a noise filter in the noisy cytoplasm (see also **Figure 5D**).

STAR METHODS

RESOURCE AVAILABILITY

Lead contact

Further information and requests for resources and reagents should be directed to and will be fulfilled by the Lead Contact Akihiro Kusumi (akihiro.kusumi@oist.jp)

Materials availability

Plasmids generated in this study are available by request from the Lead Contact.

Data and code availability

Data and codes generated in this study are available by request from the Lead Contact.

EXPERIMENTAL MODEL AND SUBJECT DETAILS

Cells

T24 cells, a kind gift from Masahiro Sokabe (Nagoya University) [77], HeLa cells, purchased from the RIKEN Cell Bank (RCB0007), and CHO-K1 cells, purchased from Dainippon Pharma Co., Ltd., (03-402), were cultured in Ham's nutrient mixture F12 (Sigma Aldrich: N6658) supplemented with 10% (vol/vol) fetal bovine serum (FBS, Gibco: 10270-106, Lot#: 42G7281K). The talin1 and 2 double knockout mouse embryonic fibroblasts (talin-dKO MEFs) and talin2-KO MEFs, kind gifts from Reinhard Fässler (Max Planck Institute of Biochemistry) [11], the zyxin-KO MEF line, a kind gift from Mary C. Beckerle (University of Utah) [13], the control MEF lines 1-3, kind gifts from Noboru Mizushima (University of Tokyo), the control MEF line 4, a kind gift from Ryusuke Kuwahara (Okinawa Institute of Science and Technology Graduate University), and the NIH3T3 cell line, a kind gift from Makoto Kinoshita (Nagoya University) [78], were cultured in Dulbecco's modified Eagle's medium (DMEM, Sigma Aldrich: D5796) supplemented with 10% (vol/vol) FBS, 100 U/ml penicillin, and 100 μg/ml streptomycin (Nacalai Tesque: 26253-84). The mouse embryonic stem cells

(mESCs, clone E14tg2a), purchased from the RIKEN Cell Bank (AES0135, Lot#: 2) [79], were cultured in DMEM supplemented with 15% (vol/vol) embryonic stem-cell qualified FBS (Gibco: 16141079), 1x MEM non-essential amino acids solution (Gibco: 11140050), 1 mM sodium pyruvate (Gibco: 11360070), 55 μM 2-mercaptoethanol (Gibco: 21985023), 100 U/ml penicillin, 100 μg/ml streptomycin, and 10^3 U/ml mouse leukemia inhibitory factor (LIF, Millipore: ESG1106) without feeder cells [80]. The identities of the T24 and HeLa cell lines were authenticated by PowerPlex16 STR (contracted to Promega). All of the cells used were mycoplasma free, as determined by using a Mycoplasma PCR Detection Kit (Beyotime Biotechnology: C0301S) and VenorGeM Mycoplasma Detection Kit (Minerva Biolabs: MNV11-1100).

METHOD DETAILS

Cell transfection

The transfection of cells with the plasmid vectors was performed by electroporation with a Lonza 4D-Nucleofector, according to the manufacturer's recommendations, using the SF solution and program EN138 for T24 and NIH3T3 cells; SE and CN114 for HeLa cells; SF and DT133 for CHO-K1 cells; SE and DS150 for talin-dKO MEFs; SF and CZ167 for other MEFs; and SF and CG104 for mESCs.

For the generation of cell lines stably expressing selected proteins, the cells were transfected with the expression vector (for the pPBpuro expression vector, pCMV-mPBase was co-transfected). Two days after transfection, the cells were selected by an incubation with G418 (800 μg/ml for T24, 1,000 μg/ml for MEFs) or puromycin (0.5 μg/ml for T24, 1 μg/ml for MEFs). After an incubation in the selection medium for a week, the cell lines were cloned by limiting dilution using 96-well plates. The expression levels of isolated cell clones were examined by western blotting and immunofluorescence microscopy. The established stable cell lines were routinely cultured in the presence of antibiotics.

For fluorescence microscopy, the cells were plated in a glass-bottom dish with a glass window size of 12 mm in diameter (No.1S, Iwaki: 3971-035), pre-coated with fibronectin (FN, Sigma Aldrich: F1141) by placing 100 μl of 10 μg/ml FN in phosphate buffered saline

(PBS: 137 mM NaCl, 8.1 mM $NaHPO_4$, 2.7 mM KCl, 1.5 mM KH_2PO_4, pH 7.4) on the glass at room temperature (RT) for 30 min. The cells were cultured in the complete growth medium for 24–48 h before use. For cell stimulation experiments using epidermal growth factor (EGF) and platelet-derived growth factor (PDGF), the cells were pretreated with the FBS-free medium for 3-12 h. For microscope observations, the medium was replaced by Hanks' balanced salt solution (Nissui: 05905) buffered with 2 mM TES (Dojindo: 348-08371) at pH 7.4 (observation medium; T-HBSS).

For the expression of the CRY2 protein, transfected talin1/2-dKO MEFs were first incubated in the complete growth medium at 37ºC for 2 h for recovery from the transfection, and then cultured at 33ºC for 2 days, to allow for better folding of the CRY2 protein, followed by the incubation at 37ºC for 3 h before microscope observations.

Cell stimulation

CD59 and Thy1 were activated by polystyrene beads coated with the respective monoclonal antibodies. Mouse anti-CD59 and mouse anti-Thy1 monoclonal antibodies were purified from the culture media of hybridoma MEM43/5 (a kind gift from Vaclav Horejsi [Institute of Molecular Genetics of the Czech Academy of Sciences]) [81] and hybridoma OX7 (European Collection of Cell Cultures: 84112008) [82,83], respectively. The carboxylate-modified yellow-green or dark-red fluorescent 40-nm polystyrene beads (Molecular Probes: F8795, F8789, respectively; final concentration of 0.4 μM) were functionalised by incubating them at RT for 10 min in the activation solution, containing 2 mM 1-ethyl-3-(3-dimethylaminopropyl)carbodiimide (EDC, Pierce: 22980), 4 mM sulfo-N-hydroxysuccinimide (sulfo-NHS, Pierce: 24525), and 150 mM NaCl, buffered with 0.1 M 2-(N-morpholino)ethanesulfonic acid (MES) at pH 5.5. Afterwards, a 9 μl portion of the antibody (1 mg/ml in PBS) was mixed with 3 μl functionalized beads, 3 μl borate -buffered saline (150 mM NaCl buffered with 0.5 M borate [Wako: 021-02195] at pH 8.0), and 1 μl 0.4 M NaOH. After an incubation at RT for 1 h, the coupling reaction was stopped by the addition of 7.5 μl of 300 mM glycine and 1 μl of 5% polyethylene glycol with a mean molecular weight of 20,000 (PEG20K, Sigma Aldrich: P5413) in PBS and incubated at RT for 5 min. The mixture was ultracentrifuged (50,000 rpm for 15 min), and then the antibody-coated beads were

resuspended in 1 ml PBS containing 0.1% PEG20K, ultracentrifuged again, and resuspended in T-HBSS containing 2% bovine serum albumin (BSA, Sigma Aldrich: A3059) and 0.1% PEG20K. Right before use, the bead suspension was sonicated for 5 min, followed by centrifugation (15,000 rpm for 10 min). The cells were first incubated in T-HBSS containing 0.5% BSA and 0.1% PEG20K, and then the bead suspension was added at a final concentration of 2 μM or 20 nM. The observations were finished within 10 min after the bead addition to avoid the effect of internalization.

Stimulations of the receptor-type kinases (RTKs) were performed by incubating the cells with 20 nM human recombinant EGF (Wako: 053-07871), 20 nM or 20 pM human recombinant PDGF-BB (Pepro Tech: 100-14B), and 100 μM uridine triphosphate (UTP, Invitrogen: R0471). All microscope observations were finished within 5 min after the stimulation.

Cell treatments with various reagents

The kinase activity of Src family kinases (SFKs) was inhibited by treating the cells with 10 μM PP2 (Selleckchem: S7008) [84] at 37°C for 10 min. The kinase activity of focal adhesion kinase (FAK) was inhibited by treating the cells with 10 μM PF573228 (Cayman Chemical: 14924) [85] at 37°C for 10 min.

Partial actin depolymerization was performed by incubating the cells in medium containing 100 nM latrunculin A (Wako: 125-04363), 500 nM cytochalasin D (Cayman Chemical: 11330), or 10 μM Y27632 (ChemScene: CS-0878) for 10 min at 37°C. Partial depletion of cholesterol was achieved by incubating the cells in 4 mM methyl-b-cyclodextrin (MβCD, Sigma Aldrich: 332615) at 37°C for 30 min or in 60 μg/ml saponin (Nacalai Tesque: 30502-42) on ice for 15 min [38]. Replenishment of cholesterol was performed by incubating the cholesterol-depleted cells in 10 mM MβCD-cholesterol complex (1:1 mol/mol; Sigma Aldrich: C3045) at 37°C for 30 min [38]. Partial depletion of PI(4,5)P_2 from the PM was performed by incubating the cells with 10 μM ionomycin (Wako: 093-04531) at 37°C for 5 min [86], 1 μM phenylarsine oxide (Tokyo Chemical Industry: P0140) at 37°C for 3 h, or 50 μM quercetin (Sigma Aldrich: Q4951) at 37°C for 3 h [25,87].

To inhibit the interactions between the intrinsically disordered regions (IDRs) of the

proteins, cells were first lightly permeabilized with 1% Tween 20 in T-HBSS at RT for 10 min, and then treated with T-HBSS containing 5% 1,6-hexanediol (Wako: 081-00435) on the microscope stage during observation. The microscope observations were finished within 10 min [88]. For *in vitro* experiments, 1,6-hexanediol was added at a final concentration of 10%.

cDNA construction

Plasmids were constructed using standard techniques in molecular biology and confirmed by DNA sequencing. All plasmids used in this study are listed in **Table S1**, and the complete plasmid sequences in the GenBank format with annotations are shown in **Data S1**. The cDNAs encoding SNAPf, Halo7, mEGFP, and mCherry were obtained from New England Biolabs (N9172S), Promega (G9651) and Clontech (Z2370N, Z2522N), respectively. The cDNA encoding mEos3.2 was generated by making 3 point-mutations, I102N, H158E, and Y189A, in the Addgene mEos2 plasmid (#20341), a kind gift from Loren L. Looger (Janelia Research Campus) [89–91]. The cDNAs encoding the deletion mutants of RIAM, VASP, and zyxin were generated by PCR with designed primers. The cDNAs encoding phosphomimetic and phosphodeficient mutants of zyxin and VASP were custom synthesized by Gene Universal. The cDNAs encoding mScarlet-I [92], domain 4 from perfringolysin O with the D434S mutation (D4H) [93,94], and ostreolysin A with the E69A mutation (OlyA [E69A]) [23] were custom synthesized by Sangon Biotech (Shanghai, PRC).

The cDNAs encoding the following proteins were kind gifts from researchers. Mouse FAK (Caroline H. Damsky, University of California, San Francisco) [95]; human RIAM (Chinten J. Lim, University of California, San Diego) [96]; human β3 integrin (Jonathan C. Jones, Northwestern University) [97]; rat N-WASP (Jack Taunton, University of California, San Francisco) [98]; mouse PIP5KIγ (Richard A. Anderson, University of Wisconsin) [99]; probes for PI(4)P, PI(3,4)P_2, PI(4,5)P_2, and PI(3,4,5)P_3 (Toshiki Itoh, Kobe University) [21]; a probe for phosphatidylserine (Tomohiko Taguchi, Tohoku University) [27,100]; CIBN and CRY2-5ptase (Pietro de Camilli, Yale University) [24]; human CD59 (Masahide Tone, Oxford University) [101]; rat Thy1 (Roger J. Morris, King's College London) [82]; human PDGFR-β (William Hahn, Broad Institute of MIT and David Root, Harvard University) [102]; rat PLCγ1 (Matilda Katan, Cancer Research UK Centre) [103]; mouse PLCβ1 (Katsuhiko Mikoshiba,

ShanghaiTech University) [104]; human K-Ras and human Raf1 (Akihiko Yoshimura, Keio University) [105]; and human CD47 (Eric C. Brown, Genentech) [106].

The five-amino acid linker sequence (Ser-Gly-Gly-Gly-Gly) was inserted between the target protein and mGFP, mCherry, and mScarlet-I, and the 15-amino acid linker ((Ser-Gly-Gly-Gly-Gly)$_3$) was inserted between the target protein and SNAPf, Halo7, and mEos3.2.

The sequences encoding various proteins were subcloned into the following vectors: pEGFP, pmCherry (Clontech: Z2370N, Z2522N), pET26B (Novagen: 69862), and pPBpuro (a custom vector with the PiggyBac terminal repeat sequence and the high expression promoter consisting of chicken beta actin promoter, CAG promoter with an artificial intron, and CMV IE, a kind gift from Michiyuki Matsuda, Kyoto University) [107]. pCMV-mPBase was a kind gift from Michiyuki Matsuda (Kyoto University) [107].

Western blotting

Ice-cold radio immunoprecipitation assay (RIPA) buffer, consisting of 150 mM NaCl, 5 mM ethylenediaminetetraacetic acid (EDTA, Dojindo: 345-01865), 1% NP-40 (Wako: 141-08321), 1% sodium deoxycholate (Nacalai Tesque: 08805-72), 0.1% sodium dodecyl sulfate (SDS, Wako: 191-07145), and 100x diluted protease inhibitor cocktail (Nacalai Tesque: 25955-24), buffered with 50 mM tris(hydroxymethyl)aminomethane (Tris)-HCl at pH 7.4 (350 µl) (100x diluted phosphatase inhibitor cocktail [Nacalai Tesque: 07574-61] was included for the Akt phosphorylation assay), was added to cells cultured to ~80% confluency in a 60-mm plastic dish, and kept on ice for 5 min. The entire material in the dish was collected by using a cell scraper, and then centrifuged at 15,000 rpm for 20 min. The supernatant (300 µl) was mixed with 100 µl of 4x Laemmli sample buffer, consisting of 8% SDS, 0.12% bromophenol blue, 40% glycerol, and 400 mM dithiothreitol, buffered with 200 mM Tris-HCl at pH 6.8, and boiled for 5 min. The boiled mixture (2 ~10 µl, 1~2 µg of total protein for each lane) was loaded on a precast 4-20% gradient polyacrylamide gel (PAGE, Bio-Rad: 4561096) and electrophoresed at a constant voltage of 200 V for 35 min, using a Mini Protean Tetra Cell (Bio-Rad: 1658000JA), in Tris-glycine running buffer (25 mM Tris-HCl, 190 mM glycine, and 0.1% SDS). The direct addition of the 4x Laemmli buffer to the cells gave virtually the same results, but the background of the western blot membrane was higher, and thus we performed

the initial cell solubilization with the RIPA buffer.

The proteins separated by SDS-PAGE, zyxin, VASP, and Akt, were blotted onto polyvinylidene fluoride (PVDF) membranes by the semi-dry transfer method, using a Trans-Blot Turbo (Bio-Rad: 1704150, mixed MW protocol) with the PVDF transfer pack (Bio-Rad: 1704156). In the case of talin, the wet transfer to the PVDF membrane (Immobilon-P, Millipore: IPVH00010) was performed using a running buffer containing 25 mM Tris-HCl, 190 mM glycine, and 20% methanol at 4ºC, with a constant voltage of 100 V for 1 h (Mini Protean Tetra Cell). The immuno-detection was performed by a SNAP i.d. (Millipore, SNAP2BASE), according to the manufacturer's recommendations. The membranes were blocked with Blocking One (Nacalai Tesque: 03953-95) and washed with Tris-buffered saline (TBS; 137 mM NaCl and 2.7 mM KCl buffered with 25 mM Tris-HCl, pH 7.4) supplemented with 0.1% Tween 20 (TBS-T).

Primary antibodies were as follows: mouse anti-talin1 (clone 93E12, Abcam: ab104913, Lot#: GR24449-3, 0.5 μg/ml), rabbit anti-zyxin (B71, Millipore: ABC1463, Lot#: Q3027780, 4,000x dilution), rabbit anti-GFP (ProteinTech: 50430-2-AP, Lot#: 78456, 0.5 μg/ml), rabbit anti-VASP (clone 9A2, Cell Signaling Technology: 3132, Lot#: 5, 21 ng/ml), rabbit anti-Akt (Cell Signaling Technology: 9272, Lot#: 5, 17 ng/ml), rabbit anti-phospho-Akt (pS473, clone D9E, Cell Signaling Technology: 4060, Lot#: 25, 48 ng/ml), mouse anti-GAPDH (ProteinTech: 60004-1-Ig, Lot#:10008047, 10 ~ 500 ng/ml). Secondary antibodies were the following: horseradish peroxidase (HRP)-conjugated goat anti-mouse immunoglobulin G (IgG, Invitrogen: G21040, Lot#:2122350, 0.5 μg/ml) and HRP-conjugated goat anti-rabbit IgG (Invitrogen: G21234, Lot#:2087715, 0.5 μg/ml).

The membrane was then incubated with Western BLoT Hyper HRP Substrate (Takara: T7103B) for chemiluminescence detection, and then imaged with an LAS-3000 (Fuji Film, high sensitivity mode) or iBright FL1500 (Thermo Fischer Scientific, 2x2 binning, 1.5x zoom) image analyzer. Quantitative analysis of the protein bands was performed with the ImageJ software. The signal intensities were normalized by the GAPDH intensities. To measure the phosphorylation of Akt, the membrane was first treated and imaged to measure Akt phosphorylation, and then the bound antibodies and the chemifluorescent product were removed by incubating the membrane with stripping buffer, consisting of 2% SDS and 100

mM 2-mercaptoethanol buffered with 62.5 mM Tris-HCl at pH 6.7, at 50ºC for 20 min, followed by reprobing with the anti-Akt antibodies.

Cell attachment assay

Cultured cells (in 100-mm plastic dishes, ~80% confluence) were detached with a freshly prepared trypsin solution (0.25% trypsin and 1 mM EDTA in PBS) at RT for 3 min. After brief centrifugation (1,000 rpm for 3 min), the cells were resuspended in the complete growth medium, and the cell number was determined with a hemocytometer. The cell concentration was adjusted to 3 x 10^4 cells/ml and the cells were incubated in the CO_2 incubator at 37ºC for 30 min, for recovery from the detachment process. Afterwards, 1 ml of the cell suspension was dispensed into each FN-coated well in the 12-well plastic plate, which was then placed in the CO_2 incubator for 5 min. The plate was then gently washed twice with T-HBSS, and the cells were imaged by a ZEISS Primovert Photo inverted phase-contrast microscope. The numbers of attached cells were counted by the ImageJ software.

Fluorescence labeling of molecules

To fluorescently label the SNAPf and Halo tags bound to target proteins expressed in cells, the cells were incubated at 37ºC in complete growth medium containing either 50 nM SNAP-tetramethylrhodamine (TMR) star (New England BioLabs: S9105S) for 60 min, or 20 nM TMR-Halo linker (Promega: G8251), 20 nM SaraFluor650T Halo linker (SF650, Goryo Chemical: A308-02), or 100 nM JF646 Halo linker (Promega: GA1120) for 30 min. The labelling efficiencies (including the misfolding, slow folding, and cleavages of the tag proteins) were estimated to be 66 ± 1.8% for SNAPf, 88 ± 2.2% for Halo7, and 76 ± 2.3% for mEGFP, using the control monomeric molecules mEGFP-CD47-SNAPf and mEGFP-CD47-Halo7 (SNAPf and Halo7 tags located in the cytoplasm). Unless otherwise noted, Halo7 and SNAPf tags were labeled with SaraFluor650 Halo-ligand and SNAP-TMR star, respectively.

Immunofluorescence labeling

The cultured cells on the FN-coated glass-base dish were fixed with cold methanol (-20ºC) for 5 min for talin staining or 4% paraformaldehyde for 1 h for zyxin staining. The fixed cells

were incubated at RT with 100 mM glycine for 15 min, 0.1% Triton X-100 for 5 min, and then 1% BSA for 1 h (all solvents were PBS containing 0.1% Tween 20; PBS-T). The cells were immunostained by sequential 1 h incubations with primary and secondary antibodies at RT. Each incubation was followed by three washes with PBS-T.

The following antibodies were used: mouse anti-talin1 (clone 97H6, Bio-Rad: MCA4770, Lot#:1803, 1 μg/ml), rabbit anti-zyxin (B71, Millipore:ABC1463, Lot#: Q3027780, 600x dilution), Rhodamine Red-X-conjugated donkey anti-mouse IgG (Jackson: 715-295-150, Lot#: 145566, 1 μg/ml), and Rhodamine Red-X-conjugated donkey anti-rabbit IgG (Jackson: 711-295-152, Lot#: 145693, 1 μg/ml).

Single fluorescent-molecule imaging and analysis

All single-molecule observations were performed at 37°C, using a microscope housed in a home-made environmental chamber. Fluorescently labeled molecules in cells were excited by total internal reflection (TIR) illumination (for those on the basal PM) or oblique-angle illumination (for those on the apical PM) using objective-lens-type TIRF microscopes, which were constructed on Olympus and Nikon inverted microscopes (IX-83 and TiE, respectively) equipped with 100x 1.49 NA objective lenses (UApoN100XTIRF and ApoTIRF100XC, respectively). The two-color fluorescence images were separated into the two detection arms of the microscope by a dichroic mirror (Chroma: ZT561rdc-UF3 or ZT640rdc-UF3). The detection arms were equipped with band-pass filters of ET525/50m, ET600/50m, or ET700/75m (all from Chroma), and the images were recorded at each arm with a two-stage microchannel plate intensifier (Hamamatsu Photonics: C9016-02MLP24), lens-coupled to a scientific complementary metal oxide semiconductor (sCMOS) camera (ORCA-Flash ver4.0 V2 plus, Hamamatsu Photonics: C11440-22CU). The final magnifications were 133 and 100x, resulting in pixel sizes of ~50 and 65 nm (square pixels), respectively.

The incident excitation laser powers at the sample plane for single molecule observations with the oblique illumination were 0.29 μW/μm^2 for the 488-nm line (for mEGFP, Coherent: OBIS 488-100 LS), 0.21 μW/μm^2 for the 561-nm line (for TMR, Coherent: OBIS 561-100 LS), and 0.37 μW/μm^2 for the 642-nm line (for SF650 and JF646, Omicron: LuuXPlus 640-140). For the TIRF illumination, we employed very shallow angles and 2x-increased incident laser

powers. Under these conditions, the photobleaching lifetimes for fluorophores on the apical PM with the oblique-angle illumination (basal PM with the TIR illumination) were the following: mEGFP, 0.61 ± 0.02 (0.74 ± 0.02) s; SNAPf-TMR, 3.65 ± 0.15 (3.68 ± 0.18) s; Halo7-TMR, 8.87 ± 0.47 (9.50 ± 0.48) s; Halo7-SaraFluor650, 12.69 ± 0.57 (14.38 ± 0.53) s; and Halo7-JF646, 11.12 ± 0.62 (12.01 ± 0.54) s. For the cluster (iTRVZ) observations, the laser powers were reduced by a factor of three from those used for single molecule observations. The dual-colour images were separated by a dichroic mirror (Chroma: ZT561rdc-UF3 or ZT640rdc-UF3) and projected into two detection arms with band-pass filters of ET525/50m, ET600/50m, or ET700/75m (all from Chroma).

Each individual fluorescent spot in the image was identified and tracked by using an in-house computer program, as described previously [14,45,90,91]. The superimposition of images in different colors obtained by two separate cameras was conducted as described previously [108].

Transient-immobilization events, called Temporary Arrest of LateraL diffusion (TALL [109,110]), were detected in single-molecule tracking trajectories, by using the algorithm developed [111] and modified [109,110] previously. The detection circle radius and the threshold residency time were set at 200 nm and 5 frames (0.167 s), respectively. The cluster lifetimes and molecular dwell lifetimes on iTRVZ should in principle be corrected for the photobleaching lifetimes of the probes [110], but since the observed durations were much shorter than the probes' photobleaching lifetimes, no corrections were performed.

Colocalization index analysis

To quantitatively measure the colocalization of single molecules with iTRVZ clusters (talin and zyxin clusters), since the sizes of the cluster images are virtually the size of the light diffraction limit (they appear like single-molecule spots in terms of their sizes), we employed a "colocalization index" parameter, based on the pair cross-correlation analysis for single-molecule movies simultaneously recorded in two colors (such as green and red) [17,112], as shown in **Figure 3B**. Briefly, (1) a region of interest (ROI) is selected, and then the distances between all pairs of green and red spots in the ROI in a video frame are measured, and this is repeated for all of the video frames in an image sequence. (2) The distribution of the

number of distances $R(r)$ is plotted against the distance. The normalization factor $N(r)$ is computed using fast Fourier transform, as described [17,112]. (3) The cross-correlation function $C(r)$ is calculated by dividing $R(r)$ by $N(r)$. (4) The colocalization index is defined as the ratio of the value of the pair correlation function between 0 and 50 nm and the value between 450 and 500 nm. When no significant colocalization exists, the colocalization index is 1, and with an increase of colocalizations, the index increases. The control data without any correlation between green and red spots were produced by shifting each spot in the image by 1 μm in random directions.

PALM observation and analysis

Cells expressing the proteins conjugated with mEos3.2 were chemically fixed for PALM observations. Briefly, cells were initially fixed with 0.3% (v/v) glutaraldehyde in cytoskeleton buffer (150 mM NaCl, 5 mM EGTA, 5 mM glucose and 5 mM $MgCl_2$, buffered with 10 mM MES at pH 6.1) containing 0.25% (v/v) Triton X-100 for 1 min, and then post-fixed with 2% (v/v) glutaraldehyde in the same solution for 15 min [113]. The cells were then incubated with freshly prepared 0.1% (w/v) sodium borohydride for 7 min to quench the unreacted aldehyde groups. After replacing the cytoskeleton buffer with T-HBSS, the fixed cells were observed at 37°C by a home-built PALM station.

The PALM station is virtually the same objective-lens-type TIRF microscope developed for single-molecule imaging, based on an Olympus IX-83. The samples were illuminated with the TIR or oblique-angle illumination mode, using an activation laser (405-nm, Cobolt: 06-MLD 405-100; increased from 1.5 to 78 nW/μm^2 on the sample plane following the Fermi photoactivation scheme [t_F = 162, T = 16.2 s] [114]), an excitation laser (561-nm, MPB Communications: Fiber 560-20000; 12.4 μW/μm^2), and an additional weak 488-nm laser to suppress the long-lived dark state [61] (Coherent: Sapphire 488-300 CW; 0.164 μW/μm^2). The PALM data acquisition was performed at 60 Hz for 14,560 frames with an image size of 512 x 512 pixels, using the high-speed camera system (Photron: mini AX200-II) described previously [90,91]. The final magnification was 250x (~80 nm/pixel; square pixels).

The detection of the spots in the images was performed by using the ThunderSTORM plugin of ImageJ [60] with “Wavelet filtering” (B-Spline order = 3 and B-Spline scale = 2.0) and

the “Local maximum method” (Peak intensity threshold = 30 ~ 50 and Connectivity = 8-neighborhood). After the spot detection, the post-processing steps of “Remove duplicates” (Distance threshold = uncertainty) and “Drift correction” (cross-correlation with 5 bins) were further performed. These datasets were imported to the SR-Tesseler software [16] for the cluster analysis and image reconstruction. First, the areas with good focus in the apical PM and those that do not contain obvious FAs were selected as ROI. Second, blinking and multi-ON frame detections were corrected by the “Detection cleaner” function using the following parameters: photon/background size = 0.3; fixed maximal dark time = 200; intensity to photon ratio = 0.039; and background value = 0.3 (**Figure S2A**) [61]). Third, cluster contour detection was performed by using a Voronoï polygon density factor of 3.5 (within the whole ROI).

Confocal microscopy and FRAP

To obtain confocal fluorescence images of the cells at 37ºC, we employed a custom-built spinning-disk confocal microscope based on an Olympus IX83 (placed in a home-built environmental chamber) equipped with an Olympus objective PLXApo60XO or UApoN100XTIR, a Yokogawa confocal unit, CSU-W1, and a Hamamatsu Photonics ORCA-Flash 4.0 V2 plus sCMOS camera.

For the in-cell fluorescence recovery after photobleaching (FRAP) experiments, we employed a Nikon A1R confocal microscope equipped with a stage top incubator (Tokai hit, STXG-TIZWX-SET) operated at 37ºC, with recordings at 0.5 Hz. The photobleached-observed area was a circular region of ~1 μm in diameter, and photobleaching was performed by illuminating the area with a 488 or 561 nm laser beam at 30% of the full laser power for ~1 s. For the *in vitro* FRAP experiments, a mixture of purified proteins was diluted with the observation buffer (150 mM NaCl and 0.5 mM tris(2-carboxyethyl)phosphine) [TCEP] buffered with 25 mM Tris–HCl, pH 7.4). After the addition of a final concentration of 1% PEG8K (Sigma Aldrich: P5413), the mixed solution was placed on the glass-bottom slide (Ibidi: 81507) and observed at 37ºC and 1 Hz by a Nikon spinning-disk confocal microscope, consisting of a Nikon TiE inverted microscope, a Nikon PlanApo 60x/1.40 objective lens, a Yokogawa CSU-X confocal unit, an Andor Revolution SD System, an Andor iXon 888-U3ultra camera, and an OkoLab stage top incubator. The photobleached-observed area was a

circular region of ~1.5 μm in diameter, and photobleaching was performed by illuminating the area with a 488 nm laser beam (3.9 mW) for 0.5 s. The intensity recovery traces were analyzed (background corrected and normalized) by the Image J software, based on the previously described method [115].

Cell volume measurement

The cells were transfected with the plasmid encoding SNAPf (without any fusion proteins), and plated on the FN-coated glass-bottom dishes. After culturing for 48 h, the expressed SNAPf proteins were labelled with 20 nM SNAP-TMR star at 37ºC for 30 min. After washing three times with T-HBSS, the medium was replaced with 1,000x diluted NucSpot Live 650 (Biotium, 40082) in T-HBSS for nuclear staining. Without washing, the whole 3D cell images were captured by Z scanning (250 nm pitch) with an Olympus custom-built spinning-disk confocal microscope.

The obtained images were binarized by the ImageJ software with Otsu's binarization algorithm [116]. The volumes of the whole cell and the nucleus were determined from the binarized images of SNAPf and NucSpot Live 650, respectively, by counting the total voxel numbers. The volume of the cytoplasm was calculated by subtracting the nucleus volume from the whole cell volume.

Measurements of intracellular Ca^{2+} concentrations

The cells were incubated with 20 μM CalBryte 590 (AAT Bioquest: 20700) in T-HBSS at 37ºC for 30 min, and then washed three times with T-HBSS. The cells were observed at 37ºC by a home-built objective-lens-type TIRF microscope (Nikon TiE-base) equipped with a Nikon Plan Fluor 20x/0.50 objective lens. The cells were illuminated by a 561 nm laser at the Epi angle at a laser power of 0.22 nW/μm^2 on the sample. Recordings were performed at 1 or 2 Hz. To avoid the incorporation of CalBryte 590 in endosomes by endocytosis, all observations were finished within 1 h after labelling.

Protein purification

For preparing the cholesterol probe (Halo7 tag fused to D4H [93,94]) and sphingomyelin probe

(Halo7 tag fused to OlyA(E69A) [23]), BL21 (DE3) *E. coli* competent cells (New England BioLabs: C2527) were transfected with the expression plasmids by heat shock, and then cultured at 37˚C in Luria-Bertani medium containing 50 μg/ml kanamycin, with agitation until the optical density at 600 nm reached 0.4 ~ 0.6. The cells were further cultured with 0.6 mM isopropyl-β-D-thiogalactopyranoside (Amresco: MFCD00063273) at 24˚C for 12 h. The cells were collected by centrifugation at 7,000 rpm for 3 min, resuspended in lysis buffer (1% Triton X-100 and 300 mM NaCl buffered with 20 mM Tris-HCl, pH 8.0) containing the protease inhibitor cocktail (Nacalai Tesque: 25955-24), and then disrupted by agitation on ice for 20 min. The suspension was centrifuged at 12,000 rpm for 10 min, and the supernatant was filtered through a Millex filter (0.45 μm pore; Millipore: SLFH05010) to remove the cell debris. The filtered solution was loaded on a column packed with nickel-nitrilotriacetic acid (Ni-NTA) agarose beads (Sangon Biotech: C600332-0001), and the bound proteins were eluted by the sequential additions of 10 mM (10 ml), 20 mM (10 ml), and 30 mM (5 ml) imidazole (all in 150 mM NaCl buffered with 20 mM Tris-HCl, pH 8.0), and finally, of 10 mM imidazole in 250 mM NaCl buffered with 20 mM Tris-HCl, pH 8.0 (10 ml). The eluted fractions were desalted and concentrated with an Amicon Ultra concentrator (10 kDa cutoff, Millipore, UFC501008) with 150 mM NaCl buffered with 20 mM 4-(2-hydroxyethyl)-1-piperazine ethanesulfonic acid (HEPES), pH 7.4. The probe concentrations were determined according to the optical absorbance at 280 nm, assuming molecular extinction coefficients of 1.02 and 0.977 x 10^5 (M/cm) for Halo7-D4H and Halo7-OlyA(E65A), respectively (determined from the amino acid composition data [117]). To label probes with the SeTau647-Halo ligand [110], purified probes were incubated with 1.5 equivalents of SeTau647-Halo ligand at 37 ˚C for 3 h. The labelled proteins were separated from the unreacted ligand by Ni-NTA affinity column chromatography, followed by concentration-purification using an Amicon Ultra concentrator, according to the same protocol described for the initial purification of Halo7-D4H and Halo7-OlyA(E65A). Their purities were 71 and 90%, respectively, as determined by the Coomassie Brilliant Blue R-250 (CBBR, Fluka: 27816) staining of the SDS-PAGE gels. Aliquots (30 μl) of the labelled protein solutions were placed in Eppendorf tubes, rapidly frozen in liquid N_2, and stored at -80ºC until use.

For the preparation of zyxin (and its mutants) and VASP, the proteins were expressed as

chimeric proteins with a 6xHis tag, maltose binding protein (MBP), Tobacco Etch Virus protease digestion sequence (TEV), mCherry (GFP for VASP), and zyxin (VASP) in Expi293F cells (Thermo Fisher Scientific: A14635) for three days. The cells were harvested and lysed by freeze-thawing in buffer A (200 mM NaCl, 1 mM EDTA and 0.5 mM TCEP buffered with 25 mM Tris-HCl, pH 7.4) supplemented with protease inhibitor cocktail (cOmplete, ETDA-free, Roche: 11873580001) at RT. The lysates were centrifuged at 21,000g at 4ºC for 1 h, and then purified according to a two-step protocol. The first step was affinity purification on an MBP-binding dextrin Sepharose column (MPBTrap, GE Healthcare: 28-9187-78). The lysates were loaded twice on the column at a flow rate of 0.5 ml/min, and eluted with 10 mM maltose in buffer A at RT. The eluates were incubated with TEV protease (1:10 total protein weight) at 16ºC for 18 h to cleave the TEV sequence. The second step was the separation of mCherry-zyxin or EGFP-VASP from 6xHis-MBP and the removal of the His-tagged TEV protease by Ni-NTA chromatography (HisPur™ Ni-NTA Resin, Thermo Scientific: 88222). First, NaCl and imidazole were added to the digested solutions at final concentrations of 400 and 25 mM, respectively, and then the cleavage reaction solution was passed twice over a preequilibrated Ni-NTA Sepharose slurry (200 ml of bed volume, equilibrated with a buffer solution (300 mM NaCl, 25 mM imidazole, and 0.5 mM TCEP buffered with 25 mM Tris-HCl, pH 7.4), in a Poly-Prep Chromatography Column (Bio-Rad: 731-1550). The flow-through was collected and concentrated with a Pierce Protein Concentrator (30 kDa MWCO, PES-membrane, Thermo Scientific: 88502) to ~150 µl. The concentrated solutions were dialyzed using micro-dialyzer units (10 kDa MWCO, Slide-A-Lyzer MINI, Thermo Scientific: 69576) against buffer B (150 mM NaCl and 0.5 mM TCEP buffered with 25 mM Tris-HCl, pH 7.4) at 4ºC overnight. Finally, the concentrations of the proteins were determined using the absorbance at 280 nm, assuming molecular extinction coefficients of 6.11, 6.15, 5.30, 5.18, and 4.84 x 10^4 (M/cm) for GFP-VASP, mCherry-zyxin (WT), mCherry-zyxin (ΔPr), mCherry-zyxin (ΔIDR), and mCherry-zyxin (ΔNC), respectively (determined from the amino acid composition data [117]). The purities of GFP-VASP, mCherry-zyxin (WT), mCherry-zyxin (ΔPr), mCherry-zyxin (ΔIDR), and mCherry-zyxin (ΔNC) were 84, 72, 69, 89, and 71%, respectively, as determined by the staining of the SDS-PAGE gels with CBBR (InstantBlue Coomassie Protein Stain [ISB1L], Abcam: ab119211). Aliquots (10 µl) of the protein solutions were placed

in Eppendorf tubes, which were rapidly frozen in liquid N_2 and stored at -80ºC until use.

In vitro phase separation assay

Purified zyxin and VASP solutions were diluted with buffer B to the desired protein concentrations. After the addition of 1% PEG8K, the mixtures were transferred to glass-bottom slides (Ibidi: 81507) for imaging. All reactions and observations were performed at 37ºC.

QUANTIFICATION AND STATISTICAL ANALYSIS

Software and statistical analysis

Superimpositions of image sequences obtained in two colors and tracking single-molecules in the movies were performed using C++-based computer programs produced in-house, as described previously [45,108]. Conventional TIRF images were processed and analyzed using Fiji [118] (NIH), MatLab 2019a (MathWorks), and ilastik [58]. Curve fittings were performed using Origin 2017 (OriginLab). Statistical analyses were performed using OriginPro 2017, Rstudio, and Excel (Microsoft). $P<0.05$ was defined as statistically significant. Other image and data analyses were performed using Fiji and MatLab 2019a. Figures and videos were edited using Photoshop CC 2021 and Illustrator CC 2021 (Adobe).

SUPPLEMENTAL ITEM TITLES AND LEGENDS

Video S1. Visualizing the talin and zyxin clusters on the apical PM by rolling averaging, related to Figure 1

Type or paste caption here. Movies recorded at video rate (**top**) and those after rolling averaging over 30 frames and background subtraction (**bottom**) are replayed at video rate. Halo7-talin expressed in a talin1/2-dKO MEF, Halo7-zyxin in a zyxin-KO MEF, and Halo7-farnesyl expressed in a talin2 KO MEF were labeled with the SaraFluor650-conjugated Halo-ligand and observed on the apical PM. After rolling averaging, the signal from the fast-diffusing molecules in the cytoplasm and on the PM, like Halo7-farnesyl, became averaged out. Meanwhile, immobile and slowly diffusing molecules and molecular clusters bound to the PM were visible even after rolling averaging (marked by circles in the bottom movies). A representative movie among 20 movies.

Video S2. Transient recruitment of a CD59 cluster to an iTRVZ platform, related to Figure 1

Real-time movie of CD59 clusters formed by the anti-CD59 mAb-coated fluorescent beads (magenta, with a trajectory), superimposed on the rolling-averaged movie of iTRVZ (observed as SNAPf-talin clusters in a Talin1/2-dKO MEF; green; TMR label) observed on the apical PM (recorded at video rate). A representative movie among 20 movies.

Video S3. Transient recruitment of a PDGF molecule to an iTRVZ platform upon stimulation, related to Figure 1

Real-time movie of PDGFR (magenta, with a trajectory; SaraFluor650 label) superimposed on the rolling-averaged movie of iTRVZ (observed as SNAPf-talin clusters in a Talin1/2-dKO MEF; green; TMR label) observed on the apical PM (recorded at video rate) after PDGF stimulation. The PDGFR spot might represent a monomer or an oligomer, but due to the presence of endogenous non-labeled PDGFR molecules, we could not confirm this. A representative movie among 20 movies.

Video S4. Typical signal intensity fluctuations of a talin cluster (iTRVZ), indicating rapid exchanges of talin molecules with those in the cytoplasm, related to Figure 1

The raw movie (video rate; **top left**) and 30-frame rolling averaged movie (**top right)** of a talin cluster (iTRVZ observed as a Halo7-talin cluster in a Talin1/2-dKO MEF; labeled with SaraFluor650), and their signal intensity time traces (**bottom**). The intensity fluctuation is mostly quantized with the changes representing the entry and exit of one to a few talin molecules into/out of the iTRVZ (talin cluster) during a frame time of 30 ms. The quantized intensity fluctuations are most visible in the time trace averaged over 5 frames. This result suggests that iTRVZ is a liquid-like entity. A representative movie among 10 movies.

Video S5. Transient recruitment of a FAK molecule to an iTRVZ platform upon PDGF stimulation, related to Figure S3

Real-time movie of Halo7-FAK (magenta, with a trajectory; SaraFluor650 label) superimposed on the rolling-averaged movie of iTRVZ (observed as SNAPf-talin clusters; green; TMR label) on the apical PM of a T24-T cell, recorded at video rate, after PDGF stimulation. A representative movie among 20 movies.

Video S6. Transient recruitment of a PIP5K molecule to an iTRVZ platform even before stimulation, related to Figure 4

Real-time movie of Halo7-PIP5K (magenta, with a trajectory; SaraFluor650 label) superimposed on the rolling-averaged movie of iTRVZ (observed as SNAPf-talin clusters; green; TMR label) on the apical PM of a T24-T cell, recorded at video rate, without PDGF stimulation. A representative movie among 20 movies.

Video S7. In-cell FRAP analysis of zyxin and VASP, showing that overexpressed zyxin and VASP form micron-scale liquid-like droplets inside the cell, related to Figure 6 and S6

Both zyxin and VASP (**first and second videos from left**), zyxin alone and VASP alone (**third and fourth videos from left, respectively**) overexpressed in T24 cells were analyzed by FRAP (observed every 2 s), using mCherry-zyxin and mGFP-VASP. A representative

movie among 15 movies.

Table S1. A complete list of plasmids used in this study, related to STAR Methods.

For complete sequence data, see **Data S1**.

Data S1. A set of text files for complete sequences of plasmids used in this study, related to STAR Methods.

Files are in GenBank format with annotations.

REFERENCES

1. Taniguchi, C.M., Emanuelli, B., and Kahn, C.R. (2006). Critical nodes in signalling pathways: insights into insulin action. Nat. Rev. Mol. Cell Biol. *7*, 85–96. https://doi.org/10.1038/nrm1837.

2. Chen, Z., Oh, D., Dubey, A.K., Yao, M., Yang, B., Groves, J.T., and Sheetz, M. (2018). EGFR family and Src family kinase interactions: mechanics matters? Curr. Opin. Cell Biol. *51*, 97–102. https://doi.org/10.1016/j.ceb.2017.12.003.

3. Wakefield, D.L., Holowka, D., and Baird, B. (2017). The FcεRI signaling cascade and integrin trafficking converge at patterned ligand surfaces. Mol. Biol. Cell *28*, 3383–3396. https://doi.org/10.1091/mbc.e17-03-0208.

4. Suzuki, K.G., Fujiwara, T.K., Edidin, M., and Kusumi, A. (2007). Dynamic recruitment of phospholipase C gamma at transiently immobilized GPI-anchored receptor clusters induces IP3-Ca2+ signaling: single-molecule tracking study 2. J. Cell Biol. *177*, 731–742. https://doi.org/10.1083/jcb.200609175.

5. Suzuki, K.G., Fujiwara, T.K., Sanematsu, F., Iino, R., Edidin, M., and Kusumi, A. (2007). GPI-anchored receptor clusters transiently recruit Lyn and G alpha for temporary cluster immobilization and Lyn activation: single-molecule tracking study 1. J. Cell Biol. *177*, 717–730. https://doi.org/10.1083/jcb.200609174.

6. Cui, X., Zhang, X., Bu, H., Liu, N., Li, H., Guan, X., Yan, H., Wang, Y., Zhang, H., Ding, Y., et al. (2017). Shear stress-mediated changes in the expression of complement regulatory protein CD59 on human endothelial progenitor cells by ECM-integrinαVβ3-F-actin pathway in vitro. Biochem. Biophys. Res. Commun. *494*, 416–421. https://doi.org/10.1016/j.bbrc.2017.09.019.

7. Morris, R.J. (2018). Thy-1, a pathfinder protein for the post-genomic era. Front. Cell Dev. Biol. *6*, 173. https://doi.org/10.3389/fcell.2018.00173.

8. Strainic, M.G., Liu, J., An, F., Bailey, E., Esposito, A., Hamann, J., Heeger, P.S., and Medof, M.E. (2019). CD55 is essential for CD103^{+} dendritic cell tolerogenic responses that protect against autoimmunity. Am. J. Pathol. *189*, 1386–1401. https://doi.org/10.1016/j.ajpath.2019.04.008.

9. Kalappurakkal, J.M., Anilkumar, A.A., Patra, C., Zanten, T.S. van, Sheetz, M.P., and Mayor, S. (2019). Integrin mechano-chemical signaling generates plasma membrane nanodomains that promote cell spreading. Cell *177*, 1738-1756. e23. https://doi.org/10.1016/j.cell.2019.04.037.

10. Kanchanawong, P., Shtengel, G., Pasapera, A.M., Ramko, E.B., Davidson, M.W., Hess, H.F., and Waterman, C.M. (2010). Nanoscale architecture of integrin-based cell adhesions. Nature *468*, 580–584. https://doi.org/10.1038/nature09621.

11. Theodosiou, M., Widmaier, M., Böttcher, R.T., Rognoni, E., Veelders, M., Bharadwaj, M., Lambacher, A., Austen, K., Müller, D.J., Zent, R., et al. (2016). Kindlin-2 cooperates with talin to activate integrins and induces cell spreading by directly binding paxillin. eLife *5*, e10130. https://doi.org/10.7554/elife.10130.

12. Yamada, K.M., and Sixt, M. (2019). Mechanisms of 3D cell migration. Nat. Rev. Mol. Cell Biol. *20*, 738–752. https://doi.org/10.1038/s41580-019-0172-9.

13. Hoffman, L.M., Jensen, C.C., Kloeker, S., Wang, C.-L.A., Yoshigi, M., and Beckerle, M.C. (2006). Genetic ablation of zyxin causes Mena/VASP mislocalization, increased motility, and deficits in actin remodeling. J. Cell Biol. *172*, 771–782. https://doi.org/10.1083/jcb.200512115.

14. Fujiwara, T.K., Iwasawa, K., Kalay, Z., Tsunoyama, T.A., Watanabe, Y., Umemura, Y.M., Murakoshi, H., Suzuki, K.G.N., Nemoto, Y.L., Morone, N., et al. (2016). Confined diffusion of transmembrane proteins and lipids induced by the same actin meshwork lining the plasma membrane. Mol. Biol. Cell *27*, 1101–1119. https://doi.org/10.1091/mbc.e15-04-0186.

15. Sengupta, P., Van Engelenburg, S., and Lippincott-Schwartz, J. (2012). Visualizing cell structure and function with point-localization superresolution imaging. Dev. Cell *23*, 1092–1102. https://doi.org/10.1016/j.devcel.2012.09.022.

16. Levet, F., Hosy, E., Kechkar, A., Butler, C., Beghin, A., Choquet, D., and Sibarita, J.-B. (2015). SR-Tesseler: a method to segment and quantify localization-based super-resolution microscopy data. Nat. Methods *12*, 1065–1071. https://doi.org/10.1038/nmeth.3579.

17. Stone, M.B., and Veatch, S.L. (2014). Steady-state cross-correlations for live two-colour super-resolution localization data sets. Nat. Commun. *6*, 7347. https://doi.org/10.1038/ncomms8347.

18. Han, S.J., Azarova, E.V., Whitewood, A.J., Bachir, A., Guttierrez, E., Groisman, A., Horwitz, A.R., Goult, B.T., Dean, K.M., and Danuser, G. (2021). Pre-complexation of talin and vinculin without tension is required for efficient nascent adhesion maturation. eLife *10*, e66151. https://doi.org/10.7554/elife.66151.

19. Paolo, G.D., Pellegrini, L., Letinic, K., Cestra, G., Zoncu, R., Voronov, S., Chang, S., Guo, J., Wenk, M.R., and Camilli, P.D. (2002). Recruitment and regulation of phosphatidylinositol phosphate kinase type 1γ by the FERM domain of talin. Nature *420*, 85–89. https://doi.org/10.1038/nature01147.

20. Cho, E.-A., Zhang, P., Kumar, V., Kavalchuk, M., Zhang, H., Huang, Q., Duncan, J.S., and Wu, J. (2021). Phosphorylation of RIAM by src promotes integrin activation by unmasking the PH domain of RIAM. Structure *29*, 320-329. e4. https://doi.org/10.1016/j.str.2020.11.011.

21. Furutani, M., Tsujita, K., Itoh, T., Ijuin, T., and Takenawa, T. (2006). Application of phosphoinositide-binding domains for the detection and quantification of specific phosphoinositides. Anal. Biochem. *355*, 8–18. https://doi.org/10.1016/j.ab.2006.05.014.

22. Maekawa, M. (2017). Domain 4 (D4) of perfringolysin O to visualize cholesterol in cellular membranes—the update. Sensors *17*, 504. https://doi.org/10.3390/s17030504.

23. Endapally, S., Frias, D., Grzemska, M., Gay, A., Tomchick, D.R., and Radhakrishnan, A. (2019). Molecular discrimination between two conformations of sphingomyelin in plasma membranes. Cell *176*, 1040-1053. e17. https://doi.org/10.1016/j.cell.2018.12.042.

24. Idevall-Hagren, O., Dickson, E.J., Hille, B., Toomre, D.K., and Camilli, P.D. (2012). Optogenetic control of phosphoinositide metabolism. Proc. Natl. Acad. Sci. USA *109*, E2316–E2323. https://doi.org/10.1073/pnas.1211305109.

25. Santos, M. de S., Naal, R.M.Z.G., Baird, B., and Holowka, D. (2013). Inhibitors of PI(4,5)P_2 synthesis reveal dynamic regulation of IgE receptor signaling by phosphoinositides in RBL mast cells. Mol. Pharmacol. *83*, 793–804. https://doi.org/10.1124/mol.112.082834.

26. Gowrishankar, K., Ghosh, S., Saha, S., Rumamol, C., Mayor, S., and Rao, M. (2012). Active remodeling of cortical actin regulates spatiotemporal organization of cell surface molecules. Cell *149*, 1353–1367. https://doi.org/10.1016/j.cell.2012.05.008.

27. Lee, S., Uchida, Y., Wang, J., Matsudaira, T., Nakagawa, T., Kishimoto, T., Mukai, K., Inaba, T., Kobayashi, T., Molday, R.S., et al. (2015). Transport through recycling endosomes requires EHD1 recruitment by a phosphatidylserine translocase. EMBO J. *34*, 669–688. https://doi.org/10.15252/embj.201489703.

28. Simons, K., and Sampaio, J.L. (2011). Membrane organization and lipid rafts. Cold Spring Harb. Perspect. Biol. *3*, a004697. https://doi.org/10.1101/cshperspect.a004697.

29. Rossi, E., Casali, B., Regolisti, G., Davoli, S., Perazzoli, F., Negro, A., Sani, C., Tumiati, B., and Nicoli, D. (1998). Increased plasma levels of platelet-derived growth factor (PDGF-BB + PDGF-AB) in patients with never-treated mild essential hypertension. Am. J. Hypertens. *11*, 1239–1243. https://doi.org/10.1016/s0895-7061(98)00124-1.

30. Piovesan, D., Necci, M., Escobedo, N., Monzon, A.M., Hatos, A., Mičetić, I., Quaglia, F., Paladin, L., Ramasamy, P., Dosztányi, Z., et al. (2020). MobiDB: intrinsically disordered proteins in 2021. Nucleic Acids Res. *49*, D361–D367. https://doi.org/10.1093/nar/gkaa1058.

31. Milovanovic, D., Wu, Y., Bian, X., and Camilli, P.D. (2018). A liquid phase of synapsin and lipid vesicles. Science *361*, 604–607. https://doi.org/10.1126/science.aat5671.

32. Feng, Z., Chen, X., Wu, X., and Zhang, M. (2019). Formation of biological condensates via phase separation: Characteristics, analytical methods, and physiological implications. J. Biol. Chem. *294*, 14823–14835. https://doi.org/10.1074/jbc.rev119.007895.

33. Case, L.B., Ditlev, J.A., and Rosen, M.K. (2019). Regulation of transmembrane signaling by phase separation. Annu. Rev. Biophys. *48*, 465–494. https://doi.org/10.1146/annurev-biophys-052118-115534.

34. Jaqaman, K., and Ditlev, J.A. (2021). Biomolecular condensates in membrane receptor signaling. Curr. Opin. Cell Biol. *69*, 48–54. https://doi.org/10.1016/j.ceb.2020.12.006.

35. Hoffmann, C., Sansevrino, R., Morabito, G., Logan, C., Vabulas, R.M., Ulusoy, A., Ganzella, M., and Milovanovic, D. (2021). Synapsin condensates recruit alpha-synuclein. J. Mol. Biol. *433*, 166961. https://doi.org/10.1016/j.jmb.2021.166961.

36. Huang, W.Y.C., Alvarez, S., Kondo, Y., Lee, Y.K., Chung, J.K., Lam, H.Y.M., Biswas, K.H., Kuriyan, J., and Groves, J.T. (2019). A molecular assembly phase transition and

kinetic proofreading modulate Ras activation by SOS. Science *363*, 1098–1103. https://doi.org/10.1126/science.aau5721.

37. Klosin, A., Oltsch, F., Harmon, T., Honigmann, A., Jülicher, F., Hyman, A.A., and Zechner, C. (2020). Phase separation provides a mechanism to reduce noise in cells. Science *367*, 464–468. https://doi.org/10.1126/science.aav6691.

38. Suzuki, K.G., Kasai, R.S., Hirosawa, K.M., Nemoto, Y.L., Ishibashi, M., Miwa, Y., Fujiwara, T.K., and Kusumi, A. (2012). Transient GPI-anchored protein homodimers are units for raft organization and function. Nat. Chem. Biol. *8*, 774–783. https://doi.org/10.1038/nchembio.1028.

39. Kusumi, A., Tsunoyama, T.A., Hirosawa, K.M., Kasai, R.S., and Fujiwara, T.K. (2014). Tracking single molecules at work in living cells. Nat. Chem. Biol. *10*, 524–532. https://doi.org/10.1038/nchembio.1558.

40. Su, X., Ditlev, J.A., Hui, E., Xing, W., Banjade, S., Okrut, J., King, D.S., Taunton, J., Rosen, M.K., and Vale, R.D. (2016). Phase separation of signaling molecules promotes T cell receptor signal transduction. Science *352*, 595–599. https://doi.org/10.1126/science.aad9964.

41. Peng, S., Li, W., Yao, Y., Xing, W., Li, P., and Chen, C. (2020). Phase separation at the nanoscale quantified by dcFCCS. Proc. Natl Acad. Sci. USA *117*, 27124–27131. https://doi.org/10.1073/pnas.2008447117.

42. Rouches, M., Veatch, S.L., and Machta, B.B. (2021). Surface densities prewet a near-critical membrane. Proc. Natl. Acad. Sci. USA *118*, e2103401118. https://doi.org/10.1073/pnas.2103401118.

43. Lin, C.-C., Suen, K.M., Jeffrey, P.-A., Wieteska, L., Lidster, J.A., Bao, P., Curd, A.P., Stainthorp, A., Seiler, C., Koss, H., et al. (2022). Receptor tyrosine kinases regulate signal transduction through a liquid-liquid phase separated state. Mol. Cell *82*, 1089-1106. e12. https://doi.org/10.1016/j.molcel.2022.02.005.

44. Massou, S., Vicente, F.N., Wetzel, F., Mehidi, A., Strehle, D., Leduc, C., Voituriez, R., Rossier, O., Nassoy, P., and Giannone, G. (2020). Cell stretching is amplified by active actin remodelling to deform and recruit proteins in mechanosensitive structures. Nat. Cell Biol. *22*, 1011–1023. https://doi.org/10.1038/s41556-020-0548-2.

45. Fujiwara, T., Ritchie, K., Murakoshi, H., Jacobson, K., and Kusumi, A. (2002). Phospholipids undergo hop diffusion in compartmentalized cell membrane. J. Cell Biol. *157*, 1071–1082. https://doi.org/10.1083/jcb.200202050.

46. Koyama-Honda, I., Fujiwara, T.K., Kasai, R.S., Suzuki, K.G.N., Kajikawa, E., Tsuboi, H., Tsunoyama, T.A., and Kusumi, A. (2020). High-speed single-molecule imaging reveals signal transduction by induced transbilayer raft phases. J. Cell Biol. *219*, e202006125. https://doi.org/10.1083/jcb.202006125.

47. Liu, S., Calderwood, D.A., and Ginsberg, M.H. (2000). Integrin cytoplasmic domain-binding proteins. J. Cell Sci. *113*, 3563–3571.

48. Lamsoul, I., Dupré, L., and Lutz, P.G. (2020). Molecular tuning of filamin A activities in the context of adhesion and migration. Front. Cell Dev. Biol. *8*, 591323. https://doi.org/10.3389/fcell.2020.591323.

49. Calderwood, D.A., Campbell, I.D., and Critchley, D.R. (2013). Talins and kindlins: partners in integrin-mediated adhesion. Nat. Rev. Mol. Cell Biol. *14*, 503–517. https://doi.org/10.1038/nrm3624.

50. Sulzmaier, F.J., Jean, C., and Schlaepfer, D.D. (2014). FAK in cancer: mechanistic findings and clinical applications. Nat. Rev. Cancer *14*, 598–610. https://doi.org/10.1038/nrc3792.

51. Takenawa, T., and Suetsugu, S. (2007). The WASP–WAVE protein network: connecting the membrane to the cytoskeleton. Nat. Rev. Mol. Cell Biol. *8*, 37–48. https://doi.org/10.1038/nrm2069.

52. López-Colomé, A.M., Lee-Rivera, I., Benavides-Hidalgo, R., and López, E. (2017). Paxillin: a crossroad in pathological cell migration. J. Hematol. Oncol. *10*, 50. https://doi.org/10.1186/s13045-017-0418-y.

53. Yang, J., Zhu, L., Zhang, H., Hirbawi, J., Fukuda, K., Dwivedi, P., Liu, J., Byzova, T., Plow, E.F., Wu, J., et al. (2014). Conformational activation of talin by RIAM triggers integrin-mediated cell adhesion. Nat Commun. *5*, 5880. https://doi.org/10.1038/ncomms6880.

54. Bays, J.L., and DeMali, K.A. (2017). Vinculin in cell–cell and cell–matrix adhesions. Cell Mol. Life Sci. *74*, 2999–3009. https://doi.org/10.1007/s00018-017-2511-3.

55. Sjöblom, B., Salmazo, A., and Djinović-Carugo, K. (2008). α-Actinin structure and regulation. Cell Mol. Life Sci. *65*, 2688. https://doi.org/10.1007/s00018-008-8080-8.

56. Krause, M., Dent, E.W., Bear, J.E., Loureiro, J.J., and Gertler, F.B. (2003). ENA/VASP proteins: regulators of the actin cytoskeleton and cell migration. Cell Dev. Biol. *19*, 541–564. https://doi.org/10.1146/annurev.cellbio.19.050103.103356.

57. Kotb, A., Hyndman, M.E., and Patel, T.R. (2018). The role of zyxin in regulation of malignancies. Heliyon *4*, e00695. https://doi.org/10.1016/j.heliyon.2018.e00695.

58. Berg, S., Kutra, D., Kroeger, T., Straehle, C.N., Kausler, B.X., Haubold, C., Schiegg, M., Ales, J., Beier, T., Rudy, M., et al. (2019). ilastik: interactive machine learning for (bio)image analysis. Nat. Methods *16*, 1226–1232. https://doi.org/10.1038/s41592-019-0582-9.

59. Praekelt, U., Kopp, P.M., Rehm, K., Linder, S., Bate, N., Patel, B., Debrand, E., Manso, A.M., Ross, R.S., Conti, F., et al. (2012). New isoform-specific monoclonal antibodies reveal different sub-cellular localisations for talin1 and talin2. Eur. J. Cell Biol. *91*, 180–191. https://doi.org/10.1016/j.ejcb.2011.12.003.

60. Ovesný, M., Křížek, P., Borkovec, J., Švindrych, Z., and Hagen, G.M. (2014). ThunderSTORM: a comprehensive ImageJ plug-in for PALM and STORM data analysis and super-resolution imaging. Bioinformatics *30*, 2389–2390. https://doi.org/10.1093/bioinformatics/btu202.

61. Zitter, E.D., Thédié, D., Mönkemöller, V., Hugelier, S., Beaudouin, J., Adam, V., Byrdin, M., Meervelt, L.V., Dedecker, P., and Bourgeois, D. (2019). Mechanistic investigation of mEos4b reveals a strategy to reduce track interruptions in sptPALM. Nat. Methods *16*, 707–710. https://doi.org/10.1038/s41592-019-0462-3.

62. Curtis, I. de (2021). Biomolecular condensates at the front: cell migration meets phase separation. Trends Cell Biol. *31*, 145–148. https://doi.org/10.1016/j.tcb.2020.12.002.

63. Case, L.B., Pasquale, M.D., Henry, L., and Rosen, M.K. (2022). Synergistic phase separation of two pathways promotes integrin clustering and nascent adhesion formation. eLife *11*, e72588. https://doi.org/10.7554/elife.72588.

64. Li, Y., Zhang, T., Li, H., Yang, H., Lin, R., Sun, K., Wang, L., Zhang, J., Wei, Z., and Yu, C. (2020). Kindlin2-mediated phase separation underlies integrin adhesion formation. BioRxiv, 2020.07.10.197400. https://doi.org/10.1101/2020.07.10.197400.

65. Graham, K., Chandrasekaran, A., Wang, L., Ladak, A., Lafer, E.M., Rangamani, P., and Stachowiak, J.C. (2022). Liquid-like assembly of VASP drives actin polymerization and bundling. Biorxiv, 2022.05.09.491236. https://doi.org/10.1101/2022.05.09.491236.

66. Wang, Y., Zhang, C., Yang, W., Shao, S., Xu, X., Sun, Y., Li, P., Liang, L., and Wu, C. (2021). LIMD1 phase separation contributes to cellular mechanics and durotaxis by regulating focal adhesion dynamics in response to force. Dev. Cell *56*, 1313-1325.e7. https://doi.org/10.1016/j.devcel.2021.04.002.

67. Zhu, J., Zhou, Q., Xia, Y., Lin, L., Li, J., Peng, M., Zhang, R., and Zhang, M. (2020). GIT/PIX condensates are modular and ideal for distinct compartmentalized cell signaling. Mol. Cell *79*, 782-796.e6. https://doi.org/10.1016/j.molcel.2020.07.004.

68. Case, L.B., Zhang, X., Ditlev, J.A., and Rosen, M.K. (2019). Stoichiometry controls activity of phase-separated clusters of actin signaling proteins. Science *363*, 1093–1097. https://doi.org/10.1126/science.aau6313.

69. Sala, K., Corbetta, A., Minici, C., Tonoli, D., Murray, D.H., Cammarota, E., Ribolla, L., Ramella, M., Fesce, R., Mazza, D., et al. (2019). The ERC1 scaffold protein implicated in cell motility drives the assembly of a liquid phase. Sci. Rep. *9*, 13530. https://doi.org/10.1038/s41598-019-49630-y.

70. Sala, K., Raimondi, A., Tonoli, D., Tacchetti, C., and Curtis, I. de (2018). Identification of a membrane-less compartment regulating invadosome function and motility. Sci. Rep. *8*, 1164. https://doi.org/10.1038/s41598-018-19447-2.

71. Korkmazhan, E., Tompa, P., and Dunn, A.R. (2021). The role of ordered cooperative assembly in biomolecular condensates. Nat. Rev. Mol. Cell Biol. *22*, 647–648. https://doi.org/10.1038/s41580-021-00408-z.

72. Amri, M.E., Fitzgerald, U., and Schlosser, G. (2018). MARCKS and MARCKS-like proteins in development and regeneration. J. Biomed. Sci. *25*, 43. https://doi.org/10.1186/s12929-018-0445-1.

73. Morone, N., Fujiwara, T., Murase, K., Kasai, R.S., Ike, H., Yuasa, S., Usukura, J., and Kusumi, A. (2006). Three-dimensional reconstruction of the membrane skeleton at the plasma membrane interface by electron tomography. J. Cell Biol. *174*, 851–862. https://doi.org/10.1083/jcb.200606007.

74. Murase, K., Fujiwara, T., Umemura, Y., Suzuki, K., Iino, R., Yamashita, H., Saito, M., Murakoshi, H., Ritchie, K., and Kusumi, A. (2004). Ultrafine membrane compartments for molecular diffusion as revealed by single molecule techniques. Biophys. J. *86*, 4075–4093. https://doi.org/10.1529/biophysj.103.035717.

75. Shirai, Y.M., Tsunoyama, T.A., Hiramoto-Yamaki, N., Hirosawa, K.M., Shibata, A.C.E., Kondo, K., Tsurumune, A., Ishidate, F., Kusumi, A., and Fujiwara, T.K. (2017). Cortical actin nodes: their dynamics and recruitment of podosomal proteins as revealed by super-resolution and single-molecule microscopy. PLoS One *12*, e0188778. https://doi.org/10.1371/journal.pone.0188778.

76. Raghupathy, R., Anilkumar, A.A., Polley, A., Singh, P.P., Yadav, M., Johnson, C., Suryawanshi, S., Saikam, V., Sawant, S.D., Panda, A., et al. (2015). Transbilayer lipid interactions mediate nanoclustering of lipid-anchored proteins. Cell *161*, 581–594. https://doi.org/10.1016/j.cell.2015.03.048.

77. Naruse, K., Sai, X., Yokoyama, N., and Sokabe, M. (1998). Uni-axial cyclic stretch induces c-src activation and translocation in human endothelial cells via SA channel activation. FEBS Lett. *441*, 111–115.

78. Ihara, M., Tomimoto, H., Kitayama, H., Morioka, Y., Akiguchi, I., Shibasaki, H., Noda, M., and Kinoshita, M. (2003). Association of the cytoskeletal GTP-binding protein Sept4/H5 with cytoplasmic inclusions found in Parkinson's disease and other synucleinopathies. J. Biol. Chem. *278*, 24095–24102. https://doi.org/10.1074/jbc.m301352200.

79. Hooper, M., Hardy, K., Handyside, A., Hunter, S., and Monk, M. (1987). HPRT-deficient (Lesch–Nyhan) mouse embryos derived from germline colonization by cultured cells. Nature *326*, 292–295. https://doi.org/10.1038/326292a0.

80. Xia, S., Lim, Y.B., Zhang, Z., Wang, Y., Zhang, S., Lim, C.T., Yim, E.K.F., and Kanchanawong, P. (2019). Nanoscale architecture of the cortical actin cytoskeleton in embryonic stem cells. Cell Rep. *28*, 1251-1267.e7. https://doi.org/10.1016/j.celrep.2019.06.089.

81. Štefanová, I., Hilgert, I., Krištofová, H., Brown, R., Low, M.G., and Hořejši, V. (1989). Characterization of a broadly expressed human leucocyte surface antigen MEM-43 anchored in membrane through phosphatidylinositol. Mol. Immunol. *26*, 153–161. https://doi.org/10.1016/0161-5890(89)90097-7.

82. Madore, N., Smith, K.L., Graham, C.H., Jen, A., Brady, K., Hall, S., and Morris, R. (1999). Functionally different GPI proteins are organized in different domains on the neuronal surface. EMBO J. *18*, 6917–6926. https://doi.org/10.1093/emboj/18.24.6917.

83. Mason, D.W., and Williams, A.F. (1980). The kinetics of antibody binding to membrane antigens in solution and at the cell surface. Biochem. J. *187*, 1–20. https://doi.org/10.1042/bj1870001.

84. Hanke, J.H., Gardner, J.P., Dow, R.L., Changelian, P.S., Brissette, W.H., Weringer, E.J., Pollok, B.A., and Connelly, P.A. (1996). Discovery of a novel, potent, and Src family-selective tyrosine kinase inhibitor. J. Biol. Chem. *271*, 695–701. https://doi.org/10.1074/jbc.271.2.695.

85. Slack-Davis, J.K., Martin, K.H., Tilghman, R.W., Iwanicki, M., Ung, E.J., Autry, C., Luzzio, M.J., Cooper, B., Kath, J.C., Roberts, W.G., et al. (2007). Cellular characterization of a novel focal adhesion kinase inhibitor. J. Biol. Chem. *282*, 14845–14852. https://doi.org/10.1074/jbc.m606695200.

86. Kosenko, A., and Hoshi, N. (2013). A change in configuration of the calmodulin-KCNQ channel complex underlies Ca^{2+}-dependent modulation of KCNQ channel activity. PLoS One *8*, e82290. https://doi.org/10.1371/journal.pone.0082290.

87. Johnson, K.A., Budicini, M.R., Urata, S., Bhattarai, N., Gerstman, B.S., Chapagain, P.P., Li, S., and Stahelin, R.V. (2018). PI(4,5)P_2 binding sites in the Ebola virus matrix protein modulate assembly and budding. BioRxiv, 341248. https://doi.org/10.1101/341248.

88. Ulianov, S.V., Velichko, A.K., Magnitov, M.D., Luzhin, A.V., Golov, A.K., Ovsyannikova, N., Kireev, I.I., Gavrikov, A.S., Mishin, A.S., Garaev, A.K., et al. (2021). Suppression of liquid–liquid phase separation by 1,6-hexanediol partially compromises the 3D genome organization in living cells. Nucleic Acids Res. *49*, 10524–10541. https://doi.org/10.1093/nar/gkab249.

89. McKinney, S.A., Murphy, C.S., Hazelwood, K.L., Davidson, M.W., and Looger, L.L. (2009). A bright and photostable photoconvertible fluorescent protein. Nat. Methods *6*, 131–133. https://doi.org/10.1038/nmeth.1296.

90. Fujiwara, T.K., Takeuchi, S., Kalay, Z., Nagai, Y., Tsunoyama, T.A., Kalkbrenner, T., Iwasawa, K., Ritchie, K.P., Suzuki, K.G.N., and Kusumi, A. (2021). Development of ultrafast camera-based imaging of single fluorescent molecules and live-cell PALM. BioRxiv, 2021.10.26.465864. https://doi.org/10.1101/2021.10.26.465864.

91. Fujiwara, T.K., Takeuchi, S., Kalay, Z., Nagai, Y., Tsunoyama, T.A., Kalkbrenner, T., Chen, L.H., Shibata, A.C.E., Iwasawa, K., Ritchie, K.P., et al. (2021). Focal adhesion membrane is dotted with protein islands and partitioned for molecular hop diffusion. BioRxiv, 2021.10.26.465868. https://doi.org/10.1101/2021.10.26.465868.

92. Bindels, D.S., Haarbosch, L., Weeren, L. van, Postma, M., Wiese, K.E., Mastop, M., Aumonier, S., Gotthard, G., Royant, A., Hink, M.A., et al. (2017). mScarlet: a bright monomeric red fluorescent protein for cellular imaging. Nat. Methods *14*, 53–56. https://doi.org/10.1038/nmeth.4074.

93. Maekawa, M., and Fairn, G.D. (2015). Complementary probes reveal that phosphatidylserine is required for the proper transbilayer distribution of cholesterol. J. Cell Sci. *128*, 1422–1433. https://doi.org/10.1242/jcs.164715.

94. Johnson, B.B., Moe, P.C., Wang, D., Rossi, K., Trigatti, B.L., and Heuck, A.P. (2012). Modifications in perfringolysin O domain 4 alter the cholesterol concentration threshold required for binding. Biochemistry *51*, 3373–3382. https://doi.org/10.1021/bi3003132.

95. Ilić, D., Almeida, E.A.C., Schlaepfer, D.D., Dazin, P., Aizawa, S., and Damsky, C.H. (1998). Extracellular matrix survival signals transduced by focal adhesion kinase suppress p53-mediated apoptosis. J. Cell Biol. *143*, 547–560. https://doi.org/10.1083/jcb.143.2.547.

96. Lee, H.-S., Anekal, P., Lim, C.J., Liu, C.-C., and Ginsberg, M.H. (2013). Two modes of integrin activation form a binary molecular switch in adhesion maturation. Mol. Biol. Cell *24*, 1354–1362. https://doi.org/10.1091/mbc.e12-09-0695.

97. Tsuruta, D., Gonzales, M., Hopkinson, S.B., Otey, C., Khuon, S., Goldman, R.D., and Jones, J.C.R. (2002). Microfilament-dependent movement of the β3 integrin subunit within focal contacts of endothelial cells. FASEB J. *16*, 866–868. https://doi.org/10.1096/fj.01-0878fje.

98. Okrut, J., Prakash, S., Wu, Q., Kelly, M.J.S., and Taunton, J. (2015). Allosteric N-WASP activation by an inter-SH3 domain linker in Nck. Proc. Natl Acad. Sci. USA *112*, E6436–E6445. https://doi.org/10.1073/pnas.1510876112.

99. Sun, Y., Thapa, N., Hedman, A.C., and Anderson, R.A. (2013). Phosphatidylinositol 4,5-bisphosphate: targeted production and signaling. Bioessays *35*, 513–522. https://doi.org/10.1002/bies.201200171.

100. Uchida, Y., Hasegawa, J., Chinnapen, D., Inoue, T., Okazaki, S., Kato, R., Wakatsuki, S., Misaki, R., Koike, M., Uchiyama, Y., et al. (2011). Intracellular phosphatidylserine is essential for retrograde membrane traffic through endosomes. Proc. Natl. Acad. Sci. USA *108*, 15846–15851. https://doi.org/10.1073/pnas.1109101108.

101. Diamond, L.E., McCurry, K.R., Oldham, E.R., Tone, M., Waldmann, H., Platt, J.L., and Logan, J.S. (1995). Human CD59 expressed in transgenic mouse hearts inhibits the activation of complement. Transpl. Immunol. *3*, 305–312. https://doi.org/10.1016/0966-3274(95)80016-6.

102. Johannessen, C.M., Boehm, J.S., Kim, S.Y., Thomas, S.R., Wardwell, L., Johnson, L.A., Emery, C.M., Stransky, N., Cogdill, A.P., Barretina, J., et al. (2010). COT drives resistance to RAF inhibition through MAP kinase pathway reactivation. Nature *468*, 968–972. https://doi.org/10.1038/nature09627.

103. Jones, N.P., Peak, J., Brader, S., Eccles, S.A., and Katan, M. (2005). PLCγ1 is essential for early events in integrin signalling required for cell motility. J. Cell Sci. *118*, 2695–2706. https://doi.org/10.1242/jcs.02374.

104. Ishida, S., Matsu-ura, T., Fukami, K., Michikawa, T., and Mikoshiba, K. (2014). Phospholipase C-β1 and β4 contribute to non-genetic cell-to-cell variability in histamine-induced calcium signals in HeLa cells. PLoS One *9*, e86410. https://doi.org/10.1371/journal.pone.0086410.

105. Sasaki, A., Taketomi, T., Kato, R., Saeki, K., Nonami, A., Sasaki, M., Kuriyama, M., Saito, N., Shibuya, M., and Yoshimura, A. (2003). Mammalian Sprouty4 suppresses Ras-independent ERK activation by binding to Raf1. Nat. Cell Biol. *5*, 427–432. https://doi.org/10.1038/ncb978.

106. Lindberg, F.P., Gresham, H.D., Schwarz, E., and Brown, E.J. (1993). Molecular cloning of integrin-associated protein: an immunoglobulin family member with multiple

membrane-spanning domains implicated in alpha v beta 3-dependent ligand binding. J. Cell Biol. *123*, 485–496. https://doi.org/10.1083/jcb.123.2.485.

107. Nakamura, A., Oki, C., Kato, K., Fujinuma, S., Maryu, G., Kuwata, K., Yoshii, T., Matsuda, M., Aoki, K., and Tsukiji, S. (2020). Engineering orthogonal, plasma membrane-specific SLIPT systems for multiplexed chemical control of signaling pathways in living single cells. ACS Chem. Biol. *15*, 1004–1015. https://doi.org/10.1021/acschembio.0c00024.

108. Koyama-Honda, I., Ritchie, K., Fujiwara, T., Iino, R., Murakoshi, H., Kasai, R.S., and Kusumi, A. (2005). Fluorescence imaging for monitoring the colocalization of two single molecules in living cells. Biophys. J. *88*, 2126–2136. https://doi.org/10.1529/biophysj.104.048967.

109. Shibata, A.C., Fujiwara, T.K., Chen, L., Suzuki, K.G., Ishikawa, Y., Nemoto, Y.L., Miwa, Y., Kalay, Z., Chadda, R., Naruse, K., et al. (2012). Archipelago architecture of the focal adhesion: membrane molecules freely enter and exit from the focal adhesion zone. Cytoskeleton *69*, 380–392. https://doi.org/10.1002/cm.21032.

110. Tsunoyama, T.A., Watanabe, Y., Goto, J., Naito, K., Kasai, R.S., Suzuki, K.G.N., Fujiwara, T.K., and Kusumi, A. (2018). Super-long single-molecule tracking reveals dynamic-anchorage-induced integrin function. Nat. Chem. Biol. *14*, 497–506. https://doi.org/10.1038/s41589-018-0032-5.

111. Sahl, S.J., Leutenegger, M., Hilbert, M., Hell, S.W., and Eggeling, C. (2010). Fast molecular tracking maps nanoscale dynamics of plasma membrane lipids. Proc. Natl Acad. Sci. USA *107*, 6829–6834. https://doi.org/10.1073/pnas.0912894107.

112. Veatch, S.L., Machta, B.B., Shelby, S.A., Chiang, E.N., Holowka, D.A., and Baird, B.A. (2012). Correlation functions quantify super-resolution images and estimate apparent clustering due to over-counting. PLoS One *7*, e31457. https://doi.org/10.1371/journal.pone.0031457.

113. Xu, K., Zhong, G., and Zhuang, X. (2013). Actin, spectrin, and associated proteins form a periodic cytoskeletal structure in axons. Science *339*, 452–456. https://doi.org/10.1126/science.1232251.

114. Lee, S.-H., Shin, J.Y., Lee, A., and Bustamante, C. (2012). Counting single photoactivatable fluorescent molecules by photoactivated localization microscopy (PALM). Proc. Natl Acad. Sci. USA *109*, 17436–17441. https://doi.org/10.1073/pnas.1215175109.

115. Dundr, M., and Misteli, T. (2003). Measuring dynamics of nuclear proteins by photobleaching. Curr. Protoc. Cell Biol. *18*, 13.5.1-13.5.18. https://doi.org/10.1002/0471143030.cb1305s18.

116. Otsu, N. (1979). A threshold selection method from gray-level histograms. IEEE Trans. Syst. Man Cybern. *9*, 62–66. https://doi.org/10.1109/tsmc.1979.4310076.

117. Anthis, N.J., and Clore, G.M. (2013). Sequence-specific determination of protein and peptide concentrations by absorbance at 205 nm: sequence-specific protein concentration at 205 nm. Protein Sci. *22*, 851–858. https://doi.org/10.1002/pro.2253.

118. Schindelin, J., Arganda-Carreras, I., Frise, E., Kaynig, V., Longair, M., Pietzsch, T., Preibisch, S., Rueden, C., Saalfeld, S., Schmid, B., et al. (2012). Fiji: an open-source platform for biological-image analysis. Nat. Methods *9*, 676–682. https://doi.org/10.1038/nmeth.2019.

Figure 1

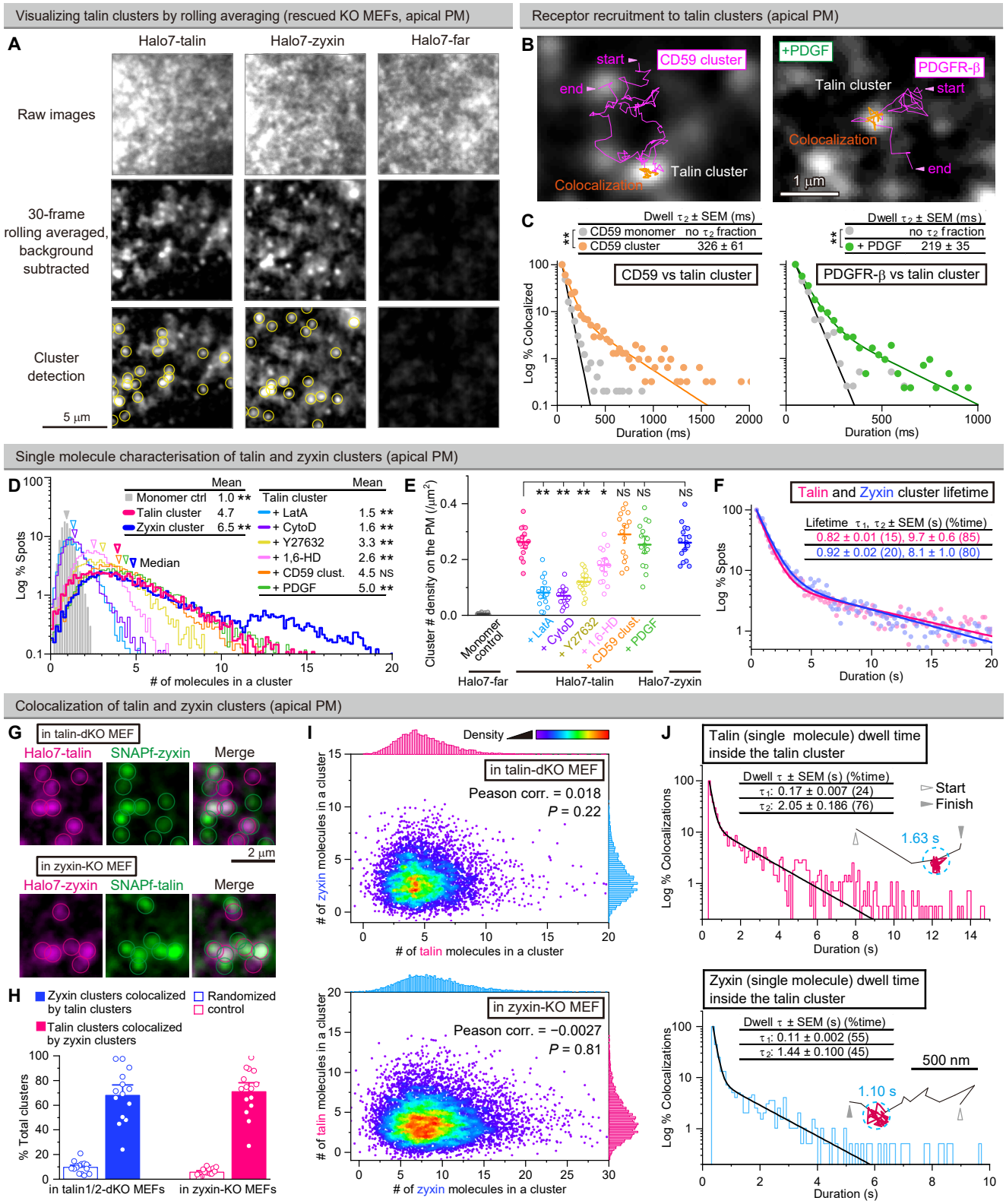
Visualizing talin clusters by rolling averaging (rescued KO MEFs, apical PM)
A
Halo7-talin
Halo7-zyxin
Halo7-far
Raw images
30-frame rolling averaged, background subtracted
Cluster detection
5 µm
Receptor recruitment to talin clusters (apical PM)
B
start
end
CD59 cluster
Talin cluster
Colocalization
+PDGF
PDGFR-β
1 µm
C
Dwell τ2 ± SEM (ms)
CD59 monomer no τ2 fraction
CD59 cluster 326 ± 61
CD59 vs talin cluster
+ PDGF 219 ± 35
PDGFR-β vs talin cluster
Log % Colocalized
Duration (ms)
Single molecule characterisation of talin and zyxin clusters (apical PM)
D
Mean
Monomer ctrl 1.0 **
Talin cluster 4.7
Zyxin cluster 6.5 **
Talin cluster
+ LatA 1.5 **
+ CytoD 1.6 **
+ Y27632 3.3 **
+ 1,6-HD 2.6 **
+ CD59 clust. 4.5 NS
+ PDGF 5.0 **
Median
Log % Spots
# of molecules in a cluster
E
Cluster # density on the PM (/µm²)
Monomer control
+ LatA
+ CytoD
+ Y27632
+ 1,6-HD
+ CD59 clust.
+ PDGF
Halo7-far
Halo7-talin
Halo7-zyxin
F
Talin and Zyxin cluster lifetime
Lifetime τ1, τ2 ± SEM (s) (%time)
0.82 ± 0.01 (15), 9.7 ± 0.6 (85)
0.92 ± 0.02 (20), 8.1 ± 1.0 (80)
Log % Spots
Duration (s)
Colocalization of talin and zyxin clusters (apical PM)
G
in talin-dKO MEF
Halo7-talin
SNAPf-zyxin
Merge
2 µm
in zyxin-KO MEF
Halo7-zyxin
SNAPf-talin
Merge
H
Zyxin clusters colocalized by talin clusters
Randomized control
Talin clusters colocalized by zyxin clusters
% Total clusters
in talin1/2-dKO MEFs
in zyxin-KO MEFs
I
Density
in talin-dKO MEF
Peason corr. = 0.018
P = 0.22
# of zyxin molecules in a cluster
# of talin molecules in a cluster
in zyxin-KO MEF
Peason corr. = −0.0027
P = 0.81
# of talin molecules in a cluster
# of zyxin molecules in a cluster
J
Talin (single molecule) dwell time inside the talin cluster
Dwell τ ± SEM (s) (%time)
τ1: 0.17 ± 0.007 (24)
τ2: 2.05 ± 0.186 (76)
Start
Finish
1.63 s
Log % Colocalizations
Duration (s)
Zyxin (single molecule) dwell time inside the talin cluster
Dwell τ ± SEM (s) (%time)
τ1: 0.11 ± 0.002 (55)
τ2: 1.44 ± 0.100 (45)
500 nm
1.10 s
Log % Colocalizations
Duration (s)

Figure 2

Conventional and PALM super-resolution images (KO MEFs rescued with mEos3.2-fused proteins)

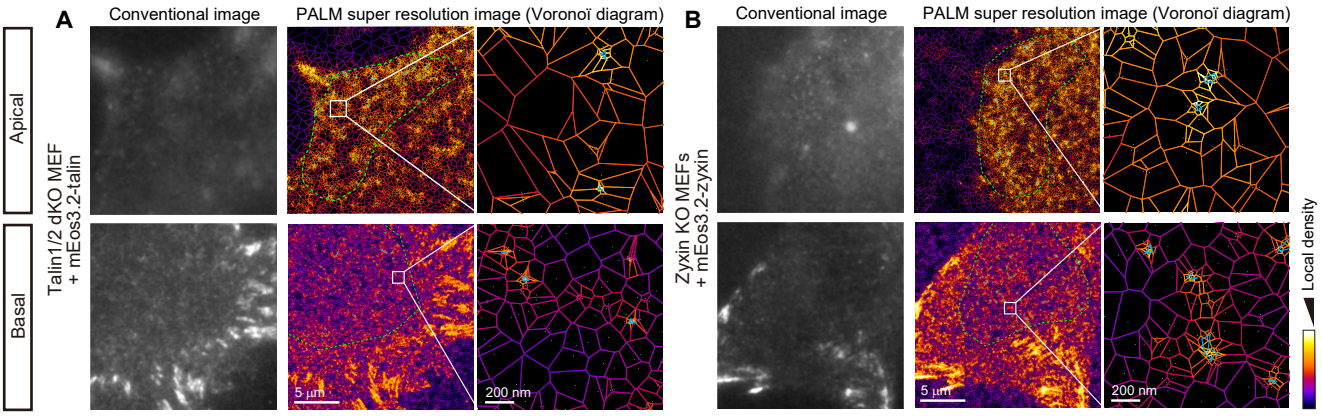

PALM quantification of talin and zyxin clusters

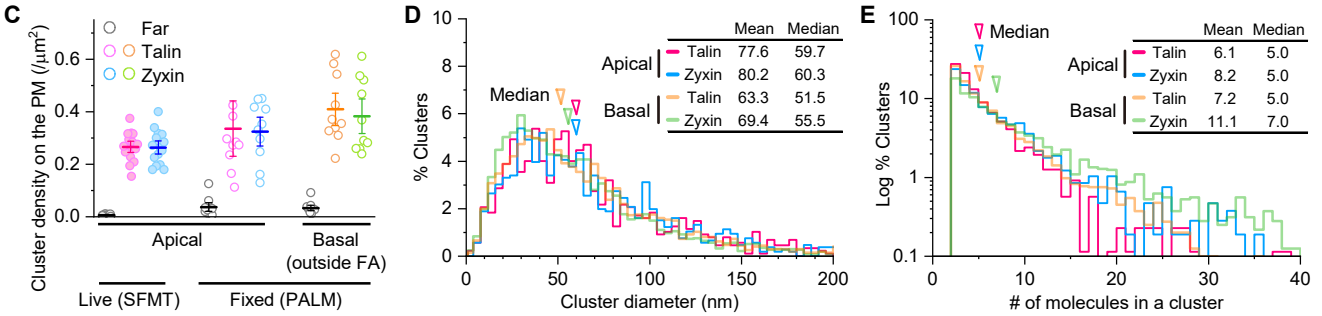

Figure 3

FA- and actin-related proteins and their interactions

Method to calculate the colocalization index

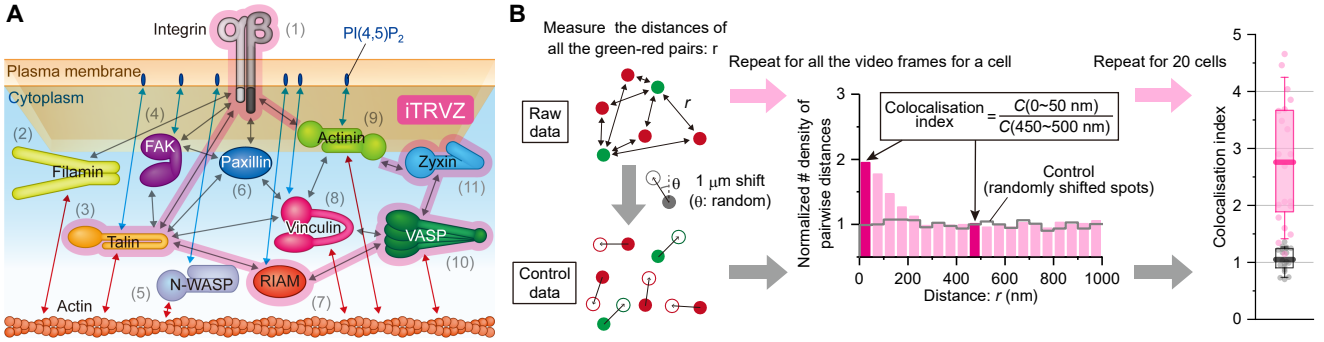

β3 integrin, talin, RIAM, VASP, zyxin form clusters, called iTRVZ (T24 cells, apical PM)

Signaling molecules are recruited to iTRVZ

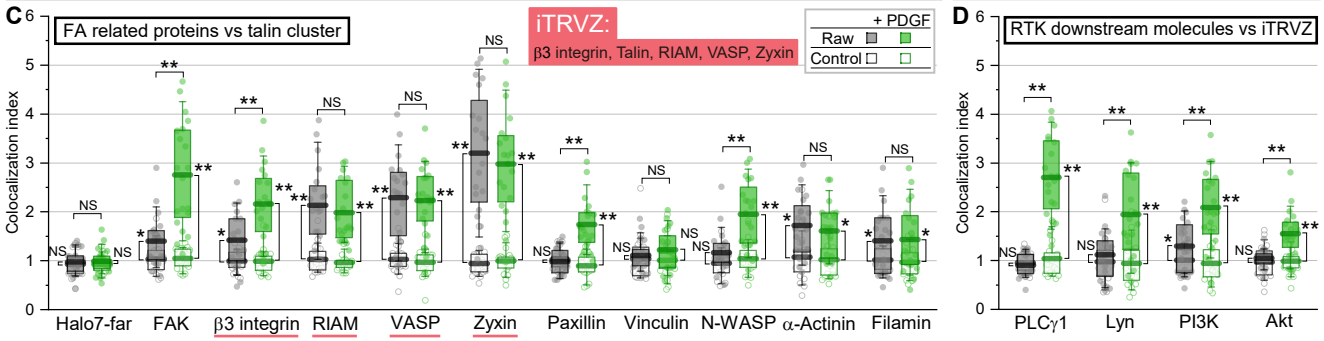

Recruitment of PLCγ1 and PLCβ1 to the iTRVZ after various stimulations (T24 cells, apical PM)

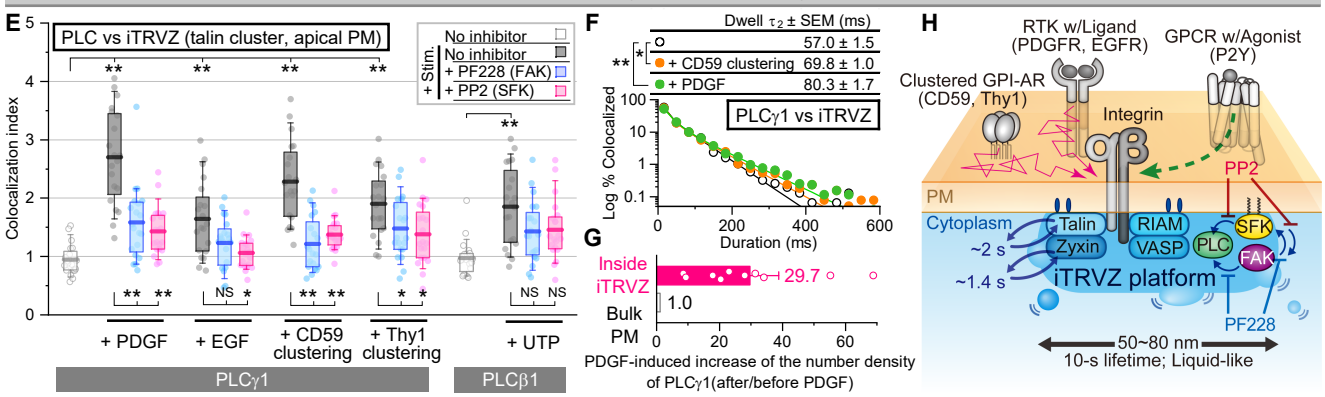

Figure 4

Colocalization of PI kinases, probes for phosphoPIs, PS, and raft domains (cholesterol and sphingomyelins) with iTRVZ (T24-T cells, apical PM)

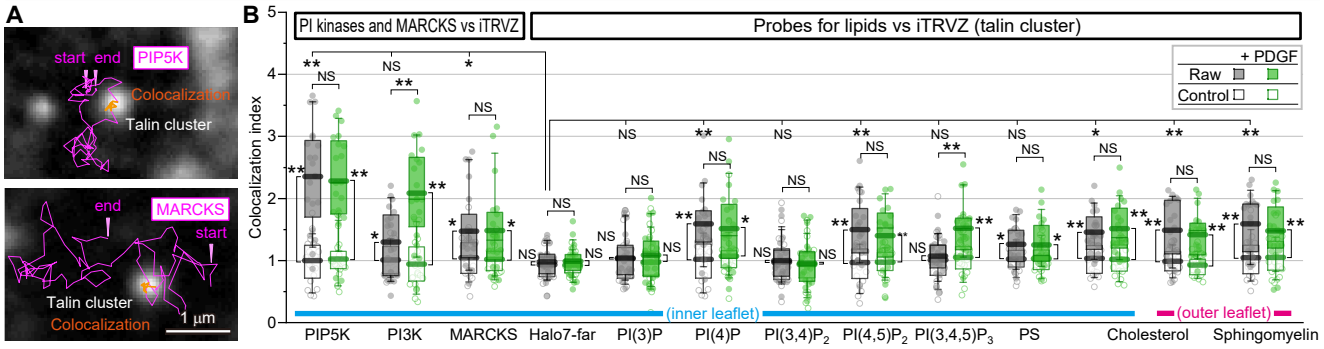

Optogenetic reduction of $PI(4,5)P_2$ on the iTRVZ (talin-rescued dKO MEFs, apical PM)

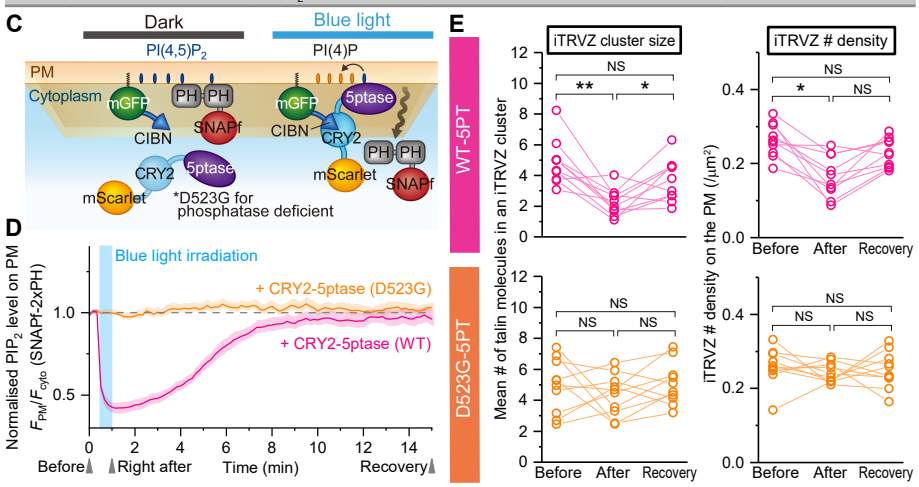

Reagent-indeced lipid depletion

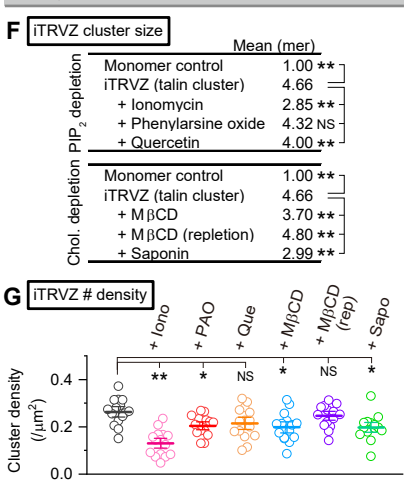

iTRVZ as a signal platform for multiple signaling pathways

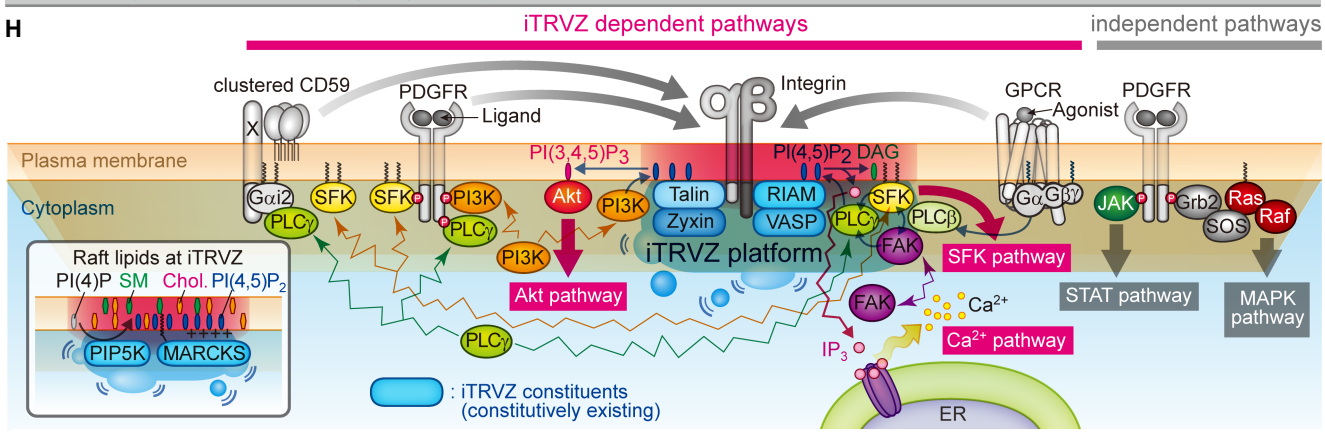

Figure 5

Cooperative integration of CD59 and PDGFR signals detected with PLCγ1 recruitment (Zyxin-KO MEFs + mGFP-zyxin [WT, −, ΔPr, ΔNC])

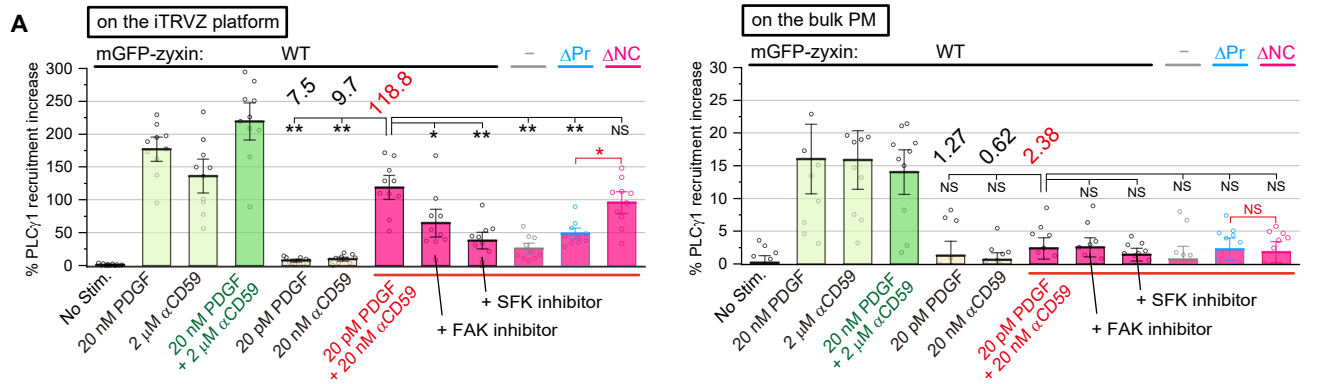

Cooperative integration of CD59 and PDGFR signals detected with Ca^{2+} responses (Zyxin-KO MEFs + mGFP-zyxin [WT, −, ΔPr, ΔNC])

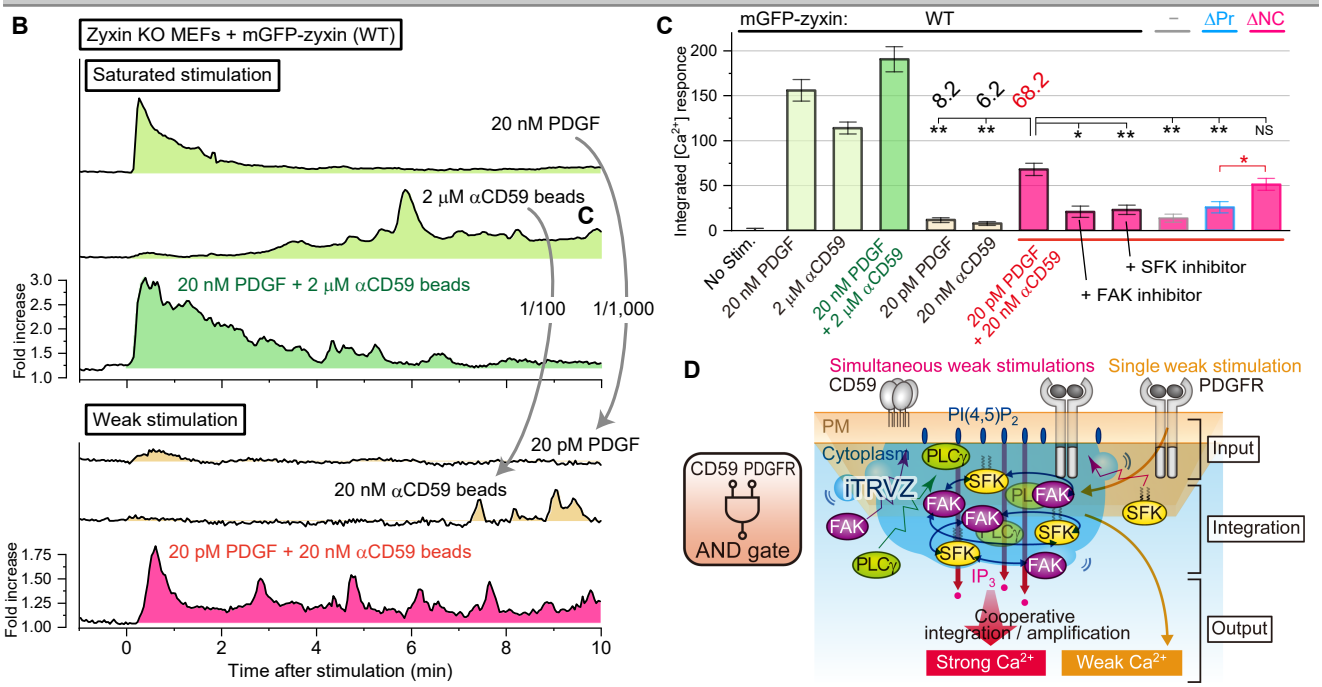

Recruitment of downstream signalling molecules after separate/simultaneous weak stimulations (zyxin-rescued KO MEF, apical PM)

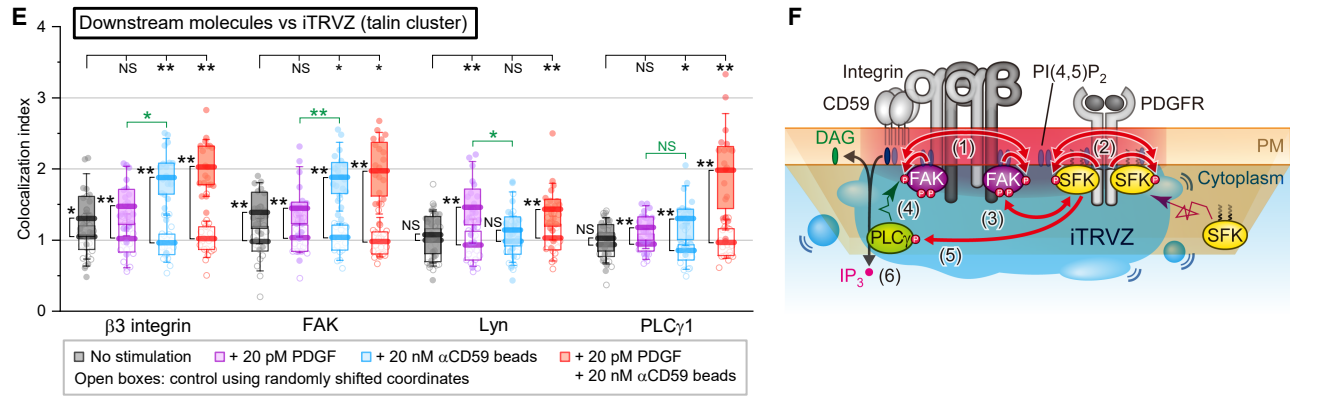

Figure 6

[*In-vitro*] LLPS assay of zyxin and VASP mixture

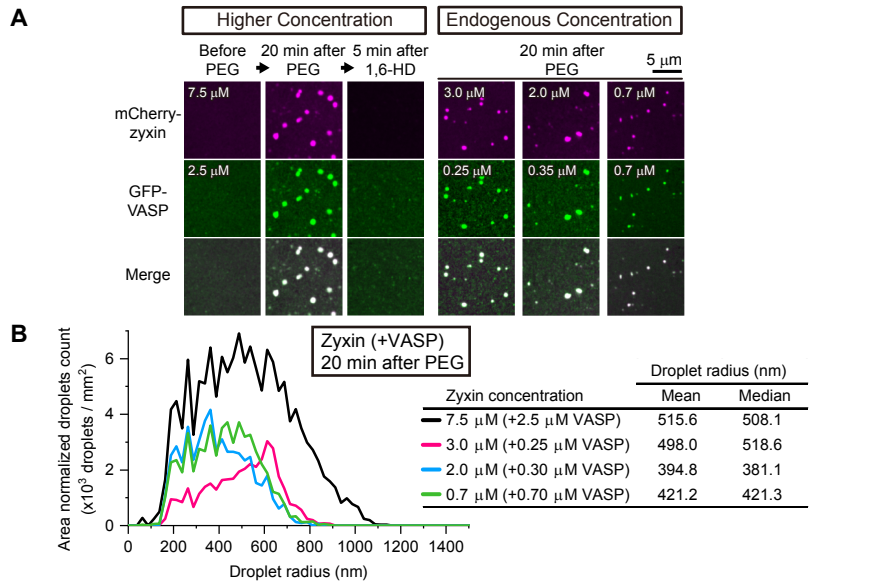

[*In-vitro*] LLPS assay of zyxin

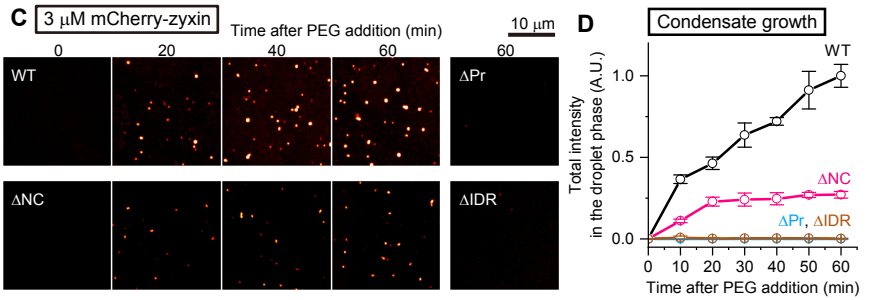

[*In-vitro* and *In-cell*] FRAP for zyxin and VASP co-condensates

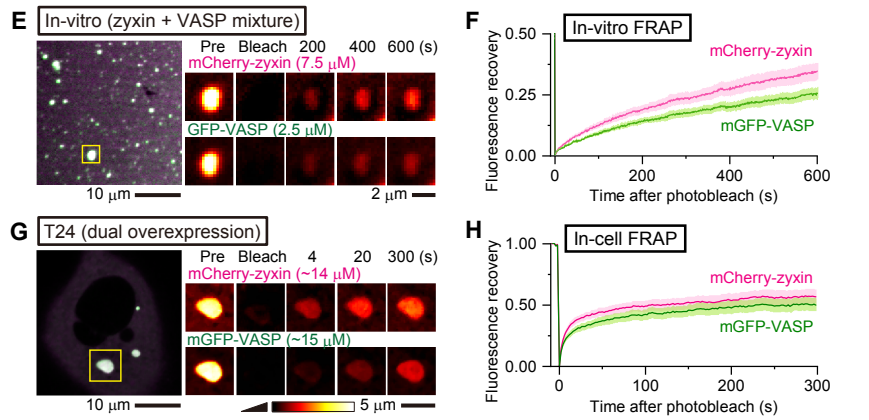

[*In-cell*] liquid behaviours of iTRVZ (zyxin rescued KO MEFs, apical PM)

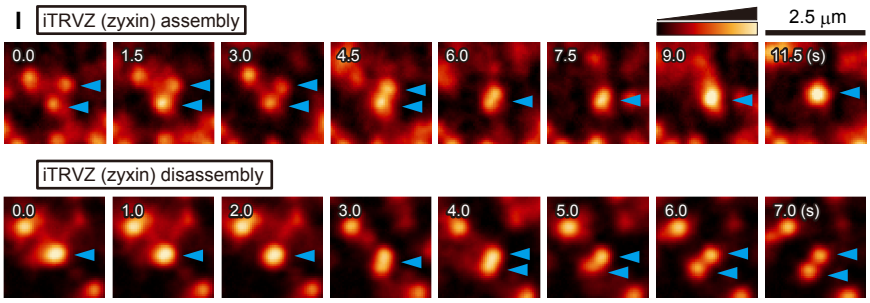

Figure 7

IDR of zyxin, VASP, RAIM and its mutants

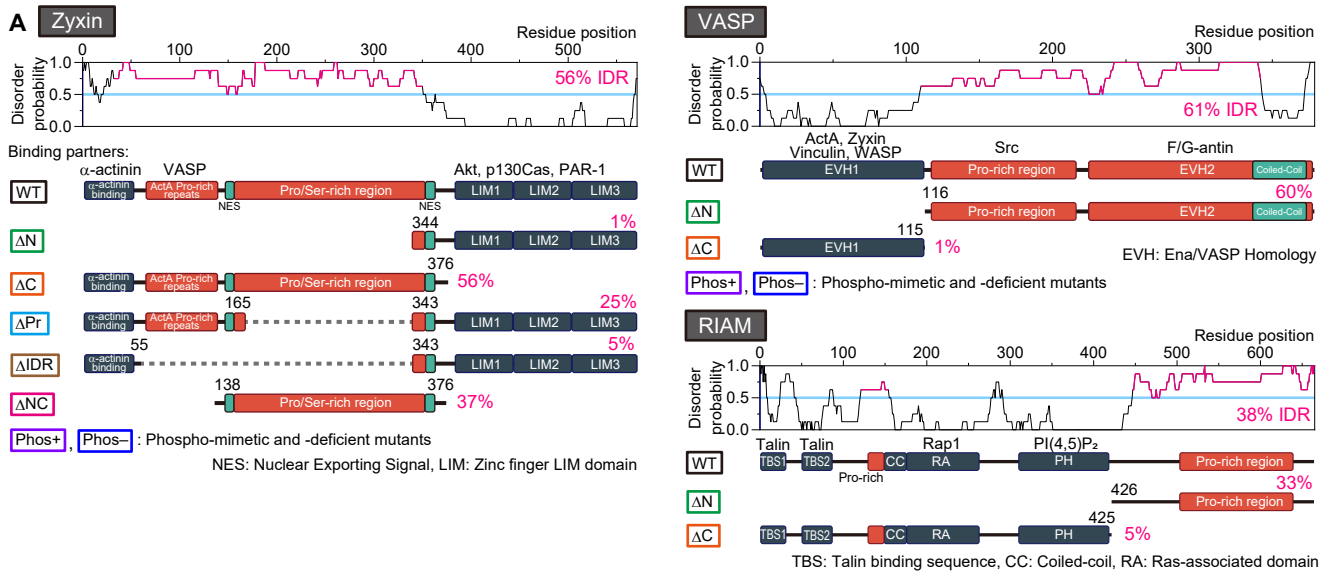

Colocalization between iTRVZ (talin cluster) and mutants (T24-T)

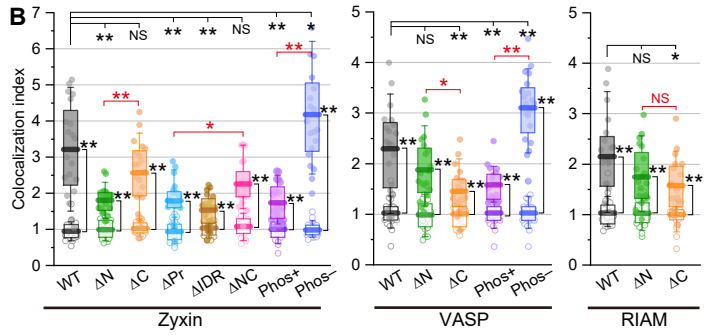

Zyxin cluster size with mutants (zyxin rescued KO MEF)

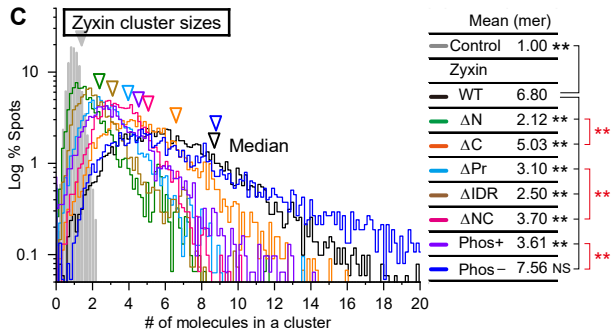

Zyxin's N-terminal domain + IDR enhances Ca^{2+} response and Akt phosphorylation (Zyxin-KO MEFs + mGFP-zyxin mutants)

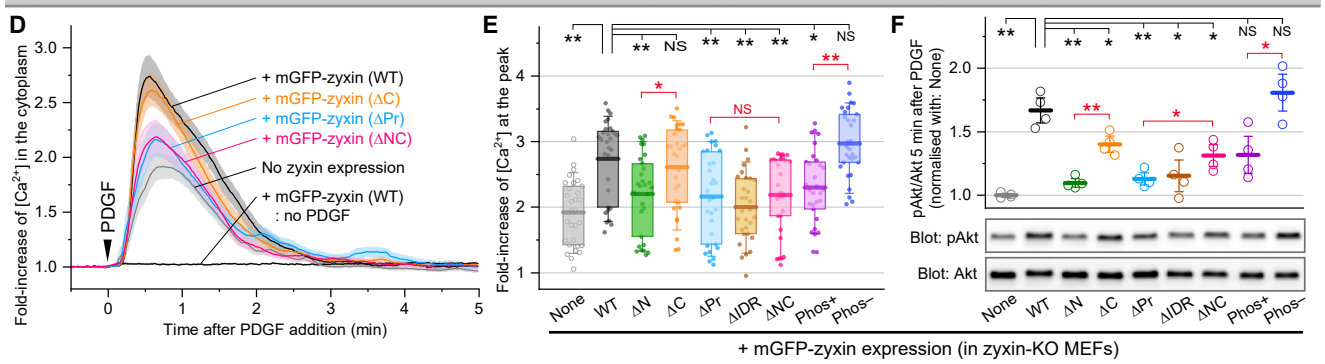

Figure S1

Rescuing talin1/2-double-KO MEF lines with tagged talins

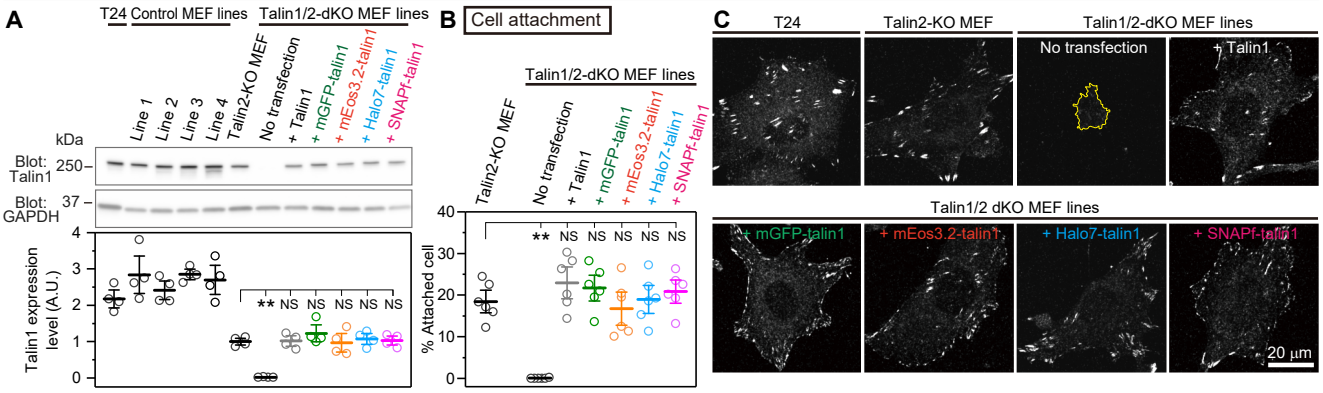

Rescuing zyxin-KO MEF lines with tagged zyxins

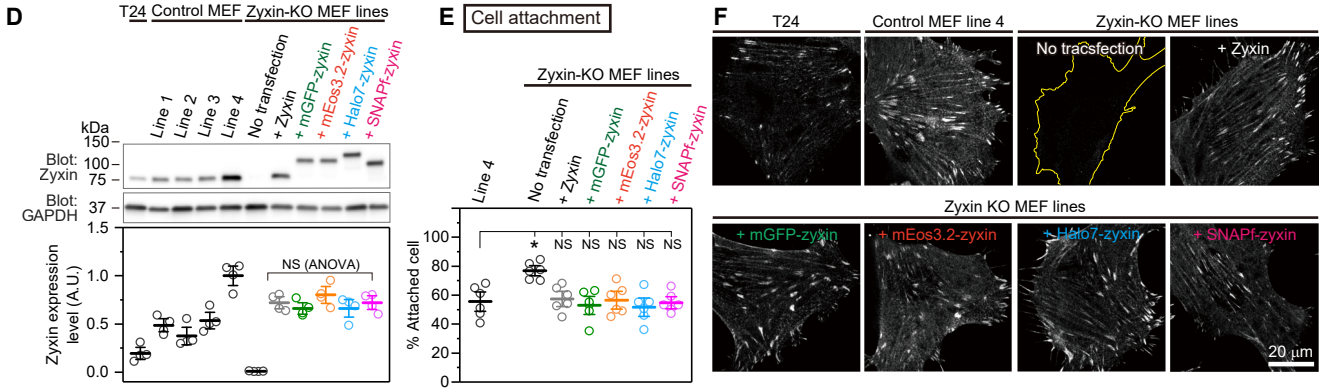

Cluster lifetime in KO MEFs (apical PM)

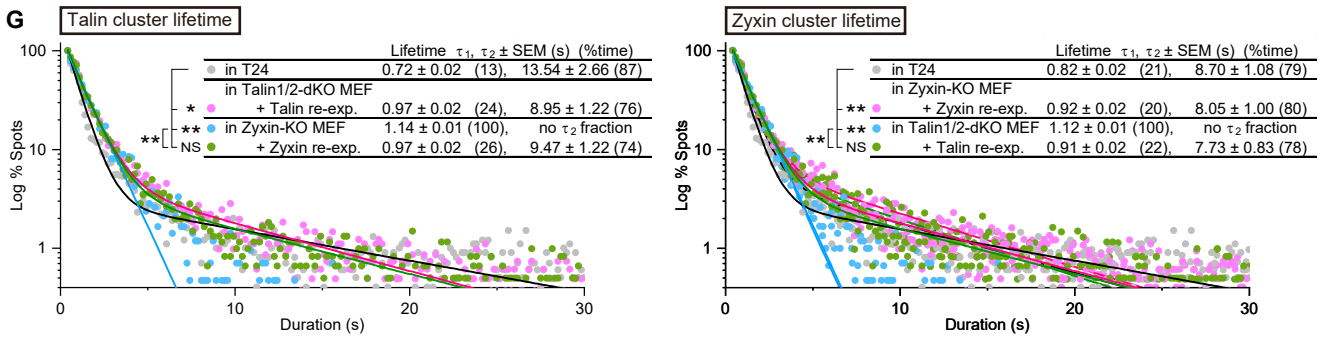

Figure S2

Photophysical properties of mEos3.2

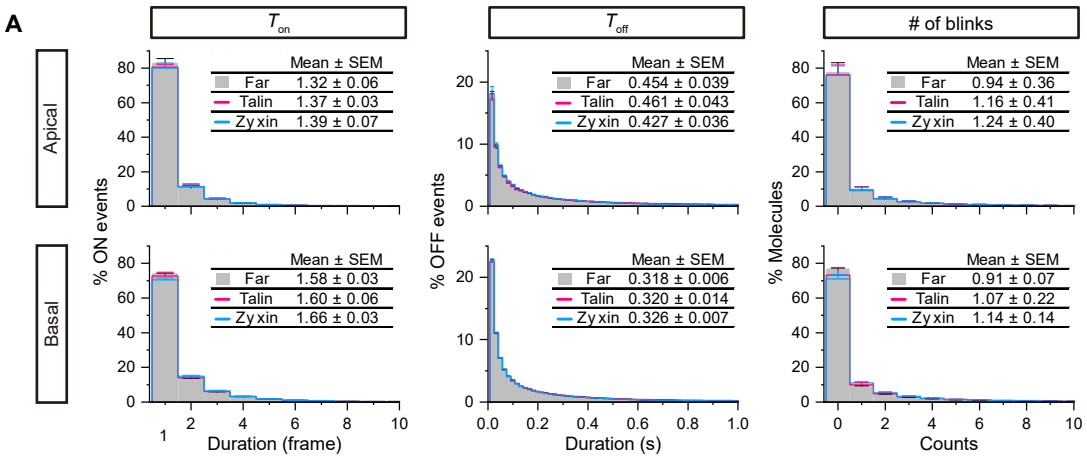

Conventional and PALM super-resolution images (control molecule: mEos3.2-far)

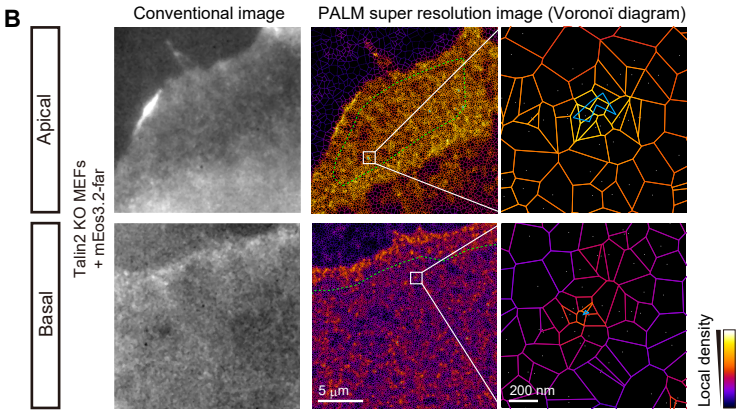

PALM quantification of control molecule (mEos3.2-far)

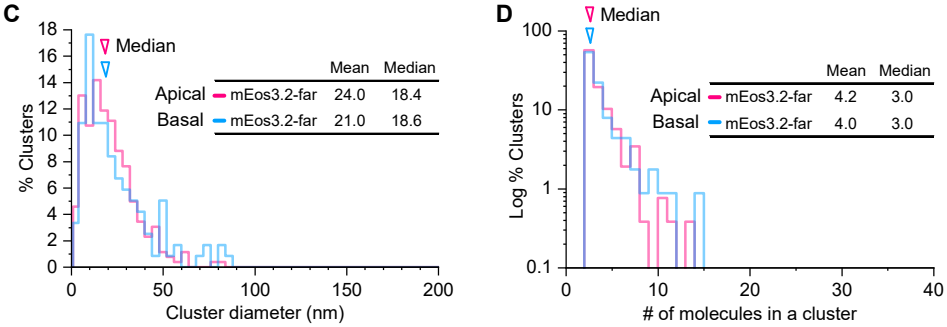

Figure S3

Halo7-talin clusters are found in all the cell lines examined here (apical PM)

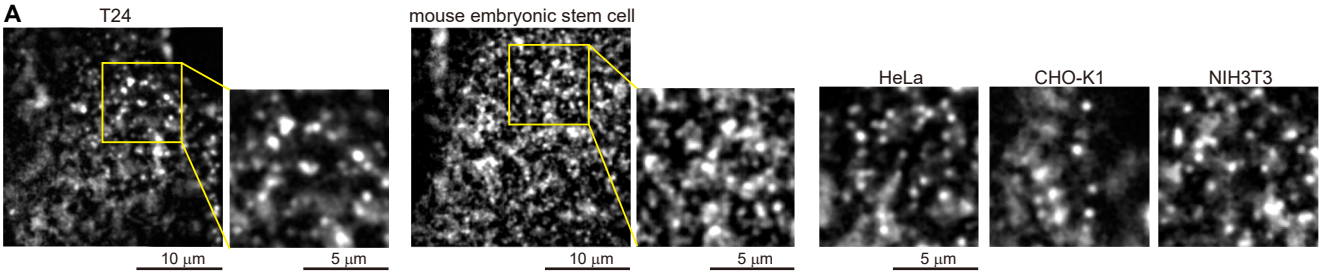

Generation of the T24-T cell line

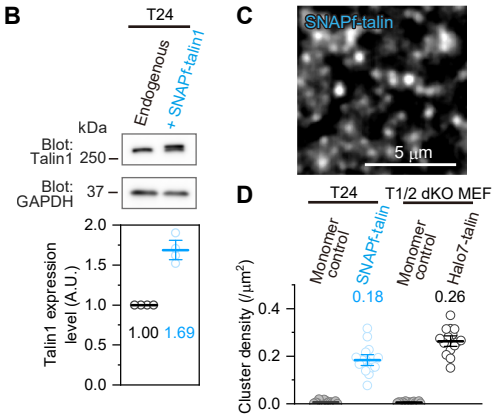

In T24-T cells, like in MEFs, receptors are recruited to the talin-zyxin clusters (apical PM)

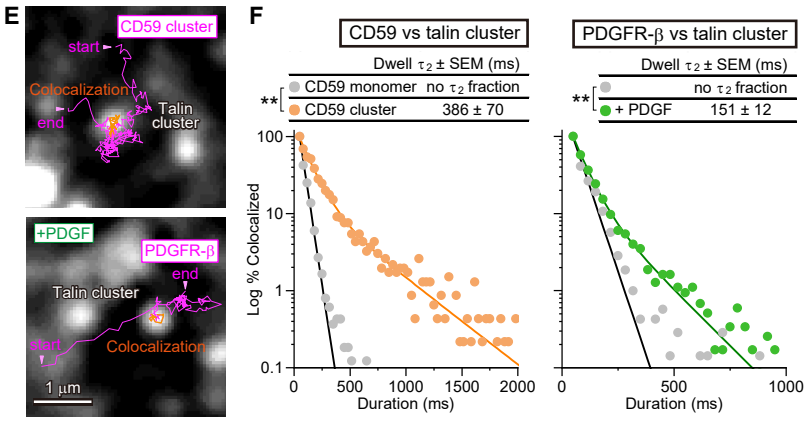

FAK recruitment after PDGF stimulation (T24-T, apical PM)

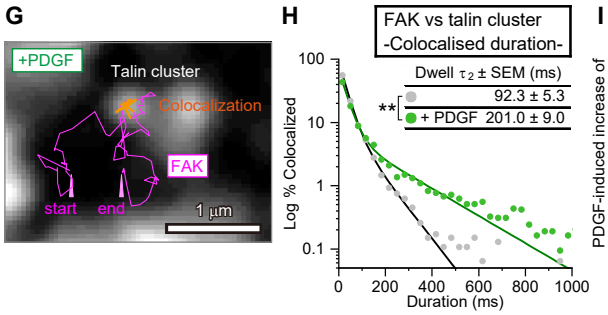

PLCγ1 recruitment after PDGF (T24-T, apical PM)

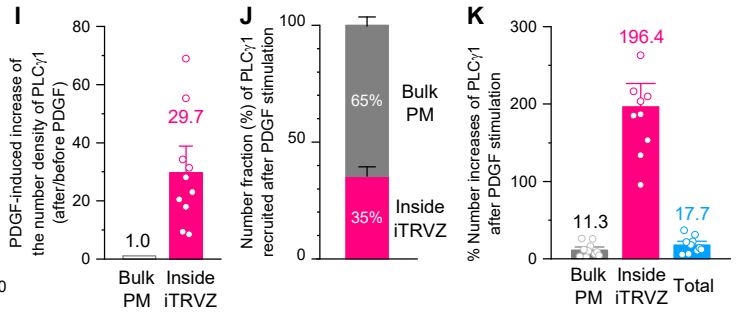

Figure S4

Effects of the optogenetic reduction of PI(4,5)P_2

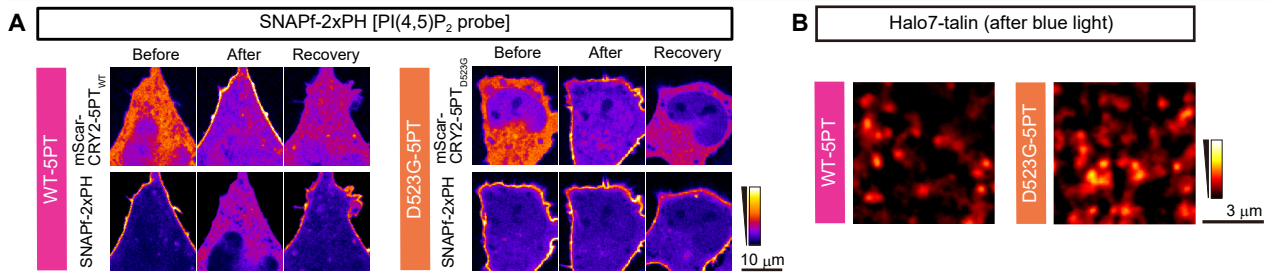

Effects of the drug-induced reduction of PI(4,5)P_2 on the iTRVZ cluster size and number density (talin-rescued dKO MEFs, apical PM)

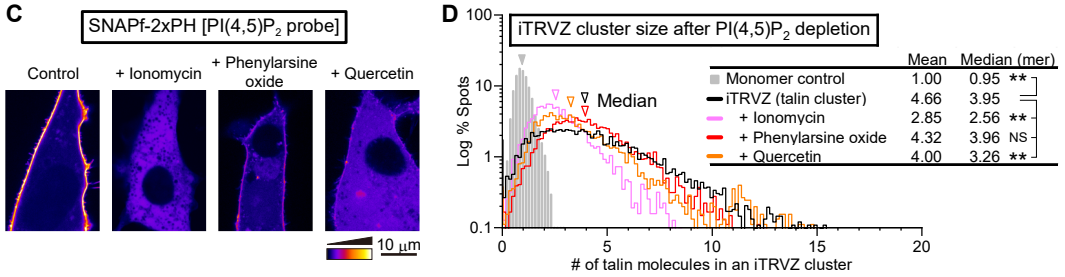

Effects of the partial cholesterol depletion on the iTRVZ cluster size and number density (talin-rescued dKO MEFs, apical PM)

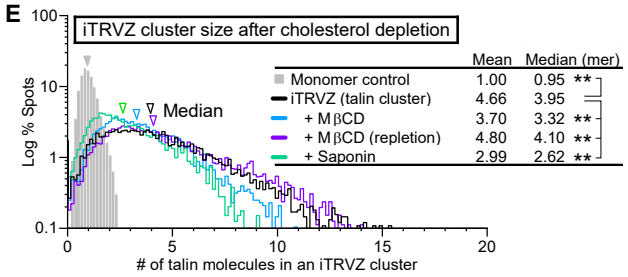

Figure S5

A

	Uniprot ID	Total (a.a.)	IDR (a.a.)	% IDR	LLPS Ref#
Receptors					
PDGFR-β	P09619	1,106	88	8.0	-
EGFR	P00533	1,210	41	3.4	-
CD59	P13987	128	0	0.0	-
Thy1	P04216	161	0	0.0	-
P2Y1	P47900	373	0	0.0	-
iTRVZ					
β3 integrin	P05106	788	0	0.0	1
Talin1	Q9Y490	2,540	0	0.0	2
RIAM	Q7Z5R6	666	253	38.0	-
VASP	P50552	380	233	61.3	3
Zyxin	Q15942	572	322	56.3	4
FA related					
Paxillin	P49023	591	269	45.5	1, 5
N-WASP	O00401	505	219	43.4	1, 6
FAK	Q05397	1,052	162	15.4	1
Filamin-A	P21333	2,647	95	3.6	-
Vinculin	P18206	1,134	31	2.7	-
α-Actinin	P12814	892	0	0.0	-
PtdIns related					
MARCKS	P29966	332	332	100.0	-
PIP5KIγ	O60331	668	126	18.9	-
PIK3CA	P42336	1,068	0	0.0	-
RTK downstream					
Raf1	P04049	648	115	17.7	-
Lyn	P07948	512	62	12.1	-
Akt	P31749	480	57	11.9	-
PLCγ1	P19174	1,290	43	3.3	7
JAK1	P23458	1,154	0	0.0	-
K-Ras	P01116	189	0	0.0	-
Other FA related proteins (not examined in this repor					
p130Cas	P56945	870	220	25.3	1
Nck1	P16333	377	0	0.0	1, 6
Kindlin2	Q96AC1	680	25	3.7	1, 2
β1 integrin	P05556	798	33	4.1	1, 2
ILK	Q13418	452	0	0.0	2
GIT1	Q9Y2X7	761	126	17.0	5, 8
β-pix	Q14155	803	129	16.1	5
LIMD1	Q9UGP4	676	261	38.6	4
Liprin-α1	Q13136	1,202	321	26.7	8, 9
ERC1	Q8IUD2	1,116	97	8.7	8, 9
LL5α	Q86UU1	1,377	487	35.4	8, 9

B

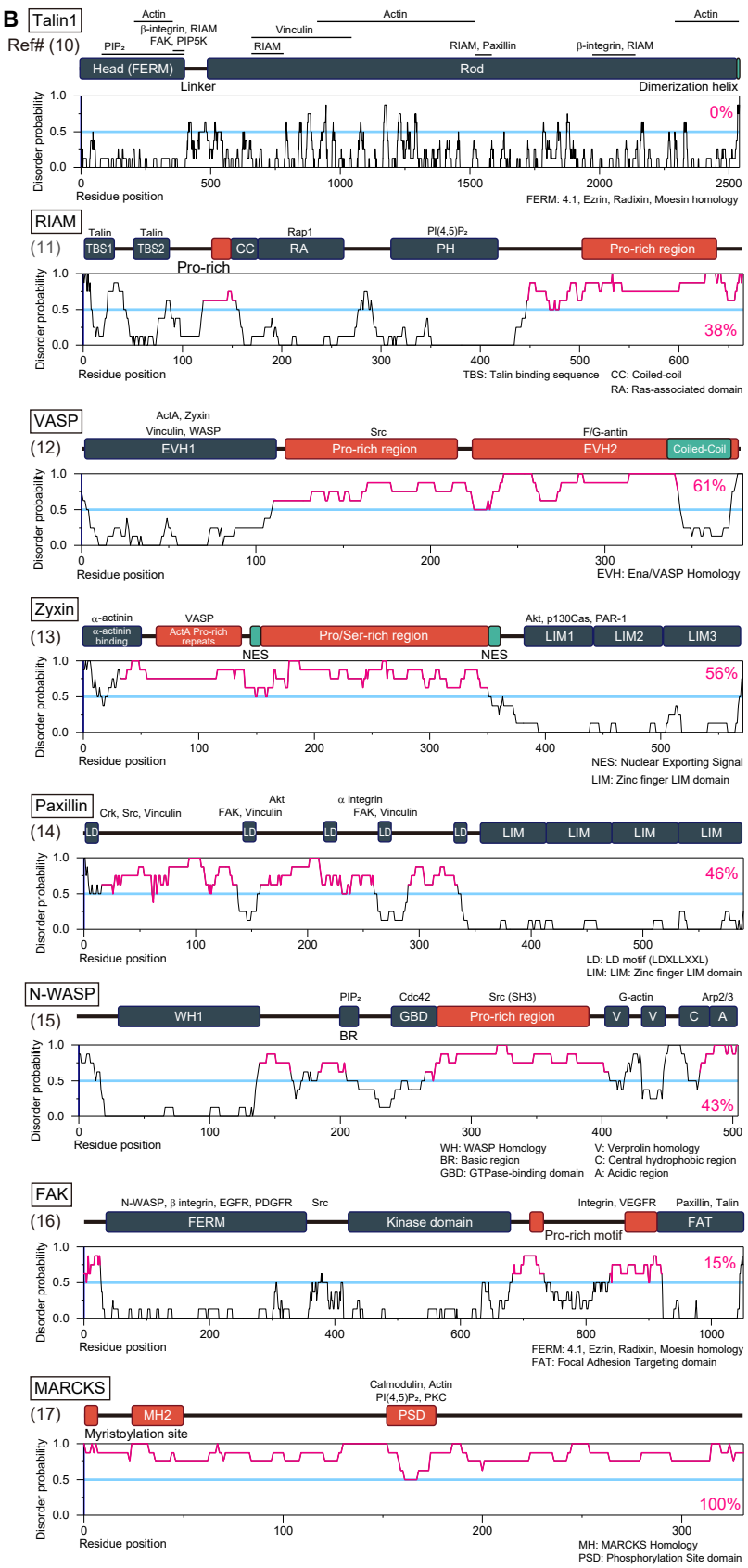

Figure S6

Determining the cytoplasmic concentrations of endogenous as well as tagged zyxin and VASP

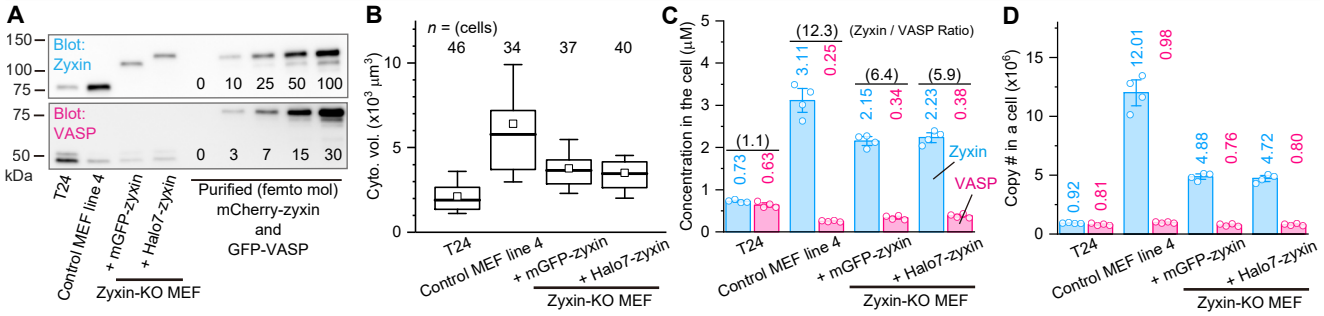

[*In-vitro*] LLPS assay of zyxin and VASP mixture

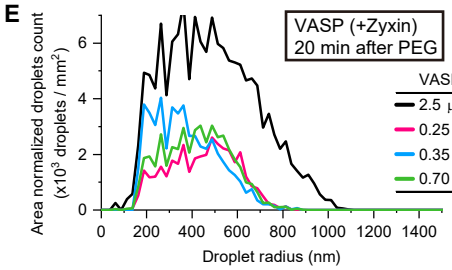

VASP concentration	Droplet radius (nm) Mean	Droplet radius (nm) Median
2.5 μM (+7.5 μM Zyxin)	484.9	469.6
0.25 μM (+3.0 μM Zyxin)	444.8	452.1
0.35 μM (+2.0 μM Zyxin)	371.2	351.7
0.70 μM (+0.70 μM Zyxin)	430.2	433.9

[*In-vitro* and *In-cell*] FRAP for zyxin and VASP condensates

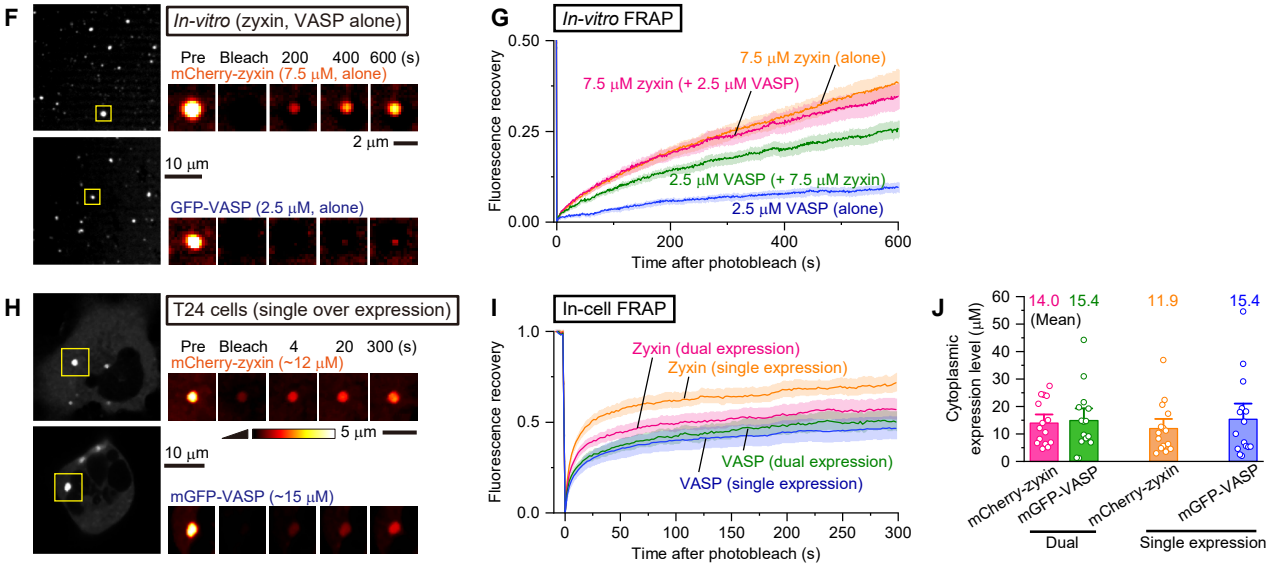

[*In-cell*] liquid behaviours of iTRVZ (talin rescued KO MEFs, apical PM)

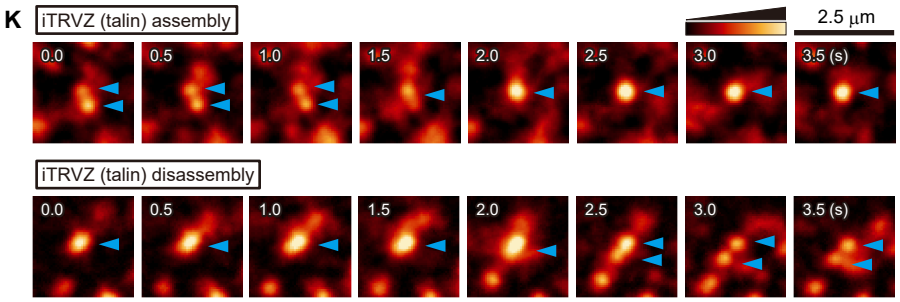

Figure S7

Rescue tries for Zyxin-KO MEF lines using zyxin and its mutants

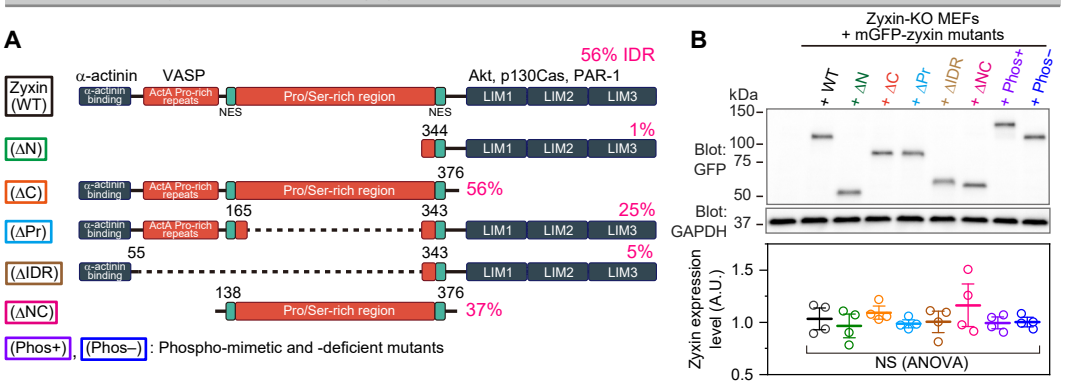

The lifetimes of iTRVZ (detected as talin clusters) containing zyxin mutants (KO MEFs expressing zyxin mutants, apical PM)

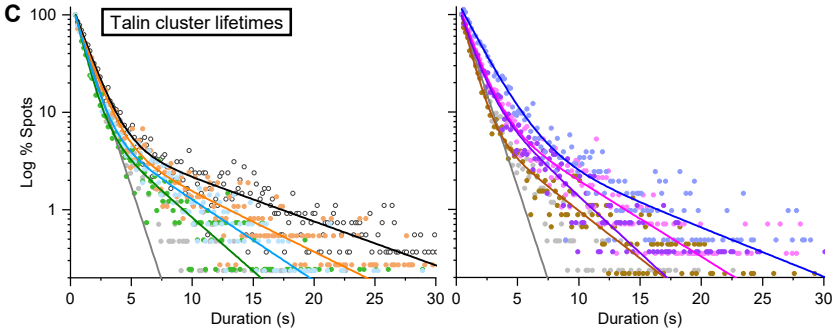

	Lifetime τ_1, τ_2 ± SEM (s) (%time)		
in Zyxin-KO MEF	1.1 ± 0.01 (100),	no τ_2 fraction	**
+ Zyxin (WT)	1.2 ± 0.02 (26),	9.6 ± 0.9 (74)	**
+ Zyxin (ΔN)	0.8 ± 0.02 (38),	4.0 ± 0.4 (62)	**
+ Zyxin (ΔC)	1.2 ± 0.03 (35),	7.0 ± 1.2 (65)	**
+ Zyxin (ΔPr)	0.9 ± 0.02 (34),	5.2 ± 0.5 (66)	**
+ Zyxin (ΔIDR)	0.8 ± 0.02 (36),	4.4 ± 0.5 (64)	**
+ Zyxin (ΔNC)	1.1 ± 0.04 (33),	5.6 ± 0.8 (67)	*
+ Zyxin (Phos+)	1.0 ± 0.05 (32),	3.7 ± 0.5 (68)	**
+ Zyxin (Phos–)	1.8 ± 0.06 (46),	8.6 ± 2.4 (54)	*
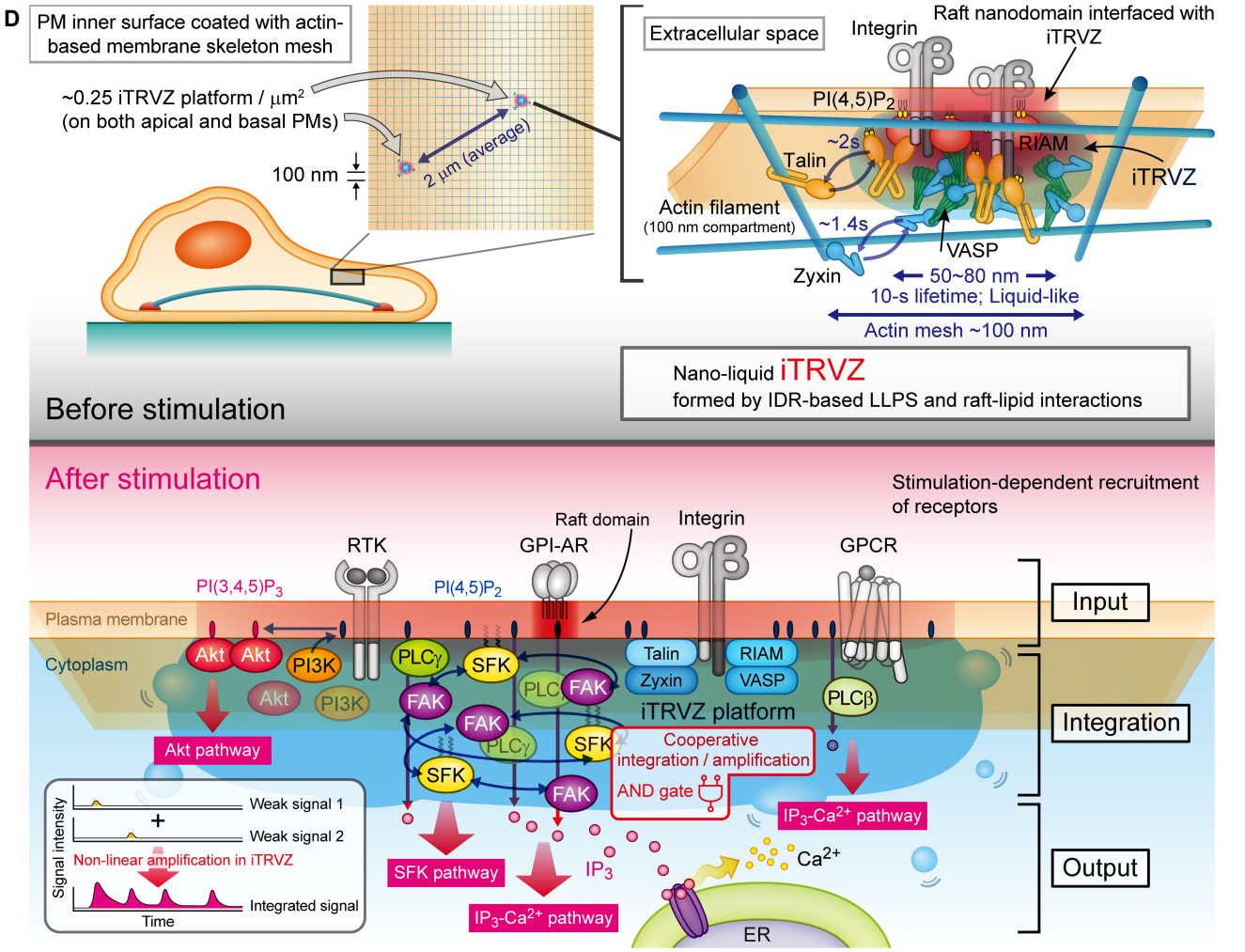
The summary of this study